Electrically Tunable Functional Nanomaterials for Actuation and Photonics

Vom Promotionsausschuss der
Technischen Universität Hamburg-Harburg
zur Erlangung des akademischen Grades
Doktor-Ingenieurin (Dr.-Ing.)
genehmigte Dissertation

von

Li-Hua Shao

aus

Hei Longjiang, China

2012

Gutachter:
Prof. Dr.-Ing. Jörg Weissmüller, Technische Universität Hamburg-Harburg
Prof. Dr. Manfred Eich, Technische Universität Hamburg-Harburg

Vorsitzender des Prüfungsausschusses:
Prof. Dr. Ernst Brinkmeyer, Technische Universität Hamburg-Harburg

Tag der mündlichen Prüfung: 23.02.2012

urn:nbn:de:gbv:830-tubdok-11433

Acknowledgements

It is a great pleasure for me to thank all the people who have supported me and contributed to the success of this thesis over the past couple of years.

First of all, I would like to express my deep and sincere gratitude to my supervisor, Prof. Jörg Weissmüller. I have been extremely lucky to have a supervisor like him, who gave me the opportunity to work on this exciting topic and kept his door open whenever I come to him for help and suggestions. His enthusiasm, inspiration, and ability to explain things clearly and simply make this work interesting and fruitful for me. I heartily thank to him for his encouragement, good teaching, sound advices, good company, and many wonderful ideas.

I gratefully acknowledge to the collaboration with the Institut für Angewandte Physik at Karlsruhe Institute of Technology. Thanks to the support of their group leader Prof. Martin Wegener, who provided the optical experiment setup and also thanks to Prof. Stefan Linden, who supplied the first batch of samples and helped for the initial tests. Thanks to Matthias Ruther for the help in metamaterial samples preparation and AFM characterization.

I also would like to express my deep gratitude to Dr. Jürgen Biener and Dr. Theodore F. Baumann from Lawrence Livermore National Laboratory at California in USA. Thanks to them for providing carbon aerogels samples and characterizing the mass-specific surface area and analysis structure size by SEM.

I wish to thank my group colleagues Dr. Jürgen Markmann and Dr. Robert Günther, who had the critical proofreading of this thesis and gave lots of useful suggestions. I sincerely appreciate Dr. Maxim Smetanin for fruitful discussions during my writing. My appreciation also goes to Dr. Hai-Jun Jin, Dr. Dominik Kramer and Dr. Raghavan N. Viswanath for their scientific suggestions and encouragements during my research at Institute of Nanotechnology.

Special thanks to Christine Fischer, Erika Schütze, Dr. Olaf Wollersheim, Dr. Christian Röthig, Renate Bender and Ursula Mösle for taking care of official matters during my stay at Institute of Nanotechnology at Karlsruhe Institute of Technology.

And many thanks to everyone who helped in any way contributing to this thesis.

Financial support from the Deutsche Forschungsgemeinschaft (Centre for Functional Nanostructures Karlsruhe) is gratefully acknowledged.

Finally, I want to thank my family for the patience, support and understanding.

Abstract

Nanomaterials with tunable electronic structure exploit the large specific surface area of metal nanostructures along with the strategy of tuning the surface properties through the controlled introduction of space-charge regions. Then, materials with tunable macroscopic properties can be created. The present thesis work achieved a successful synthesis of metallic and carbon-based tunable nanomaterials and demonstrated novel functional behavior in two fields of application: actuation and photonics. The work also proposes concepts for the underlying fundamental processes. In more detail, the following aspects were explored:

The growing interest in strain induced by capillary forces in porous materials motivates our search for the underlying mechanism. For the first time, an experiment was designed to illustrate the important distinctions in different capillary forces and their impact on the strain in porous materials. The strategy is to compare (1) dilatometry to probe macroscopic sample dimension change and (2) wide-angle x-ray diffraction to probe the lattice parameter variation of a gold crystal lattice. The resulting two strain measures on nanoporous gold show a significant difference. This observation confirms the fundamental distinction between the strain in response to the action of the surface stress at the solid surface and the strain in response to changes in the pressure in the fluid. This can be a correction of the previously reported works, which did not take into account the surface stress effect.

Using nanoporous noble metals, one can get large strain and mechanical energy density in a stiff actuator material via an applied voltage in an electrolyte. A similar concept may be applied to carbon aerogel, which is a light-weight, low cost porous material with extremely large surface area. This work demonstrates the potential of this material for actuation, with an unusually large reversible volume strain, 6.6%. The mass-specific strain energy density even exceeds that of piezoceramics and of nanoporous metal actuators. On top of that, a fundamental electrochemical parameter potential of zero charge (*pzc*) of carbon aerogel is measured. The results demonstrate that the *pzc* does not necessarily coincide with the potential of the maximum surface stress. This confirms the above-mentioned distinction between the capillary forces.

Another instance for the concept of tunable nanomaterials is electrical modulation of photonic metamaterials. Arrays of lithographical resonators are used to fabricate Metamaterials, from which one can achieve an unconventional optical response – in the extreme, the negative refractive index. The novel concept presented here is that the space-charge at the surface of each resonator is modulated by the applied potential in electrochemical environment. In this way, this work achieves a large and reversibly tunable resonance. One can switch on/off the resonance ideally by an electric signal, which is attractive for applications as functional photonic metamaterial devices. While the underlying mechanism is not conclusively understood, it is natural to suspect a coupling between the space charge and the electric resistance. Experiments using Pb and Cu underpotential deposition were performed, and the trends in the results support the notion of a decisive impact of the resistance on resonance damping, while the electron density change appears to mainly influence the resonance frequency.

Contents

1 Introduction

1.1 Background and motivation

Nanomaterials have been gaining enormous interests from the fundamental point of view and also for applications within recent years. Papers on the synthesis, characterization, modeling and exploring the potential application of nanomaterials grow considerably. Nanomaterials can be metals, ceramics, polymeric materials, or composite materials, their range of properties and possible applications appear to be huge [1]. The extremely small feature size in the range of 1-100 nanometers (nm) makes nanomaterial have a significantly high surface to volume ratio. In bulk materials, only a relatively small percentage of atoms will be at or near a surface or interface. While in nanomaterials, half or even more atoms will be near the interfaces. Hence, the materials performance here is no longer controlled by the familiar traditional properties of the bulk phases. Instead, the materials behavior relies on size- and interface effects a lot. Surface properties such as energy levels, electronic structure, interatomic forces and reactivity can be quite different from interior states, and give rise to quite different macroscopic material properties, such as mechanical, electronic, optical, magnetic, chemical, and biological properties. Their unusual properties bring opportunities for novel materials design and applications [2]. The search for new materials and devices in nanoscale and the related understanding of the underlying fundamental processes behind the functionality continues to be a major task for scientists. This is also the motivation for the present study. The details will be discussed in the following sections.

1.1.1 Electrochemically controlled space-charge region

Nanomaterials can be designed and tailored at the molecular level to have desired functionalities and properties. Manipulating matter at such a small scale with precise control of its properties is one of the hallmarks of nanotechnology [1]. The rapid development of nanotechnology will change the way we live by creating various novel materials and existing materials will be stronger, lighter, and more durable when coupled with nanotechnology [3]. One of the most powerful and important technology is electrochemical nanotechnology, which allows to precisely control and monitor the processes undergoing on the material surface in an electrolyte. For example, the scientists show their particular interests on the electrically tunable macroscopic properties of nanomaterials through the controlled introduction of the space-charge region at surfaces or interfaces through the action of an applied voltage. As schematically shown in Figure 1.1, an interconnected nanocrystalline network under an applied voltage in an electrolyte, an electrochemical

double layer is formed by the induced charge at the interface between the metal and the electrolyte. Under the applied voltage, the high density of conduction electrons in metals favors the highly efficient electronic screening, the space-charge layers at interfaces are restricted to a region of about one lattice constant, which is much narrower than the space-charge regions in semiconductors, which are between about ten and one thousand lattice constants [4]. On the other hand, the induced charge, which is typically up to a few tenths of an electron per interfacial atom, remains localized near these atoms. Therefore, the effect on local properties such as the interatomic bonding or the atomic magnetic moments may be quite large [5]. On top of that, for nanoscale microstructures with a large surface-to-volume ratio, the space-charge regions at interfaces can occupy a substantial volume fraction of the solid, which may lead to a modification of overall properties [6]. Based on these ideas, the scientists have measured the charge-induced reversible variation of resistance, conductivity as well as magnetic susceptibility of nanocrystalline metals [7-11].

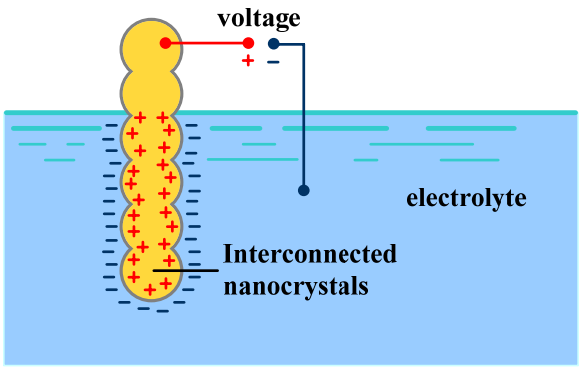

Figure 1.1 Schematic illustration of an interconnected array of nanoparticles immersed in an electrolyte under an applied voltage.

1.1.2 Nanoporous materials as electrochemical actuators

A specific example of the important previous works is the successfully measured reversible strain of nanoporous platinum under the control of surface charge density by varying the potential within the electrolyte, which has been suggested for 'metallic muscles' application [5]. Porous material consists of a solid skeleton (of metal, semiconductor, polymer) interspersed with open pores. Nanoporous materials are a subset of porous materials, typically having large porosities (greater than 40%), and pore diameters between 1- 100 nm. This structure makes the material high surface-to-volume ratio, low specific weight and very uniform pore distribution, which qualify them for many applications. The recent past has seen a growing interest in the strain of such materials in response to the capillary action [12-14]. Capillary action, also known as capillarity, is the tendency of a liquid to rise in narrow tubes or to be drawn into small openings such as those between grains of a rock [15]. Capillary action is a result of the intermolecular attraction within the liquid and solid materials, which could lead to the changes of capillary forces, such as the change of surface tension, surface stress, Laplace pressure and so on.

Capillary forces can have an important effect on the performance of nanoscale functional materials and devices. The very high strains induced by capillarity have been obtained both of the

nanoporous gold cantilevers and nanoporous Au-Pt alloys, which can be used as electrochemical actuators with a strain energy density higher than piezoceramics [16,17]. However, some scientists also point out the lack of an appropriate theory [14,18]. In order to find out the reason for reversible dimension change of porous material, a theoretical explanation has been worked out [19], which connects the macroscopic strain of a nanoporous body to the change of the capillary forces at its surface – surface stress. Their result [19] shows that the macroscopic dimension change of the bicontinuous structure, which models nanoporous gold, is more than 5 times higher than the mean strain of the bulk. This result appears unexpected at first sight, and what's more, it conflicts with the theory used by the authors who model sorption strain and capillary condensation [13,20-22]. Capillary condensation is the process by which multilayer adsorption from the vapor (phase) into a porous medium proceeds to the point at which pore spaces are filled with condensed liquid from the vapor (phase) [23,24]. The unique aspect of capillary condensation is that vapor condensation occurs below the saturation vapor pressure [25]. This phenomenon has a more physics-oriented context, since the transition from the adsorbate state with the adsorbate layer covering the inner walls of the pores and vapor in the central part of the pores to the capillary condensed state is accompanied with the deformation of the pore walls. In Refs. [13,20-22], the strains of porous silica induced by capillary condensation or by the adsorption and desorption of a liquid were discussed through the action of Laplace pressure alone without taking in account the surface stress action. Thus, the different theories used in previous reported works further complicates the problem. In all instances addressed above there is a central requirement that the capillary phenomena can be linked to experimentally accessible strain parameters. While theory indicates that quite different strain measures can be defined [19], experiments so far have not systematically explored the issue. Therefore, it is urgently required for an experimental work designed to testify which theory is correct and also to systematically explore the mechanisms for capillarity-driven deformation of a porous material.

Even though nanoporous noble metal materials are promising for use as electrochemical actuator, the high costs of such materials are an impediment to their application, as is the fact that typical carbon nanotube arrays cannot be loaded in compression [26]. It is therefore of interest to search for alternative materials which combine mechanical and chemical stability with low cost. Based on the development of nanoscience and nanotechnology, a lot of novel materials are emerging recently. One of these advanced materials is carbon aerogels (CAs), which have attracted interests as electrode material for various electrochemical applications, including supercapacitors, capacitive deionization, and fuel cells [27- 32]. CAs are nanoporous materials with very high specific surface areas (up to 3200 m^2/g) and low density. CAs also show a very high electric conductivity and chemical stability, and what is more that they are bulk nanostructured material, which means they can be loaded compressively. All the advantages given above of CAs make this material promising for actuation application. So far, their possible use as actuator has not been explored.

Besides their use in actuation, nanoporous solids impregnated by an electrolyte are also of interest with regard to the measurement of a fundamental parameter of electrode surfaces, namely the potential of zero charge (*pzc*). All of the aforementioned applications of CAs, rely on the formation of the electrochemical double layer at the electrode/electrolyte interface. One of the fundamental parameters required to describe this phenomenon is the *pzc*, which is defined as the potential at which there is no excess charge on the electrode surface, and the most common approach to measure this quantity is to determine the minimum of the differential capacity predicted by the Gouy-Chapman theory. However, the presence of surface inhomogeneities can obscure the observation of this capacity minimum [33]. Thus it has been proposed to use the maximum of

surface tension – which is embodied in the Lippmann equation [34] – as an alternative indicator of the *pzc* by measuring the dimensional changes of the electrode as a function of the applied potential [35,36]. In the case of liquid electrodes (for instance, mercury), the *pzc* indeed coincides with the maximum of the surface tension – from which it can be measured. However, for solid metals, it has been demonstrated that the *pzc* and the potential of maximum surface stress do not have to be identical ([37], see also Ref. [38] and references therein). This controversy also requires reinvestigating the properties of CAs and giving a correct method to measure the *pzc*.

1.1.3 Electrical modulation of photonic metamaterial device

Another instance for the concept of tunable nanomaterials is electrically tunable gold structured photonic metamaterials. Part of this work is motivated by the recent development on photonic metamaterials, which provides a strategy for obtaining unconventional optical response – in the extreme, negative refractive indices – by lithographically structured elements such as arrays of split-ring resonators (SRR) [39]. Metamaterials are artificial periodic structures with the feature size smaller than the wavelength of light. Most photonic metamaterials rely on plasmonic resonances of metallic nanostructures that can give rise to an effective magnetic response at elevated or even at optical frequencies [40, 41]. In fact, all the novel phenomena achieved by metamaterials, such as negative refraction [42], perfect lensing [43] and electromagnetic cloaking [44], are limited to a fixed narrow spectral bandwidth. For applications, the frequency tunable metamaterials whose operating frequency can be adjusted, is of great interest. The scientists have shown that tuning the electric or magnetic resonance positions by varying the dimension or orientation of SRRs or changing the incident direction [45,46]. However, for many applications, it is obviously highly desirable to tune these metamaterial resonances or to even modulate them, ideally by an electric signal. Several approaches have recently been discussed, such as utilizing an external field to change the orientation of the molecules in an aligned nematic liquid crystal to tune the refractive index of the metamaterial [47-49], changing the conductivity by using the metal-insulator phase transition in vanadium oxide (VO_2) to tune the optical transmission [50,51], or changing the dielectric properties of an adjacent chalcogenide glass layer by an electrically stimulated transition between amorphous and crystalline forms of the glass to produce a change in resonance frequency [52]. The changes of metal's optical properties by changing its charge density have been investigated on bulk Au, Ag, and Cu single crystal surfaces [53], on surface plasmon polaritons of thin Au films [54], as well as on nanometer-sized gold particles resonances [55-57]. For bulk Au crystals, the resulting optical modulation of the reflectance has been less than 1% [53]. The observed effect is also quite small for the surface plasmon polaritons, whereas for chemically synthesized Au nanocrystals, the modulation of the optical properties can even be seen by a color change with the naked eye in darkfield microscopic images [58]. However, for lithographically fabricated metallic photonic metamaterials, no one has investigated the possibility to modulate their optical properties by controlling the surface charge density under an applied voltage. The relevant feature sizes of photonic metamaterials tend to be intermediate of bulk crystals and nanocrystals. Thus, it has not been clear at all whether the sizable electrochemical optical modulation can be translated to metamaterials. If it is possible, no doubt that will bring the photonic metamaterial to real application.

1.2 Scope and structure of this work

The present investigation focuses on studying the properties of nanoscale materials, with an emphasis on electrical tailoring and modulation to achieve desired properties and functions. All of the aforementioned problems will be addressed in the following chapters.

As electrochemical technology is used as basic tools through all this work, the fundamental principles of electrochemistry will be introduced in the first part of Chapter 2. On top of that, the basic theory about the capillarity induced dimensional change of porous materials and the fundamentals of photonic metamaterials will also be presented in Chapter 2.

The detailed experiment procedures will be described in Chapter 3, including the electrochemical cell arrangement, samples fabrication and corresponding in-situ experiment setups.

The fundamental research and potential applications of nanoporous material will be discussed in Chapter 4, which is formed of two parts. In the first part, in order to figure out the mechanisms for capillarity-driven deformation of nanoporous metal, an experiment is designed to illustrate the important distinction between different strains through: (1) dilatometry to probe the resulting change in macroscopic sample dimension and (2) in-situ wide-angle x-ray diffraction to probe the variation in the lattice parameter of the gold crystal lattice. The two strain measures assume significantly different values. The results do confirm the fundamental difference between the strain in response to the action of the surface stress at the solid surface and the strain in response to changes in the pressure in the fluid, which also support the validity of the theoretical argument in Ref. [19]. In the second part, the fundamental electrochemical and electromechanical properties of nanoporous carbon aerogels are investigated through impedance measurement and in-situ dilatometry. The results demonstrate that the potential of zero charge does not necessarily coincide with the potential of the maximum of surface stress. Furthermore, a tunable electrochemical carbon aerogel actuator is achieved with a giant volume strain of 6.6% and higher mass specific work density compared to the reported values for other actuators.

In Chapter 5, the concepts of electrochemically tunable metamaterials are exploited showing that the electrochemical modulation is surprisingly large and hence attractive for applications as functional photonic metamaterial devices. And also, lead and copper underpotential deposition is taken out to qualitatively explain the mechanism of the electrical modulation phenomena.

This dissertation finishes at Chapter 6, which summarizes the whole work and gives an outlook on the future research.

2 Theoretical background

2.1 Fundamentals of electrochemistry

The aim of this work is the application of electrochemical methods to the study of material properties. Therefore, the fundamental principles of electrochemistry will be introduced in this section, which mainly follows Bard and Faulkner's textbook [59].

Electrochemistry is a branch of chemistry concerned with the interrelation of electrical and chemical effects. The scientists using electrochemistry study the loss of electrons (oxidation) or gain of electrons (reduction) that a material undergoes when an electric potential is applied and current passes. These reduction and oxidation reactions are commonly known as redox reactions and can provide information about the concentration, kinetics, reaction mechanisms, chemical status and other behavior of species in solution. Similar information can be obtained concerning the electrode surface. In fact, electrochemistry can cover a huge range of different phenomena, like corrosion, devices such as electro analytical sensors, batteries and fuel cells, and technologies as electroplating and the large-scale production of aluminum and chlorine.

2.1.1 The structure of the electrified interface

In electrochemical systems, the scientists are concerned with the processes and factors that affect the transport of charge across the interface between chemical phases, for example, between an electronic conductor (an *electrode)* and an ionic conductor (an *electrolyte*). The collections of interfaces are called *electrochemical cells.* These systems are defined generally as two electrodes separated by at least one electrolyte phase. The distribution of charge at an electrified interface is a central factor in electrochemical activity and has been extensively studied [60].

2.1.2 Faradaic and nonfaradaic processes

There are two kinds of processes that occur at electrodes. One kind comprises reactions where charges (e.g., electrons) are transferred across the metal-solution interface. Electron transfer causes oxidation or reduction. Since such reactions are governed by Faraday's law (i.e., the amount of chemical reaction caused by the flow of current is proportional to the amount of electricity passed), they are called *faradaic* processes. Under some conditions, a given electrode-solution interface will show a range of potentials where no charge-transfer reactions occur because such reactions are thermodynamically or kinetically unfavorable. However, processes such

as adsorption and desorption can occur, and the structure of the electrode-solution interface can change with changing potential or solution composition. These processes are called *nonfaradaic* processes. Although charge does not cross the interface, external currents can flow when the potential, electrode area, or solution composition changes. Both faradaic and nonfaradaic processes occur when electrode reactions take place.

2.1.3 The ideal polarized electrode and electrical double layer

An electrode at which no charge transfer can occur across the metal-solution interface, regardless of the potential imposed by an outside source of voltage, is called an *ideal polarized* (or *ideal polarizable) electrode* (IPE). While no real electrode can behave as an IPE over the whole potential range available in a solution, some electrode-solution systems can approach ideal polarizability over limited potential ranges. The only faradaic current that flows in this region is due to charge-transfer reactions of trace impurities (e.g., metal ions, oxygen, and organic species), and this current is quite small in clean systems.

Since charge cannot cross the IPE interface when the potential is changed, the behavior of the electrode-solution interface is analogous to that of a capacitor. At a given potential, there will exist a charge on the metal electrode, Q^M, and a charge in the solution, Q^S. Whether the charge on the metal is negative or positive with respect to the solution depends on the potential across the interface and the composition of the solution. At all times, however, $Q^M = -Q^S$. (In an actual experimental arrangement, two metal electrodes, and thus two interfaces, would have to be considered; we concentrate our attention here on one of these and ignore what happens at the other.)

The charge on the metal, Q^M, represents an excess or deficiency of electrons and resides in a very thin layer (< 0.1 Å) on the metal surface. The charge in solution, Q^S, is made up of an excess of either cations or anions in the vicinity of the electrode surface. The charges Q^M and Q^S are often divided by the electrode area and expressed as *charge densities*, such as, $q^M = Q^M/A$, usually given in $\mu C/cm^2$. The whole array of charged species and oriented dipoles existing at the metal-solution interface is called the *electrical double layer*.

The solution side of the double layer is thought to be made up of several "layers" as shown in Figure 2.1. That closest to the electrode, the *inner layer,* contains solvent molecules and sometimes other species (ions or molecules) that are said to be *specifically adsorbed*. This inner layer is also called the *compact, Helmholtz,* or *Stern layer*. The locus of the electrical centers of the specifically adsorbed ions is called the *inner Helmholtz plane* (IHP), which is at a distance x_1. The total charge density from specifically adsorbed ions in this inner layer is q^i ($\mu C/cm^2$). Solvated ions can approach the metal only to a distance x_2; the locus of centers of these nearest solvated ions is called the *outer Helmholtz plane* (OHP). The interaction of the solvated ions with the charged metal involves only long-range electrostatic forces, so that their interaction is essentially independent of the chemical properties of the ions. These ions are said to be *nonspecifically adsorbed.* Because of thermal agitation in the solution, the nonspecifically adsorbed ions are distributed in a three-dimensional region called the *diffuse layer,* which extends from the OHP into the bulk of the solution. The excess charge density in the diffuse layer is q^d, hence the total excess charge density on the solution side of the double layer, q^S, is given by $q^S = q^i + q^d = -q^M$.

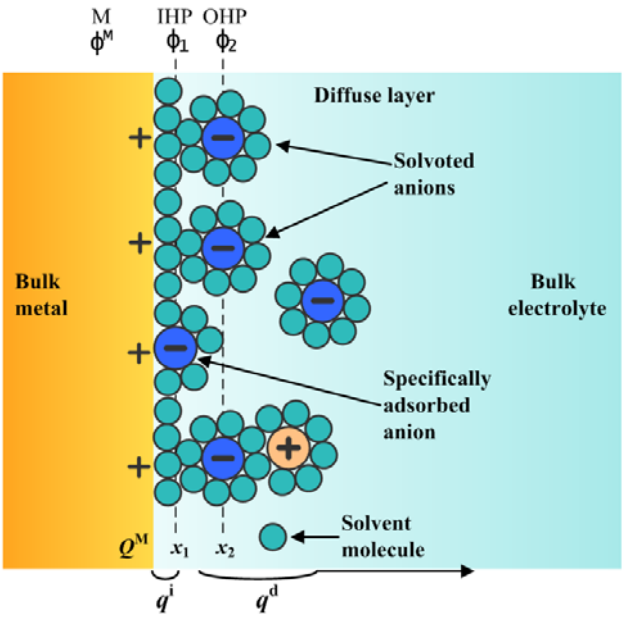

Figure 2.1 Schematic model of the double-layer region under conditions where anions are specifically adsorbed. A metal electrode M with potential ϕ^M is immersed in an electrolyte. The charge on the metal, Q^M, represents an excess or deficiency of electrons and resides in a very thin layer (< 0.1 Å) on the metal surface. The solution side of the double layer is thought to be made up of several "layers". The locus of the electrical centers of the specifically adsorbed ions is called the *inner Helmholtz plane* (IHP), which is at a distance x_1 and with a potential ϕ_1. The total charge density from specifically adsorbed ions in this inner layer is q^i (μC/cm^2). Solvated ions can approach the metal only to a distance x_2; the locus of centers of these nearest solvated ions is called the *outer Helmholtz plane* (OHP) with a potential ϕ_2.

2.1.4 Electrochemical measurement aspects

2.1.4.1 Electrodes

In most electrochemical techniques and also in this work, a three electrodes arrangement is used – which composes of the working electrode (WE), the reference electrode (RE) and the counter (or auxiliary) electrode (CE).

The WE is where the reaction of interest occurs in an electrochemical system and usually is constructed of an inert conductive material. Any changes in the cell are ascribable to the WE, the potential of WE is measured versus the RE. The RE is designed with a constant makeup, and its potential is known and fixed. One can observe or control the *potential* of the WE *with respect to* the RE, and that is equivalent to observing or controlling the energy of the electrons within the WE.

The internationally accepted primary reference is the *standard hydrogen electrode* (SHE), or *normal hydrogen electrode* (NHE), which has all components at unit activity,

$$Pt/H_2(a= l)/H^+ \ (a = 1, \text{aqueous})$$

One of the common used references is the *saturated calomel electrode* (SCE), which is,

$$Hg/Hg_2Cl_2/KCl \ \text{(saturated in water)}$$

Its potential is 0.242 V *vs.* SHE. Another is the *silver-silver chloride electrode,*

$$Ag/AgCl/KCl \ \text{(saturated in water)}$$

with a potential of 0.197 V *vs.* SHE. It is common that potentials are identified as "vs. Ag/AgCl" in the literature when this electrode is used.

The ohmic drop is $I \times R$ between WE and RE, where I denotes the current and R the electrolyte resistance. Hence, in order to minimize the potential drop and to get a precise potential value of the WE, the RE should be kept to the WE as close as possible.

The current flows between WE and CE. One can imagine the current passing along paths of roughly equal length, terminated by the faces of the two electrodes. All of the current should pass through a solution volume of extremely small cross-sectional area near the WE. Therefore, the CE is usually chosen much larger than the WE, in which case this solution volume is broadly based on the end connecting to the CE, but narrowly based at the WE.

The three electrodes are connected to a potentiostat, an instrument that controls the potential of the WE and measures the resulting current. In an electrochemical experiment, one can measure one or more of four parameters—potential (E), current (I), charge (Q), and time (t). The response of a system depends on which parameter is used as the excitation signal. By plotting different parameters in different ways, one can derive a wealth of information.

2.1.4.2 Open circuit potential

The open circuit potential, E_{OCP} (also called the zero-current potential, equilibrium potential or the rest potential), is the potential of the WE relative to the RE when no potential or current is being applied to the cell. E_{OCP} depends on many aspects, such as trace impurities in the solution (e.g., oxygen) and the previous history of the working electrode. I will not introduce the fundamentals of E_{OCP} here, only show the method used in this work to measure the E_{OCP}. E_{OCP} can be easily measured by a potentiostat or even with a voltmeter. The method used in this work is connecting the WE and RE to the potentiostat without immersing the CE in the electrolyte after the electrochemical cell is built, then the value of E_{OCP} can be measured versus time.

2.1.4.3 Cyclic voltammetry

Cyclic voltammetry is the most commonly used technique for characterizing and acquiring the information of an electrochemical system, since it is the most sensitive direct electrochemical technique for examination of both the thermodynamic and kinetic aspects of electrochemical surface processes [61]. In a cyclic voltammetry experiment, the potential of the WE is scanned by the potentiostat in a fixed potential range (or potential window) with the two limit values, E_1 and

E_2, at a constant rate, v, as shown in Figure 2.2. The scanning starts from any potential between E_1 and E_2 to positive direction, and when it reaches E_2 the scan is reversed to E_1 till returning to the initial potential. The current response to this modulation of electrode potential is recorded conjugate to varied potential, giving rise to a so-called voltammogram or cyclic-voltammogram (CV) (see Figure 2.2). The peaks "1" and "2" correspond to some anions adsorption, (for instance, OH^-, SO_4^{2-}, Cl^- and so on) and "3" and "4" are the corresponding desorption peaks, which is a reversible process for a nonfaradaic reaction. The small current outside these features indicates dominantly capacitive double-layer (d.l.) processes. Hence, from the CV curve, one can identify the electrochemical signatures of the WE, and corresponding process taking place at the interface between the WE and electrolyte.

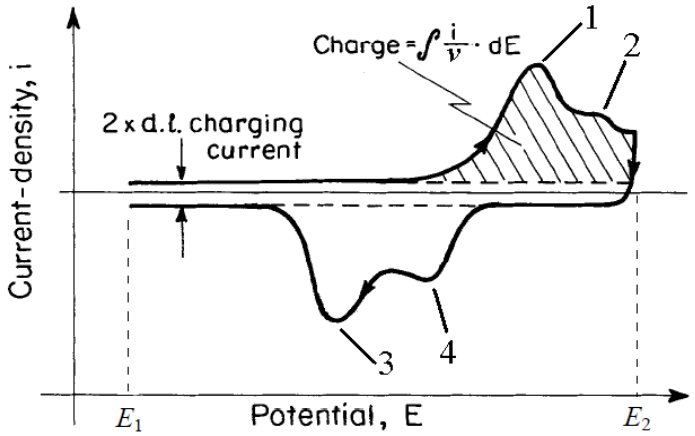

Figure 2.2 Typical cyclic voltammogram (CV) of an noble metal electrode in electrolyt for identifying the electrochemical surface process (response current density, i, plotted as a function of potential, E, cycled between two limits E_1 and E_2 at a rate v = dE/dt). The peaks "1" and "2" correspond to the anions adsorption, and "3" and "4" are the corresponding desorption peaks, which is a reversible process for a nonfaradaic reaction [61].

2.1.4.4 Chrono-amperometry

Another commonly used electroanalytical technique is chrono-amperometry, in which the potential of the WE is stepped and the resulting current from electrochemical processes occurring at the electrode (caused by the potential step) is monitored as a function of time [59]. A typical stepped potential excitation waveform and the resulting current response versus time are presented in Figure 2.3, where one can see that when the potential jumping to another value, the corresponding current changes gradually and becomes stable after certain time.

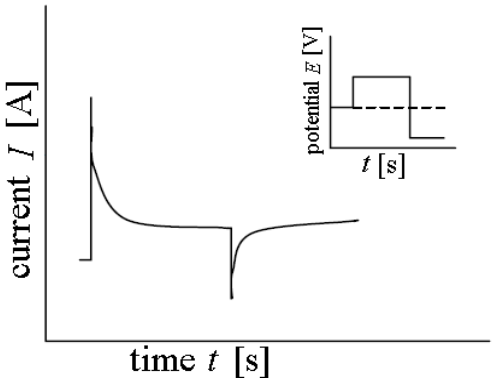

Figure 2.3 Typical chronoamperogram, where current I changing versus time t. Inset is excitation stepped potential.

2.1.5 Potential of zero charge (pzc) and Gouy-Chapman theory

The potential of zero charge (*pzc*) is a fundamental property of the electrode-electrolyte interface, which is defined as the potential at which there is no excess charge on the electrode surface. The *pzc* is a key parameter for a detailed understanding of double layer phenomena and properties [62]. And furthermore, the *pzc* of a given electrode in contact with a solution is related to its work function in vacuum [63].

Considerable progress has been made in the development of the methods for measuring the *pzc* of electrodes. One of the most common and reliable method is based on the Gouy-Chapman theory, which indicates that the differential capacitance, C, of the double layer between an electrode and an electrolyte is [59]

$$C = \frac{\mathrm{d}q}{\mathrm{d}E_0} = \left(\frac{2z^2e^2\varepsilon\varepsilon_0 n^0}{\kappa T}\right)^{1/2} \cosh\left(\frac{2eE_0}{2\kappa T}\right) \qquad 2.1$$

where q is the excess charge on the electrode surface and E_0 is the potential drop across the diffuse layer as shown in Figure 2.1. The other quantities are the dielectric constant of the medium, ε, the vacuum permittivity, ε_0, the charge on the electron, e, the Boltzmann constant, κ, the absolute temperature, T, the charge number of the ion in the bulk electrolyte, n^0, and the magnitude of the charge on the ions, z, for a system containing only a symmetrical electrolyte (an electrolyte having only one cationic species and one anionic species, both with charge magnitude z. Sometimes symmetrical electrolytes, for example, NaCl, HC1, and $CaSO_4$, are called "z:z electroytes").

Figure 2.4 shows the way of differential capacitance, C, varing with potential according to equation 2.1. There is a minimum for each curve, where the excess charge on the electrode surface is zero – which gives the $E = E_{\mathrm{pzc}}$.

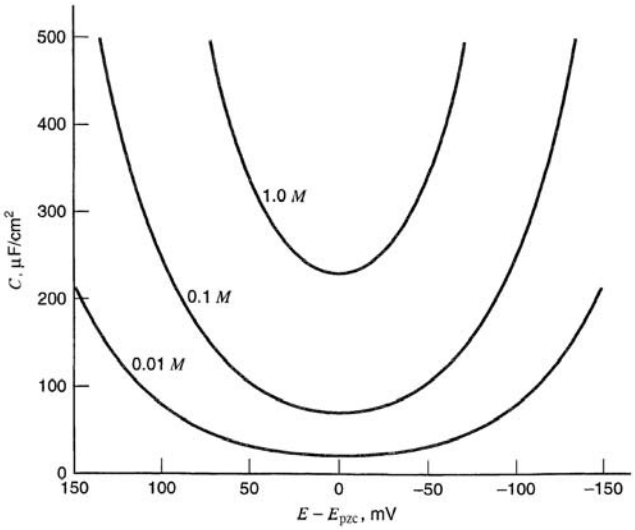

Figure 2.4 Predicted differential capacitances from Gouy-Chapman theory. Calculated for the indicated concentrations of a 1:1 electrolyte in water at 25°C [59].

2.1.6 Impedance spectroscopy

The differential capacitance (or double layer capacitance) and its dependence on potential (the "capacitance curve $C(E)$") can be obtained by impedance spectroscopy, from which one can identify the *pzc* where the capacitance gets its minimum. In the following, a simple model of electrochemical system will be presented, which is also used in this work.

Impedance spectroscopy implies the dependence of impedance on the frequency of an alternative current (ac) applied to a cell [64]. The total impedance, Z, of the electrochemical cell consists of the ohmic resistance of the electrolyte R, and the double layer capacitance C in series as shown in Figure 2.5.

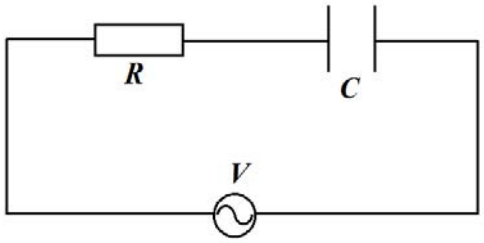

Figure 2.5 A resistor with resistance of R and a capacitor with capacitance of C in series circuit under the applied ac voltage V.

Now let us calculate the impedance of this capacitor. An ac voltage can be represented by

$$V = V_0 e^{i\omega t} \qquad 2.2$$

where i is the imaginary unit, ω is the angular frequency of the ac perturbation. With $I = \mathrm{d}Q/\mathrm{d}t$, $C = Q/V$, we have

$$I = i\omega C\, V_0\, e^{i\omega t} \tag{2.3}$$

Thus, the impedance of a capacitor Z_C is

$$Z_C = \frac{V}{I} = \frac{V_0 e^{i\omega t}}{i\omega C V_0 e^{i\omega t}} = \frac{1}{i\omega C} \tag{2.4}$$

The impedance of resistor and capacitors are additive [64]. Hence, the total impedance Z of the interfacial region between the working electrode and the reference electrode, at any direct current (dc) potential E, is given by

$$Z = Z_{\mathrm{Re}} + iZ_{\mathrm{Im}} = R + (iC\omega)^{-1} \tag{2.5}$$

where Z_{Re} and Z_{Im} are the real and imaginary parts of the impedance, respectively. Thus, at any electrode potential, the capacitance can be obtained from the measured impedance as

$$C = -(\omega Z_{\mathrm{Im}})^{-1} \tag{2.6}$$

In this work, an appropriate frequency was found at first, and then a single-frequency impedance at different potentials was measured. Afterwards, the double layer capacitance can be calculated via Eq. 2.6.

2.2 Dimensional change of porous materials

2.2.1 Surface stress, surface tension and the relation to *pzc*

In the past years, many works have been done in distinguishing the concepts of surface tension and surface stress [38,65-67]. Surface tension, γ, is the work per area required to form new surface reversibly at constant structure, for instance by adding atoms to the surface or by cleavage [68]. By contrast, surface stress, **s**, measures the forces required to change the interatomic distance at constant number of atoms by opposing an elastic deformation of the surface [69,70].

For an interface between two **liquid** media, the surface stress is identical to the surface tension. One can easily derive a simple relation between the electrode potential, the surface charge density and the interface stress, which is known as the Lippmann equation [34,71]:

$$\frac{\mathrm{d}\gamma}{\mathrm{d}E} = -q \tag{2.7}$$

The Lippmann equation is obtained through electrochemical experiments with a mercury droplet in contact with an electrolyte. If the double layer capacitance c_0 is independent on the potential and the surface concentrations are kept constant, we will have $q = c_0 (E - E_0)$ with the potential of zero charge (*pzc*), E_0. Then the surface tension, γ, depends on the square of the charge density, q, in the double layer, and has a maximum at the *pzc*, E_0 [65]:

$$\gamma - \gamma_0 = -\tfrac{1}{2}\, c_0\, (E - E_0)^2 = -\tfrac{1}{2}\, q^2/c_0 \qquad 2.8$$

Therefore, from the electrocapillary curve, i.e. surface tension γ versus electrode potential E, the *pzc* can be measured as the potential where the maximum of the surface tension γ is. However, this method can only be used for a liquid metal electrode.

By contrast, the surface tension and surface stress is different for solids. Valincius has demonstrated that the *pzc* and the potential of the maximum surface stress are not identical [37]. This is particular relevant in the case of porous carbon, because the *pzc* has been measured by monitoring the electrode dimensional changes [35,36]. Therefore, it is especially valuable to reinvestigate the behaviour of carbon.

2.2.2 Mechanism for capillarity-induced strain of porous metals

Consider a finite sized porous solid body immersed in a fluid, so that the only tractions on the surface of the solid are those due to the action of the pressure in the fluid, and let the body be at rest in its mechanical equilibrium configuration. At equilibrium the stress, **S**, within the bulk (B) of the solid phase of a porous material is governed by the generalized capillary equation for solids [72],

$$\int_B (\mathbf{S} + P_F\, \mathbf{U})\, \mathrm{d}V + \int_S \mathbf{s}\, \mathrm{d}A = 0 \qquad 2.9$$

where the integration extends over the volume of B and the area of its surface, S. Here **U** denotes the unit tensor in three-dimensional space, **s** represents the surface stress tensor, and P_F is the uniform pressure in the fluid (F) in the pore space.

The stresses in equation 2.9 arise from two independent and fundamentally different capillary parameters: whenever the pores are partially filled, P_F is governed by the surface tension, γ_{FG}, and curvature, κ_{FG}, of the fluid-gas interface via the Young-Laplace equation,

$$P_F = 2\, \kappa_{FG}\, \gamma_{FG} \qquad 2.10$$

Additionally, the integral over the surface on the left-hand side of equation 2.9 links the stresses to the surface tension, γ_S, of the solid via the surface stress

$$\mathbf{s}(\mathbf{x}) = \partial \gamma_S(\mathbf{x},\mathbf{e}) / \partial \mathbf{e} \qquad 2.11$$

where **x** denotes a position on S and **e** represents the tangential projection of the bulk strain tensor in its limit on the surface at **x** [72]. The two capillary terms represent distinctly different physics: γ_{FG} is the scalar, positive-defined and typically uniform surface tension of the fluid-gas interface, whereas **s** is the surface stress tensor of the solid surface, that varies along S and has entries which may be of either sign. Whereas γ measures an excess energy per area of surface, **s** embodies the tendency of atoms at a solid surface to favor a different interatomic spacing than the underlying bulk. In studies of capillarity it is obviously of prime importance to account for this distinction. Remarkably, equation 2.9 implies a significant distinction between the elastic response to changes in the pressure in the fluid and changes in the surface stress.

Let us first consider the response of the solid to changes in P_F. Irrespective of the pore geometry, varying P_F induces a uniform and isotropic compensating stress in the bulk, $\delta\mathbf{S} = -\delta P_F\ \mathbf{U}$. For sufficiently symmetric elastic response the hydrostatic stress leads to an affine stretch in which the lattice parameter, a, of the solid phase and the macroscopic dimension, l, of the sample are changed by the same relative amounts [19],

$$\delta l/l = \delta a/a = -\tfrac{1}{3}\,\delta P_F/K \qquad 2.12$$

where K denotes the bulk modulus of the solid phase. In the present work, P_F is a constant, 1 atm, since the sample is completely immersed and there is no microscopic meniscus at the fluid-gas interface. Yet, even without that knowledge we can rule out changes in P_F as reason for the strain, since the observation of significantly different strain values (will be shown in Section 4.1) disagrees fundamentally with equation 2.12.

The situation is different when only the surface stress varies. By contrast, varying the surface stress leads to a nonuniform and, in general, nonhydrostatic stress response in the solid. The mean pressure in the bulk of the solid is again independent of the geometry and it obeys [19]

$$\langle \delta P \rangle_B = \tfrac{2}{3}\,\alpha\,\langle \delta f \rangle_S \qquad 2.13$$

with f = trace **s** a scalar surface stress and $\alpha = A/V$ the specific surface area (area per volume of B). For isotropic materials at small strain, their volume strain can be represented as [19]

$$\delta V/V = 3\,\delta l/l = 3\,\varepsilon \qquad 2.14$$

Combining the last two equations, an orientation-average of the mean lattice parameter changes as

$$\frac{\delta a}{a} = -\frac{2\alpha f}{9K} \qquad 2.15$$

Contrary to the lattice parameter change, the macroscopic strain depends strongly on the geometry. For instance, in a granular porous solid composed of arrays of interconnected spherical particles, the surface-induced stress in each individual sphere is uniform and isotropic. Hence, the lattice parameter change and the macroscopic strain are the same [19]

$$\frac{\delta a}{a} = \frac{\delta l}{l} = -\frac{2\alpha f}{9K} \qquad 2.16$$

In contrast, when consider a "felt"-like porous material consisting of an interconnected array of long thin fibers, the two strains are not the same any more. The fibers have a circular cross-section with uniform and identical diameter. Let the fibers be interconnected in nodes which transmit force and displacement. Assume a high aspect ratio, in the sense that the distance between nodes is much larger than the fiber diameter. Thus, the details of the stress distribution at the nodes can be ignored and treated as points of rigid contact between fibers. By inspection of the scanning electron micrograph of nanoporous gold (npg) (Figure 2.6) one can see that the network of fibers represents an idealized model for the material. The bulk stress which compensates the surface stress in each circular fiber is here anisotropic, with the radial stress component only half of the axial stress [72]. Assuming isotropic elasticity with Poisson ratio ν, the longitudinal and radial strains in the fiber are [19]

$$\frac{\delta l}{l} = \frac{\alpha f}{3K}\,\frac{\nu - 1}{1 - 2\nu} \qquad 2.17$$

$$\frac{\delta r}{r} = \frac{\alpha f}{3K}\,\frac{3\nu - 1}{2(1 - 2\nu)} \qquad 2.18$$

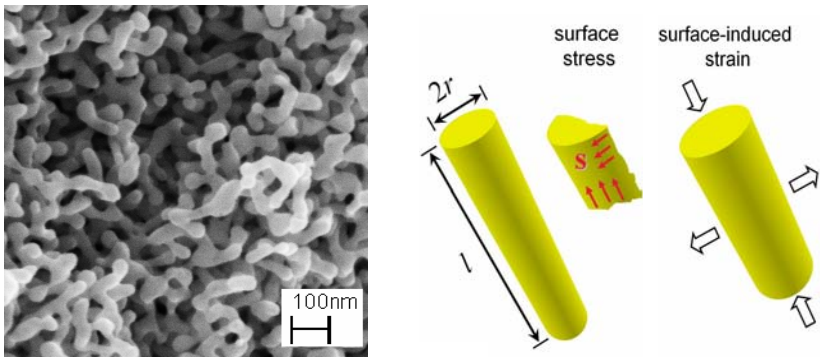

Figure 2.6 Left: SEM image of nanoporous gold showing a network of elongated ligaments. Right: Schematic illustrations of the surface stress and surface-induced strain in a circular nanofiber – resembling a ligament – of radius *r* and length *l*. Note longitudinal contraction and radial expansion (arrows outlined in black) under the action of a positive-valued surface stress (red arrows).

The two strains differ significantly in magnitude, and for ν >0.3 they are even opposite in sign (Figure 2.6). Since the macroscopic strain of the network will reflect the change in the fiber length, equation 2.17 relates the macroscopic strain of the fiber network to the surface stress.

Hence, the ratio between the macroscopic strain predicted by equation 2.17 and the lattice parameter change of equation 2.15 is

$$\Theta = \frac{\delta l / l}{\delta a / a} = \frac{3(1 - \nu)}{1 - 2\nu} \qquad 2.19$$

Take the gold material as an example, with the comparatively large Poisson ratio ν=0.44, the strain ratio Θ is as high as 7.0. And this value emerges as 5.5 from molecular dynamics simulations [19]. Other geometries will lead to different relations between the two strains [19], for instance the two values are identical for arrays of spherical particles [5].

We rewrite the mechanical equilibrium equation 2.13 between the surface and bulk when the surface stress varies as following

$$3V\langle\delta P\rangle_B = 2A\langle\delta f\rangle_S \tag{2.20}$$

Combining with the equation 2.14 and with the definition of the bulk modulus

$K = -\delta P\, V/\delta V$, we can obtain

$$\delta f = -\frac{9}{2}\frac{V}{A}K\frac{\delta l}{l} \tag{2.21}$$

Where the macroscopic length change δl can be measured with the dilatometer, the volume V can be determined from the density ρ and the mass m of the sample through the relation $V = m/\rho$. Hence, eq. 2.21 can be written as

$$\delta f = -\frac{9}{2}\frac{Km\delta l}{A\rho l} \tag{2.22}$$

Now, all the parameters are experimentally measurable. The macroscopic length change represented by equation 2.17 can be directly measured by in-situ dilatometry, while the lattice parameter variation shown in equation 2.15 can be obtained from in-situ X-ray diffraction measurement data. Using npg as a model system, whose ligaments have a high aspect ratio. If the ratio of the two measured strain Θ is considerably larger than 1, one can confirm that the surface stress is the main driving force during the dimension change of porous materials rather than the uniform pressure in the fluid.

2.3 Fundamentals of photonic metamaterial

In this section, some fundamental aspects about photonic metamaterial will be introduced, which mainly follows S.A. Ramakrishna's review paper [73] and S. A. Maier's text book [74].

2.3.1 Negative refractive index

In optics, the refractive index of a material is conventionally taken to be a measure of the 'optical density' and is defined as

$$n = c/v \tag{2.23}$$

where c is the speed of light in vacuum and v is the speed of an electromagnetic plane wave in the medium. From Maxwell's equations the refractive index is given as

$$n^2 = \varepsilon\mu \tag{2.24}$$

where ε is the relative dielectric permittivity and μ is the relative magnetic permeability of an isotropic medium. For common materials, ε and μ are positive values, and n could easily be taken as $\sqrt{\varepsilon\mu}$, but it is possible to obtain a negative n value under certain conditions.

The four quadrants in the Re(ε)–Re(μ) plane are shown in Figure 2.7, from which one can conveniently classify electromagnetic materials. The behavior of the waves is qualitatively different in each of the quadrants: materials in the first quadrant allow the normal right-handed electromagnetic propagating waves, the materials in the second and fourth quadrants do not allow any propagating waves inside them since all electromagnetic radiation is evanescently damped in these media, and in the third quadrant, when both of ε and μ are negative the materials having a negative refractive index, which allows left-handed propagating waves inside them [73]. Negative refraction never occurs in nature. However, people have recently designed artificial materials – metamaterials, to realize this effect [39].

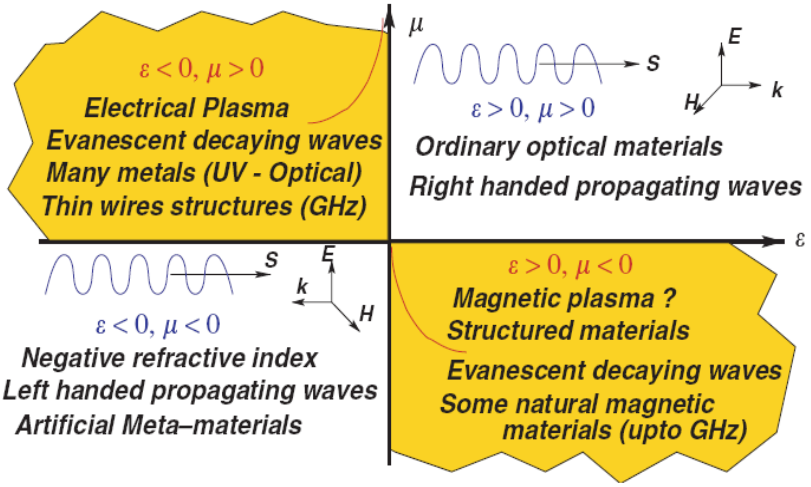

Figure 2.7 A schematic illustration of materials classification based on the dielectric and magnetic properties. The wavy lines represent materials that allow propagating waves, and the axes set in quadrants 1 and 3 show the right- and left-handed nature of E (electric field), H (magnetic field) and k(wave-vector) vectors. The waves in quadrants 2 and 4 decay evanescently inside the materials, which are depicted schematically. S is the Poynting vector. (from Ref. [73])

2.3.2 Concept of metamaterial

The dielectric permittivity, ε, and the magnetic permeability, μ, characterize the macroscopic response of a homogeneous medium to applied electric and magnetic fields. They are macroscopic parameters, because experimentally one usually detects temporal and spatial average responses rather than the actual microscopic fields of electrons and atoms on the atomic scale. All that sur-

vives the averaging in macroscopic measurements are the frequency components of the individual (atomic or molecular) oscillators driven by the external fields. This idea can now be extended to a higher class of an artificial structured material where the "artificial atoms" are on length-scales much smaller than the wavelength of the incident light but can be large compared to atomic or molecular length-scales. The light field thus does not resolve these individual "atoms", but responds to the macroscopic resonances of the structure. Such materials have been termed "metamaterials" [75,76] and can be characterized by macroscopic parameters such as ε and μ that define their response to applied electromagnetic fields, much like homogeneous materials.

Metamaterials, can be strictly distinguished from other structured photonic materials, i.e. photonic crystals [74]. In photonic crystals, both the size and the periodicity of the index modulations are of the order of the wavelength λ in the material. Hence homogenization in this sense cannot be carried out. The unnatural properties of metamaterials generally rely on their construction rather than their composition.

2.3.3 Metamaterial consisting of split ring resonators (SRRs)

The metamaterial concept of creating composites with desired electromagnetic properties has already enabled new possibilities for the control of electromagnetic radiation. The magnetic response of conventional materials vanishes ($\mu = 1$) at infrared or higher frequencies, since magnetic polarization in natural materials follows orbital currents or unpaired electron spins which are resonant in the GHz-region. In contrast, significant electric polarization can only happen in THz-frequencies due to the resonant behavior of electric excitation modes. Therefore, one motivation of metamaterials design is to shift electric resonances of natural materials (particularly metals), expressed via $\varepsilon(\omega)$, to lower frequencies. The other motivation is the creation of magnetic resonances, described by $\mu(\omega)$, at frequencies higher than those present in naturally-occurring magnetic materials. More specifically, the region of interest lies between the THz and the visible parts of the spectrum. Along this line, the scientists have successfully developed metamaterials with a negative index of refraction composed by split-ring resonators (SRR) as shown in Figure 2.8.

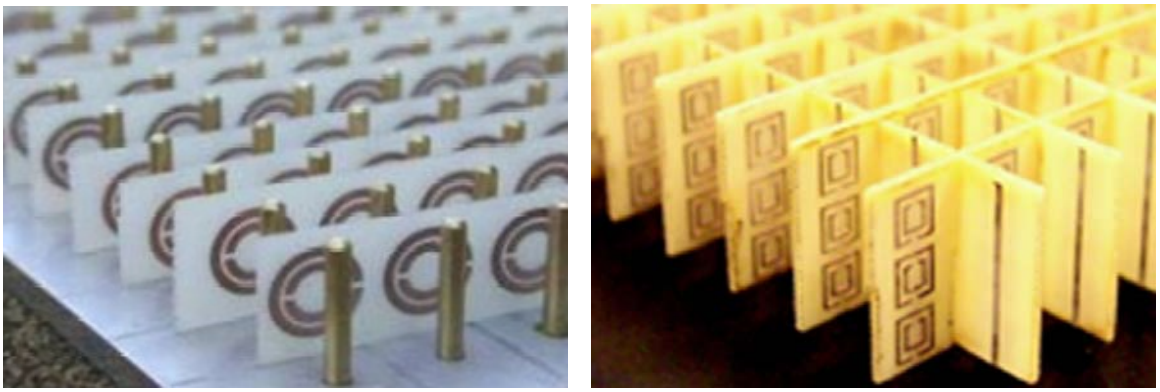

Figure 2.8 Photographs of left-handed metamaterial array configuration [77-79].

The design of this SRR structure is for the purpose of forming a circular current which generates a magnetic-dipole moment perpendicular to the SRR. If a closed ring in which the current can

flow is used, one can only couple to the magnetic dipole moment via the magnetic field. In order to efficiently couple to the ring current via the electric field [80], one has to introduce a capacitance into the structure design. This is realized by the small slit in the ring (see Figure 2.8). Metamaterials used in this work are composed of arrays of SRR with a simple form of a planar conductive 'U' shape ring as shown in Figure 2.9. Here, the SRR acts as a sub-wavelength *LC* oscillator of eigenfrequency ω_{LC} with $\omega_{LC} = (LC)^{-1/2}$, consisting of a magnetic coil with inductance *L* and a capacitor with capacitance *C* (Figure 2.9 (e)).

Based on the basic knowledge, it is obvious that an incident electromagnetic wave only excites the magnetic resonance of a resonator through its magnetic field. Thus, one could conclude that the magnetic resonance appears only if the external magnetic field **H** is perpendicular to the SRR plane, which in turn implies the propagation direction parallel to the SRR (Figure 2.9 (a) and (b)) [80]. While no coupling to the magnetic resonance was expected if **H** is parallel to the SRR (Figure 2.9 (c) and (d)). However, this is not always the case. According to Ref. [80], an incident electric field parallel to the gap-bearing side of the SRR (Figure 2.9 (c)) can also induce a circulating current – in which case the mirror symmetry of the SRR with respect to the direction of the electric field is broken by the gap of its ring. Thus, the normal incident light can couple to the *LC* resonance, if at least one of the following conditions is fulfilled: (i) The electric field vector **E** of the incident light has a component normal to the plates of the capacitor (Figure 2.9 (b) and (c)), or (ii) the magnetic field vector **H** of the incident light has a component normal to the plane of the coil (Figure 2.9 (a) and (b)) [39]. If condition (ii) is fulfilled, the current in the coil, analogous to an atomic orbital current, leads to a magnetic field that counteracts the driving magnetic field, which can lead to a negative permeability [39]. In Figure 2.9 (d) only the electric resonance can be excited.

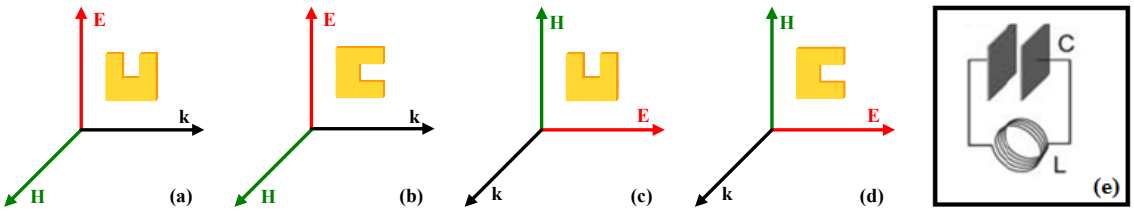

Figure 2.9 (a) - (d) The four studied orientations dependence of SRR with respect to the incident fields k, E, H of the incident electromagnetic wave. The two additional orientations, where the SRR are on the H-k plane, produce neither electric nor magnetic resonance. (e) SRR can be mimicked as a *LC* circuit with inductance *L* and capacitance *C*.

In this work, a normal incident light is used as shown in Figure 2.9 (c) and (d). With a horizontally polarized light (see Figure 2.9 (c)), the electric field could couple to the capacitance of the SRR and induce a circulating current in the coil leading to a magnetic-dipole moment normal to the SRR plane and opposing the external magnetic field, hence $\mu<0$. As shown in the transmission versus wavelength curve Figure 2.10 (a), those two measured resonances are corresponding to the electric and magnetic resonances, respectively. The magnetic resonance disappears if the incident light is polarized vertically (see Figure 2.9 (d)) as shown in Figure 2.10 (b). In the latter case, the electric field of the light leads to a charge accumulation at the surfaces of the vertical SRR arms, resulting in a depolarization electric field. Depending on the permittivity of the metal, also depending on the frequency of light, this depolarization field can enhance or suppress the external electric field. And therefore, a negative permittivity, ε, can be obtained.

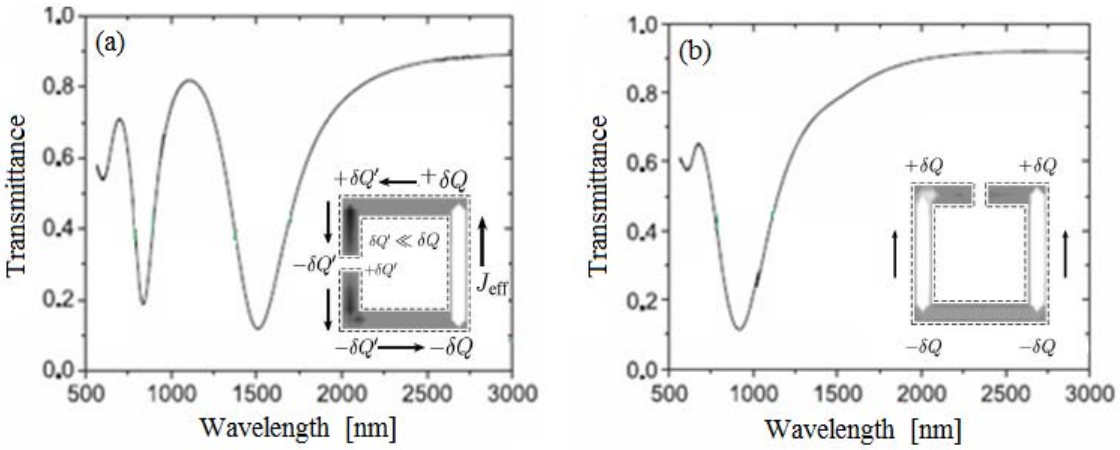

Figure 2.10 The normal-incidence transmission spectra of split ring resonators for horizontal and vertical polarization are shown in (a) and (b), respectively. In (a), one can couple to the fundamental magnetic mode at 1500 nm wavelength via the electric-field component of the incident light; while in (b), one cannot [46]. Insets are the simulation results of charge density distribution from Ref. [80].

2.3.4 Transmittance

In optics and spectroscopy, transmittance is the fraction of incident light at a specified wavelength that passes through a sample, which is defined by [81,82]

$$T \equiv \frac{I}{I_0} \tag{2.25}$$

where I is the transmitted intensity and I_0 is the incident intensity. This is sometimes explicitly written as a percentage [81],

$$T \equiv \frac{I}{I_0} \times 100\% \tag{2.26}$$

The transmittance depends on the path length or sample thickness, the absorption coefficient of the sample, the reflectivity of the sample, the angle of incidence, the polarization of the incident radiation, and, for particulate matter, on particle size and orientation [83].

3 Experimental procedures

3.1 Electrochemical measurements

The electrochemical cells were made of glassware or quartz, and before any experiment all of the cells in this work were immersed in a standard cleaning solution (5 volume parts concentrated H_2SO_4 + 1 part 30% H_2O_2) for 24 hours and then rinsed thoroughly with ultrapure 18.2 MΩ cm grade water (Arium 611, Sartorius) to remove adsorbed ions. The same water, plus NaF powder (Suprapur, Merck) or other high purity concentrated solution, was used to prepare the electrolytes with different concentrations. All electrochemical measurements were performed at room temperature (except for in-situ X-ray measurement) under potential control by a potentiastat.

3.1.1 Reference electrodes

Except for the dealloying experiment, all the potentials indicated in this work are given versus standard reference electrode (RE) consisting of Ag/AgCl in saturated KCl solution (+200 mV vs. the standard hydrogen electrode (SHE)). Before and after each measurement, the potential readings of the RE were verified by comparison to fresh ones. The variation was within the range of 10 mV.

One special homemade RE was used for the dealloying experiment, which is called pseudo Ag/AgCl RE. The pseudo Ag/AgCl reference electrode was prepared by oxidizing a Ag wire (0.5 mm diameter, Ag 99.99%, ChemPur) at 0.9 V for about 120 s in 1 M (mol/L) aqueous HCl solution – during this preparation, another Ag wire with larger surface area served as both reference and counter electrode. The potential of this pseudo Ag/AgCl RE with respect to the standard Ag/AgCl in saturated KCl solution is 330 mV measured in 1 M $HClO_4$, and therefore its potential versus SHE is 530 mV.

3.1.2 Luggin capillary

A Luggin capillary (Figure 3.1) is used in electrochemical cell measurements to reduce toward zero what is called "the *IR* error [64]." There is no potential drop in the tube leading from the reference electrode to the end of the Luggin tube. The Luggin tip is at the potential of the solution

in contact with the electrode. Then the potential difference relevant to an "electrode potential" measurement is that between the interior of the working electrode (WE) and that of the solution. One should not press the Luggin capillary against the WE because that would shield a part of the WE from receiving the normal current density. Suppose the solution-filled space between the WE and the tip of the Luggin capillary is of resistance *R* and the current on the electrode is *I*. To reduce this "ohmic error, *IR*", one should keep the Luggin open tip as close as possible to the WE.

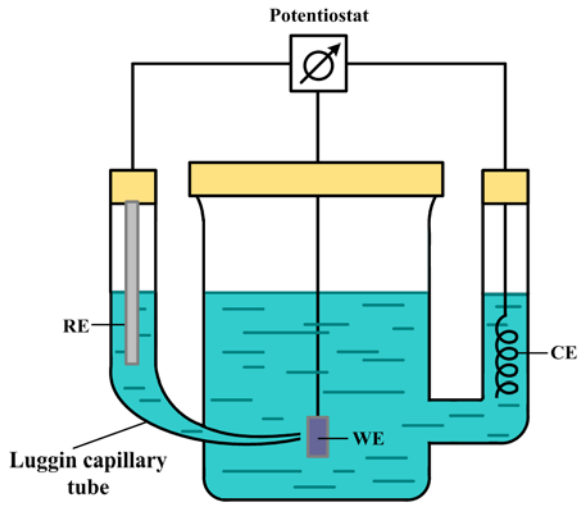

Figure 3.1 Schematic illustration of the electrochemical cell with a luggin capillary, whose tip is close to the working electrode.

3.2 Samples

3.2.1 Nanoporous gold

3.2.1.1 Silver and gold alloy preparation

The master alloy $Ag_{75}Au_{25}$ (at.%) was prepared by arc melting (Arc Melter MAM-1, Edmund Bühler) Au and Ag wire (Au 99.995% and Ag 99.99%, ChemPur). The Au-Ag system was of interest because both of Au and Ag have face-centered-cubic structures with similar lattice parameters and exhibit solid solubility across the entire composition range. The ingots (~3 g) were sealed in an evacuated (10^{-6} mbar) quartz tube and then homogenized by annealing at 950 °C (CTF model furnace, Carbolite) for 80 hours. After homogenization, ingots were rolled to form ~1 mm thick sheets (Duo rolling mill, Schmalz), from which ~10 mm×10 mm squares were cut by a diamond wire cutting machine (Model 3032, Well). Finally, the samples were annealed for 2 h at 650 °C in Ar flow for recovery.

3.2.1.2 Nanoporous gold from dealloying

The nanoporous gold (npg) samples used in this work were prepared by dealloying. The process of dealloying involves selective removal of one component from a binary or ternary solid solution, resulting in a solid skeleton interspersed with pores or voids. Dealloying can be carried out either by applying a suitable potential in an electrochemical cell or immersing the alloy in strong oxidizing electrolytes, e.g. acids. By varying dealloying conditions or by post-dealloying treatments, it is possible to prepare nanoporous structures of different length scale. One can find details about dealloying for preparing nanoporous metal material in Parida's PhD dissertation [84].

In the present work, the dealloying was performed at 0.75 V vs. pseudo Ag/AgCl RE, which was separated from the working electrode (WE) compartment by a luggin capillary in order to reduce the "the *IR* error" and also to avoid the diffusing Ag covering the RE (see Figure 3.1). The electrochemical cell was made of glassware, and the Ag wire was used as counter electrode (CE). All the electrochemical dealloying was performed in freshly prepared 1 M $HClO_4$ (Suprapur, Merck) at room temperature under potential control using a potentiostat (Eco Chemie, Autolab). The dealloying was interrupted when the current fell to 10 μA at which time nearly all the Ag was removed from the alloy. The dealloying time depended on the applied potential [85] and sample size, e.g., a large sample ($10\times10\times1$ mm^3) needs 2-3 days while it only takes 6-10 hours for a $1\times1\times2$ mm^3 small sample.

3.2.1.3 Characterization of nanoporous gold

A field-emission scanning electron microscope (SEM; LEO 1530) operated at 20 kV was used for pore structure characterization. The typical microscopic structures of nanoporous gold samples prepared by dealloying are shown in Figure 3.2. These images show that the material consists of tortuous, branched filaments, with a typical ligament size of 40±5 nm for the bulk structures (see Figure 3.2(a) and Figure 3.2(b)), and 35±5 nm for the surface structures (Figure 3.2(c)).

A npg sample is cut in the middle, then the newly formed surface on the cross-section is called fracture surface here (Figure 3.2(a)). This fracture surface represents the interior state of the npg sample. Figure 3.2(b) is taken from the border between the fracture surface and the original surface, which is called near surface here. And Figure 3.2(c) is taken for the pure original surface. Those SEM images show a small difference between the ligament sizes. Energy-dispersive X-ray spectroscopy analysis from the same machine shows that nearly no Ag (less than 1%) residues in these npg samples.

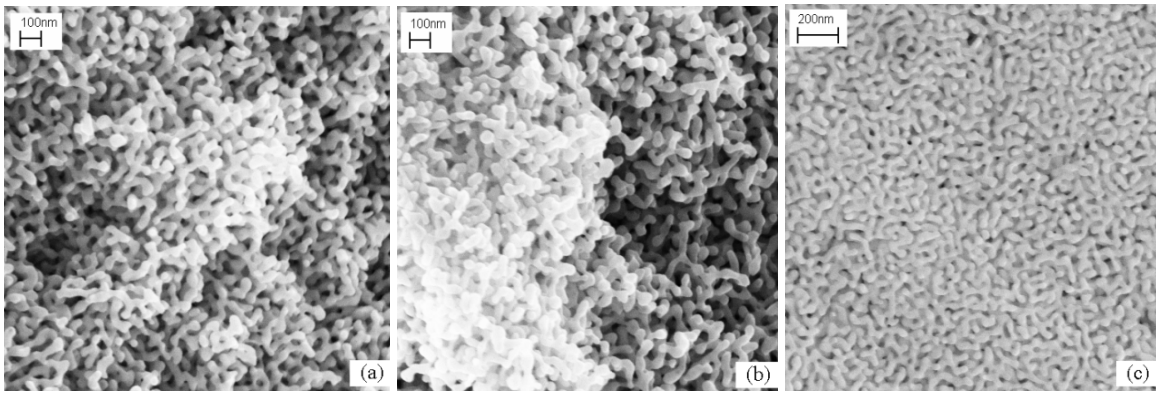

Figure 3.2 Scanning electron microscopy images of nanoporous gold sample prepared by dealloying. (a) fraction surface. (b) near surface. (c) surface of npg sample.

3.2.2 Carbon aerogels (CAs)

Carbon aerogels (CAs) samples used in this study are produced at Lawrence Livermore National Laboratory at California in USA by Dr. J. Biener and Dr. T. F. Baumann. The scientists from Dr Biener's group did some basic characterization like measuring the mass-specific surface area via the BET method and analyzing the structure size from scanning electron microscopy as shown in the following paragraph.

The synthesis and activation of the CA materials have been reported in the literature [86]. Specifically, the materials were prepared through the sol-gel polymerization of resorcinol (R) and formaldehyde (F) (R/F molar ratio = 0.5) using acetic acid as the catalyst to produce organic gels that are supercritically dried and subsequently pyrolyzed at 1050 ^{o}C in an inert atmosphere. The monolithic carbon aerogels were then activated under a carbon dioxide atmosphere at 950 ^{o}C. The surface area was determined using an ASAP 2010 Surface Area Analyzer (Micromeritics Instrument Corporation). Samples of approximately 0.1 g were heated to 300 ^{o}C under vacuum (10^{-5} Torr) for at least 24 hours to remove all adsorbed species. Nitrogen adsorption data were then taken at five relative pressures from 0.05 to 0.20 at 77 K to calculate the surface area using the Brunauer-Emmett-Teller (BET) theory. The result for the mass-specific surface area was 2800 m^2/g.

A picture of macroscopic bulk CAs is shown in Figure 3.3 (a) and also a SEM image in Figure 3.3 (b) shows that the skeletal structure of CAs defining a continuous porous network consists of interconnected carbon ligaments [86]. These ligaments appear to be made up of spherical primary particles that have fused together during network formation, which shows that CAs having similar morphology to nanoporous metal. The bulk density, ρ, of the carbon aerogel, determined by measuring the dimensions and mass of the monolithic sample, was 0.14 g/cm^3. Assuming, for the purpose of a rough estimate, that the mass density of the solid phase is similar to graphite, ρ_0 = 2.1 g/cm^3, the solid volume fraction, φ, is estimated at around 0.07.

As working electrodes, ~1x1x2 mm^3 cuboid CA samples with a typical mass of 0.38 mg are used. The same material was used as counter electrode but with an at least 5 times bigger volume. The

bulk glassy carbon sample used as a reference is a cylinder (diameter 3 mm, length 10 mm) of high purity material (SIGRADUR®G, HTW, Germany), which is shown in Figure 3.3 (c).

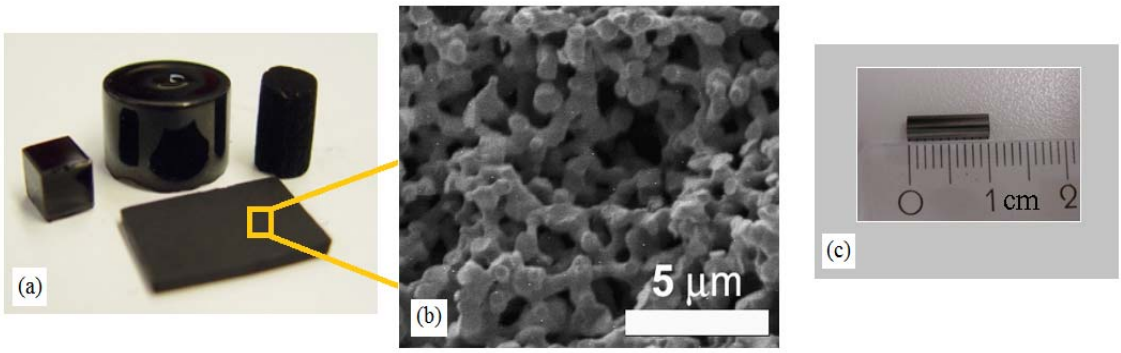

Figure 3.3 Pictures of carbon materials used in this work. (a) Macroscopic picture and (b) Scanning electron microscopy images of carbon aerogels [86]. (c) Picture of glassy carbon cylinder sample used as a reference for *pzc* test.

3.2.3 Gold nanostructure photonic metamaterials

This part of work was performed in close cooperation with the Institute of Applied Physics at Karlsruhe Institute of Technology (KIT), and the metamaterial samples used here were fabricated by M. Ruther from Prof. M. Wegener's group.

The metamaterials consisted of arrays of gold split-ring resonators [39] (SRR) and each array had a footprint of 80 µm × 80 µm (see Figure 3.4 (a)). The aqueous electrolyte is opaque in the near-infrared (i.e., for wavelengths larger than 1.4 μm, equivalent to frequencies below 214 THz). Hence, the SRR sizes were chosen such that the resonances of interest lie in the range from visible light to the beginning of the near-infrared part of the electromagnetic spectrum (i.e., from 0.5 μm to 1.4 μm). This leads to SRR side lengths in the order of 100 nm as shown in Figure 3.4 (b). The SRR arrays have been fabricated using a lift-off procedure following standard electron-beam lithography [87] on glass substrates coated with a 10 nm thin film of indium tin oxide (ITO) and a 2 to 3 nm thin Cr film as adhesion layer. Because thin ITO films are transparent in the region from infrared to ultraviolet wavelengths, it is a suitable conductive material for our experiments. The ITO film provides the electrical contact to the gold nanostructures, which form the working electrode in our electro-modulation experiments. Additional results (not shown here) were obtained with a series of samples deposited without the Cr layer. These samples tended to detach after repeated electrochemical cycles, but the results were otherwise consistent with those obtained with the Cr layer. All films (ITO, Cr, and Au) are made using high-vacuum electron-beam deposition. Gold is deposited at a rate of 0.1 nm/s. The average film thicknesses are determined by atomic-force microscopy (AFM Nanoscope Multimode, Veeco Instruments, USA) by M. Ruther at KIT.

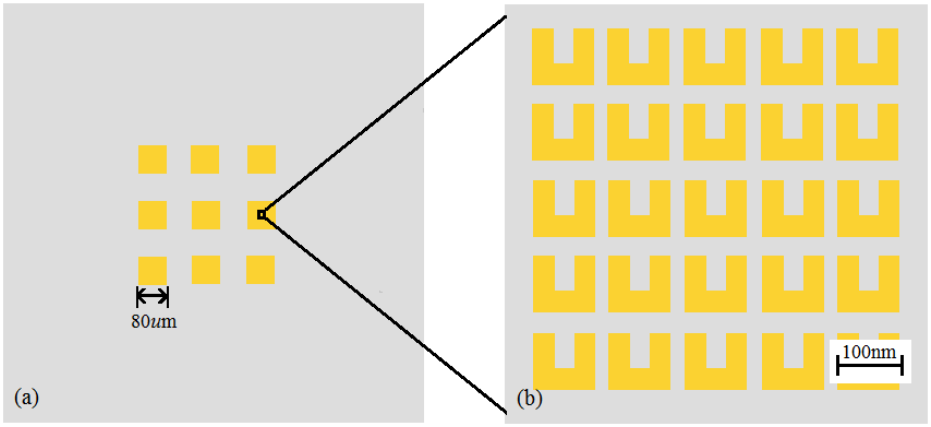

Figure 3.4 Schematic images of a metamaterial sample cosisted of arrays of gold split-ring resonators (yellow) on glass substrate (grey). Note that each array has a footprint of 80 μm × 80 μm, and the feature size of each SRR structure is at about 100 nm.

3.3 Measurement setups

3.3.1 In-situ wide-angle x-ray diffraction (XRD) experiment setup

All x-ray diffraction (XRD) measurements were performed in Bragg-Brentano geometry with a stationary sample in the horizontal focal plane (θ-θ geometry) using a solid state detector on a Philips X'pert diffractometer. In order to penetrate the sample surface as deep as possible, a sealed Mo anode was used rather than a Cu one. Within the range of scattering angle under investigation, the depth of penetration of Mo Kα radiation in npg is between 3 and 10 μm. The scattering thus provides a probe for bulk behavior.

The electrochemistry cell for the in-situ XRD measurement is shown in Figure 3.5. We used a teflon cell with a capacity of ~16 ml, a thin gold wire was mounted between the screw holder and the sample to connect to the potentiostat (VoltaLab PST 050, Radiometer Analytical). The temperature of the cell is controlled at 14 °C by a thermostat and the cell has a gas proof cover as shown schematically in Figure 3.5(a). Diffraction measurements at constant potential were started after the electrode current became stationary. In order to get good statistics, at each potential value we used 4 hours to measure the Bragg diffraction angle from 14° to 66° (angle step is 0.03°).

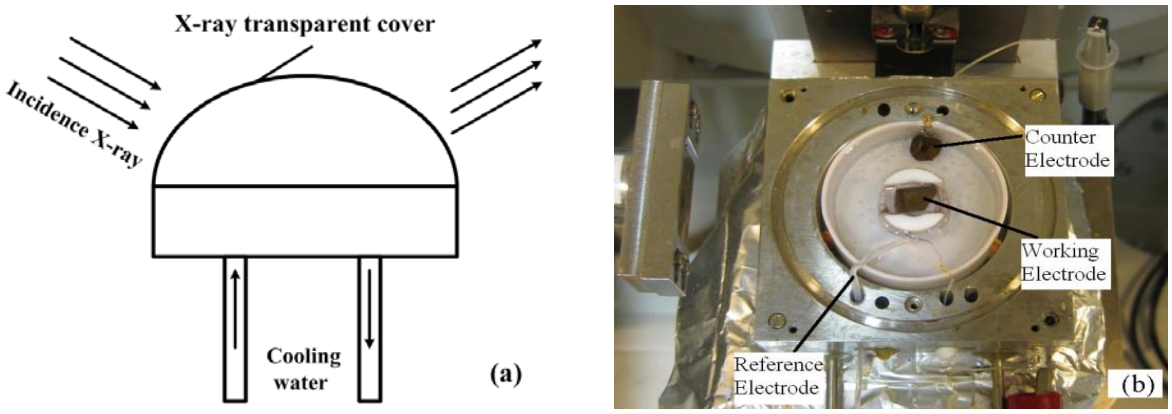

Figure 3.5 In-situ wide-angle x-ray diffraction (XRD) measurement setup. (a) A schematic graph of the setup. (b) A picture of the electrochemical cell arrangement.

3.3.2 In-situ dilatometry experiment setup

The schematic illustration of the in-situ dilatometry setup for strain measurement during cyclic voltammetry is shown in Figure 3.6. The dilatometer (Linseis) has a vertical pushrod with a sensitivity of ca. 5 nm. A cuboid sample was mounted between support and pushrod in an electrochemical cell with 10 ml volume. The sample length change was transmitted to an inductive displacement sensor via the pushrod loaded by a fixed contact pressure of 20 cN. For the samples with 1 mm^2 area, the stress exerted by the dilatometer probe was about 0.2 MPa, insignificantly small compared to the yield strength of nanoporous gold (~100 MPa) [88].

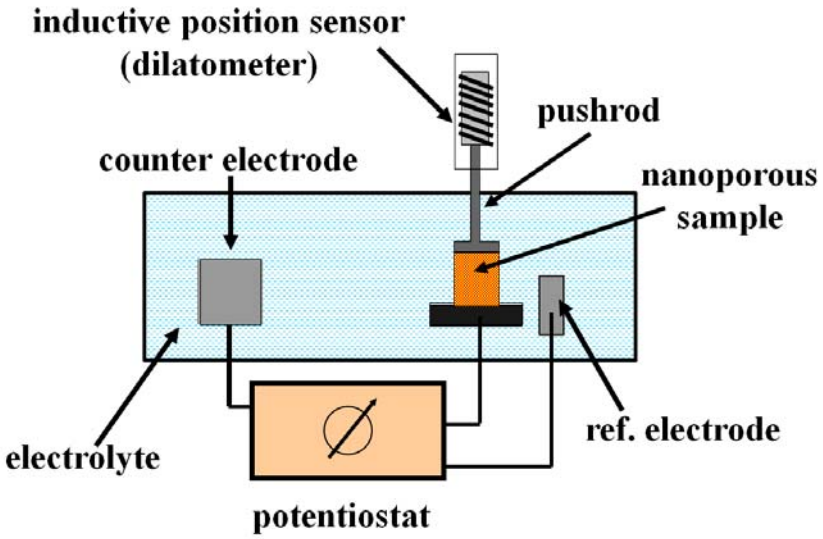

Figure 3.6 A schematic illustration of the (vertical) dilatometer equipped with an electrochemical environment.

3.3.3 Electrochemical setup for impedance measurement

The electrochemical cell used for impedance measurement is the same as the one used for dealloying as shown in Figure 3.1. The reference electrode for impedance application (Ag/AgCl in saturated KCl, Radiometer Analytical, XR820) was separated from the working electrode compartment by a luggin capillary. Before and during impedance measurement of CAs, the electrolyte was deaerated by bubbling with ultrapure argon. Electrochemical impedance spectra (EIS) were measured from 3 mHz to 200 Hz with a sinusoidal voltage perturbation of 5 mV by using a computerized potentiostat (Eco Chemie, Autolab), and the bias potential scan rate was 0.001 mV/s.

Here, we focused on pure capacitive double-layer charging with minimum contributions from pseudocapacity (capacity from specifically adsorbed ions, whose charge can be transferred to the sample). Thus, the NaF aqueous electrolyte is chosen as fluoride anions are known to show little specific adsorption on CA surfaces near the *pzc* [89]. Because the number density of adsorbates per charge decreases with increasing dilution [90], electrolytes are comparatively dilute though of sufficient concentration to allow a useful amplitude of q and, hence, measurable sample length changes.

3.3.4 In-situ optical measurement setup

The transmittance setup was home-built by Prof. Wegener's group at KIT and developed for visible and near-infrared wavelengths as schematically shown in Figure 3.7 (a). Light from a 100 W power tungsten halogen lamp serves as light source, which is focused into a multimode optical fibre with a 200 μm core by the lens L1 to be transmitted to the actual transmittance setup. The collimated beam from lens L2 passes through a Glan-Thompson polarizer P and a circular aperture CA. Then the linear polarized light is controlled and finally focused onto the sample by the microscope objective MO1. In this work, the full opening angle of the cone of light is 5 degrees, approximating very nearly normal-incidence conditions. The electrochemical cell which contains the sample is mounted on a goniometer placed on a rotation stage, hence the sample can be aligned strictly perpendicular to the incidence axis. Lens L3 in combination with the objective MO2 is used to image the sample onto a rectangular knife-edge aperture KE where only the relevant part of the sample is selected for detection. In order to align the sample with respect to the foci of the microscope objectives MO1 and MO2 and to adjust the KE in the intermediate image plane, the kinematic mirror KM can be introduced into the setup to image the intermediate image plane via lens L5 onto an infrared CCD camera (CCD, Panasonic) with a magnification of ~ 62.5x [91]. Finally, via a microscope objective MO3, the light transmitted through the selected area of the sample can be coupled into a second optical fibre attached to an optical spectrum analyzer (OSA, Acton SP2300, Princeton) with a spectral range from 0 to 1400 nm. The transmittance spectra were measured by the OSA in-situ.

A schematic graph of the in-situ measurement setup and a photo of the electrochemical cell are shown in Figure 3.7 (b) and (c), respectively. The electrochemical cell is a quartz glass cuvette (5 mm electrolyte thickness, Hellma Analytics) filled with 0.7 M aqueous solution of NaF (Suprapur, Merck) and open to air. The metamaterial sample is fixed on a homemade teflon sample holder and connected to the potentiostat by a thin gold wire (0.1 mm diameter, Au 99.995%, ChemPur). The sample immersed in the solution is perpendicular to the incident beam and its

potential – as measured relative to a standard reference electrode (RE), Ag/AgCl in saturated KCl solution (DRIREF-2SH, WPI) – is controlled by a commercial potentiostat (VoltaLab PST 050, Radiometer Analytical). A macroscopic gold spiral (0.5 mm diameter, Au 99.995%, ChemPur) was used as the counter electrode within the electrolyte. The normal-incidence intensity transmittance spectra were recorded at constant potential, after the electrode current became stationary. Normalization of the transmittance spectra is with respect to the bare ITO-coated substrate, i.e., without the Cr/Au nanostructures, in the same electrochemical cell.

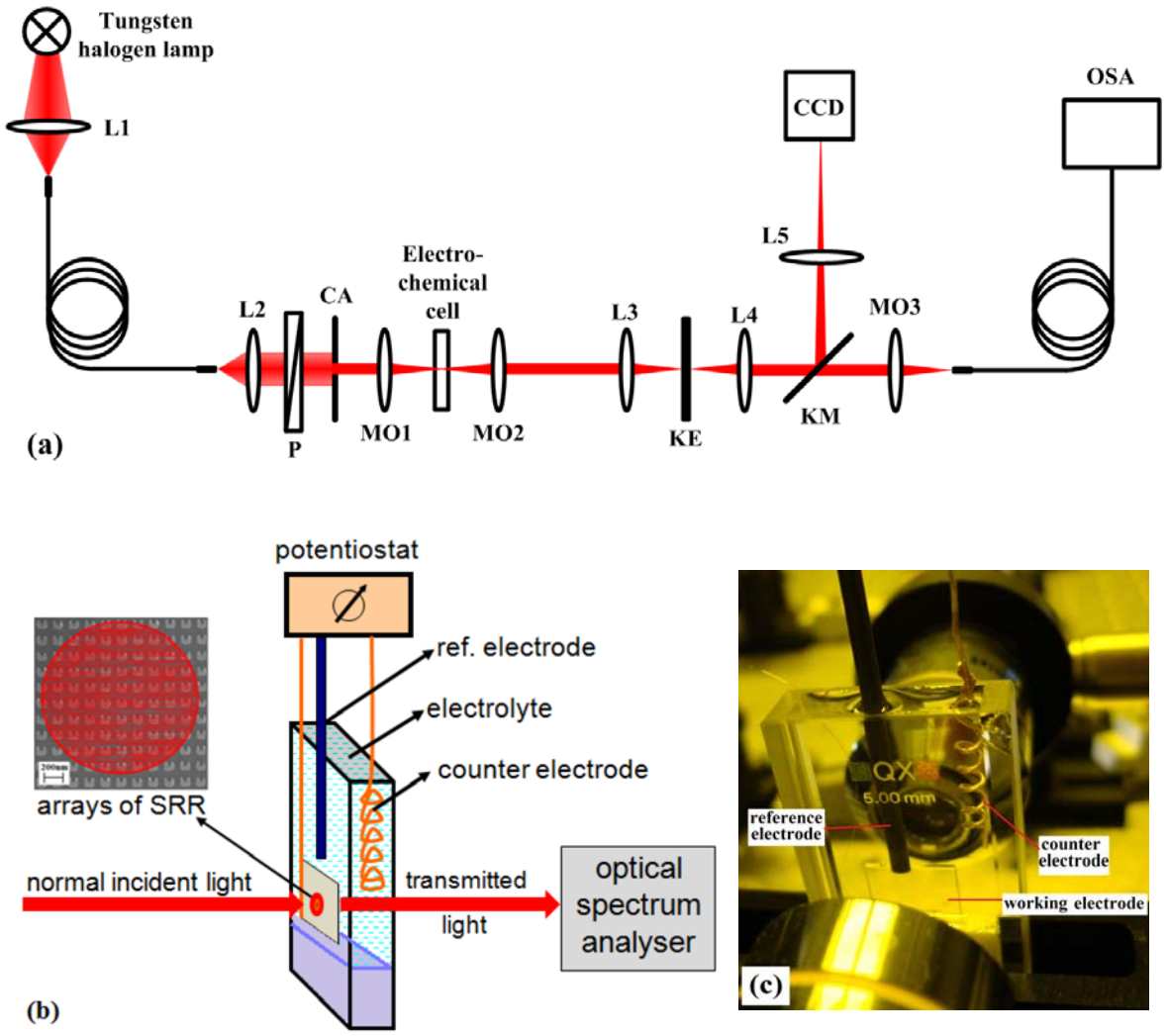

Figure 3.7 Schematicly illustrated in-situ optical measurement setup. (a) A homebuilt transmittance measurement setup. Light from power tungsten halogen lamp is focused into a multimode optical fiber by lens L1. The collimated beam from lens L2 passes through polarizer P and a circular aperture CA. Through the microscope objective MO1, the linear polarized light is controlled and finally focused onto the electrochemical cell which contains the sample. Combining lens L3 with the objective MO2 the sample is imaged onto a rectangular knife-edge aperture KE where only the relevant part of the sample is selected for detection. For alignment, a kinematic mirror KM used to image the intermediate image plane via lens L5 onto an infrared CCD camera. Finally, via microscope objective MO3, the light can be coupled into a second optical fibre attached to an optical spectrum analyzer, with which the transmittance spectra are measured. (b), (c) Schematic illustration and a photograph of the electrochemical cell.

4 Electrically tunable actuators

The research and potential applications of nanoporous material will be discussed in this chapter, which includes two parts. In the first part, an experiment is designed to figure out the mechanisms for capillarity-driven deformation of nanoporous metal through in-situ dilatometry and in-situ wide-angle x-ray diffraction (XRD) measurement. In the second part, the electrochemical and electromechanical properties of nanoporous carbon aerogels are investigated through impedance measurement and in-situ dilatometry and a tunable electrochemical carbon aerogel actuator is presented.

4.1 Capillarity-driven deformation of porous metals

Nanoporous gold (npg) made by alloy corrosion is an interconnected network of solid ligaments that resembles the long thin fibres of the theory introduced in section 2.2.2. Therefore, npg has been used as a means of probing and illustrating the differences between the various strain parameters. In the experiments in this chapter, the pore space is completely filled with an aqueous electrolyte at constant pressure, $P_F = 1$ atm. By connecting the sample as an electrode to the potentiostat and controlling the electrode potential, E, the surface stress, f, can be changed reversibly. This is done in-situ in dilatometry and x-ray diffraction setups.

In this section, in order to figure out the mechanisms for capillarity-driven deformation of nanoporous metal, an experiment is designed to illustrate the important distinction between different strains through: (1) dilatometry to probe the resulting change in macroscopic sample dimension and (2) in-situ wide-angle x-ray diffraction to probe the variation in the lattice parameter of the gold crystal lattice. The two strain measures assume significantly different values. The results do confirm the fundamental difference between the strain in response to the action of the surface stress at the solid surface and the strain in response to changes in the pressure in the fluid.

4.1.1 Experimental results

4.1.1.1 Method for analysis the lattice parameter change

All Bragg reflections correspond to face-centred cubic gold, as shown in Figure 4.1. No signature of oxide has been identified throughout the experiments. The narrow peak agrees with previous observations of a large (10-100 μm) grain size, so that the crystal lattice is coherent on a scale

much larger than the ligament size [17,92]. From the inset of Figure 4.1, we can see that repeating the diffraction experiment at a different electrode potential leads to a displaced reflection pattern.

We now turn to the evaluation of the associated strain. Usually the scientists decide the absolute value of lattice parameter from the peak positions of the diffraction spectrum [93]. This method might have an error, which is larger than the shift of lattice parameter caused by the strains which are expected in our experiment. However, in this work, only the relative rather than the absolute value is concerned, therefore a full pattern correlation technique is employed here as it yields very good resolution and reproducibility in the relative change, $\varepsilon = \delta a/a$, of the lattice parameter, a. This analysis exploits the scaling of the interference function, $S(q)$, during an isotropic and affine stretch of magnitude ε. Firstly, the scattering angle, θ, is converted to the scattering wavenumber, q, through the relation $q = 4\pi\lambda^{-1}\sin\theta$ with λ the wavelength. As $a \rightarrow a\,(1+\varepsilon)$, we have $S(q) \rightarrow S(q')$ with $q' = q\,(1+\varepsilon)$. Ignoring the atomic form factor and polarization function, which vary slowly with θ, $S(q)$ has been computed – except for a constant scaling factor that can be ignored – from the experimental intensity $I(\theta)$, using $S(q) \propto I(\theta)\,\mathrm{d}\theta/\mathrm{d}q \propto I(\theta)\sec\theta$. The strain magnitude ε is then obtained by minimizing

$$\chi^2 = \Sigma_k (S(q_k) - S_0(q_k\,(1+\varepsilon)))^2 \qquad 4.1$$

with respect to ε; the summation is over the set of experimental q-values. The computation requires interpolated values of the interference function, S_0, of a suitable reference scattering data set at the scattering numbers $q'_k = q_k\,(1+\varepsilon)$. The reference data set is one from the series of diffraction data taken with the same sample but at different potentials, from which it can be arbitrarily chosen. In this way we could determine ε – relative to the arbitrary reference state – to a precision of 1×10^{-5}, as estimated from the reproducibility of ε during cyclic variation of the potential. Extra data analysis using a full pattern correlation technique with Mathematica version 6.0 is given in the Appendix.

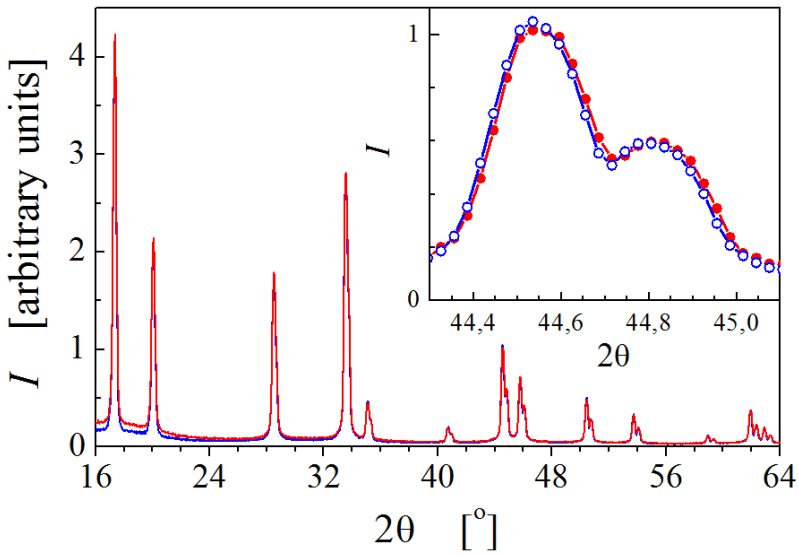

Figure 4.1 X-ray diffraction patterns (obtained with Mo $K_{\alpha1/2}$ radiation) of intensity, I, versus scattering angle, 2θ, at electrode potentials 1.35 V (blue, open symbols) and −0.2 V (red, solid symbols). The insert shows the details of the $K_{\alpha1/2}$ split (331) reflection doublet, illustrating the shift in position.

Figure 4.2 shows two characteristics of potential cycles, namely the cyclic voltammograms (CVs) and the lattice parameter changes. The significant features in the CVs are the OH-adsorption peaks during potential scans going in positive direction and the corresponding desorption peaks during scans going in negative direction. The small current outside these features indicates dominantly capacitive double-layer processes. The two aqueous electrolytes used, 1 M $HClO_4$ and 0.7 M NaF, are distinguished in particular by the different hysteresis between the adsorption and desorption peaks. The lattice parameter changes reflect this behavior, with a noticeable hysteresis in the case of the NaF solution. Note the good reproducibility of the $\Delta a/a$ values, which testifies the accurate resolution of the lattice strain.

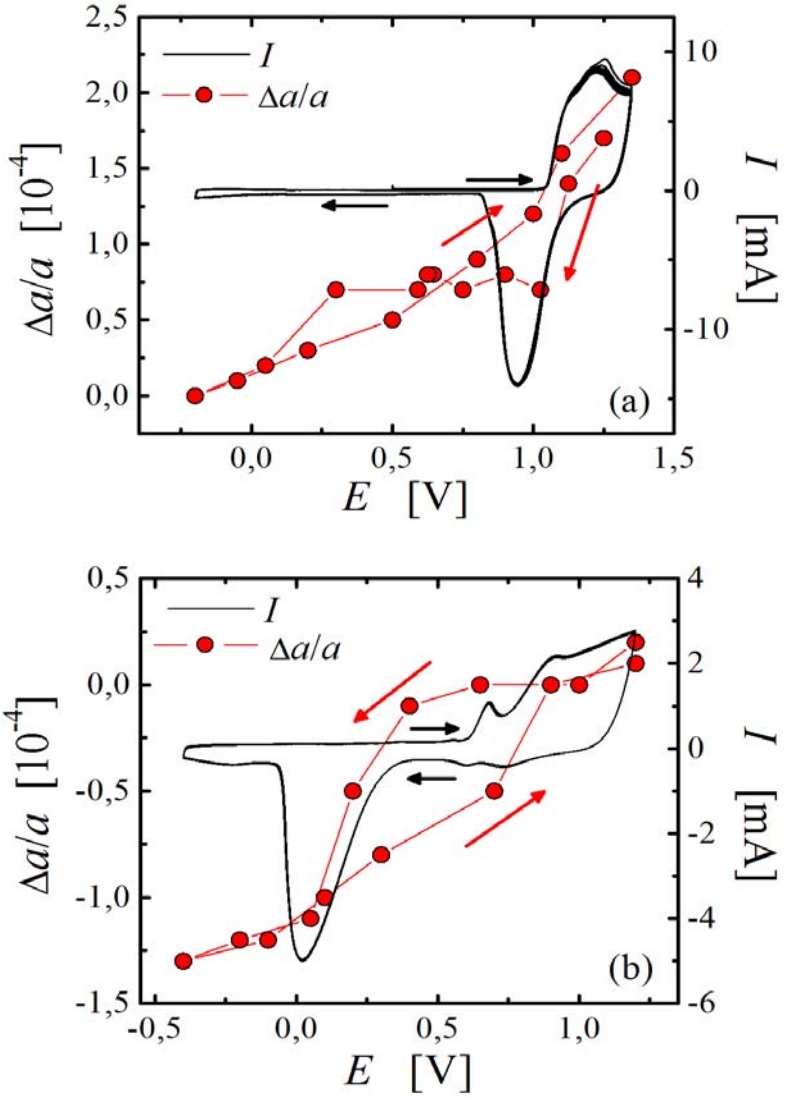

Figure 4.2 The voltage-induced strain $\Delta a/a$ (relative to an arbitrary reference state) and the cyclic voltammogram measured (a) in 1 M HClO4, scan rate 0.5 mV/s, (b) in 0.7 M NaF, scan rate 0.2 mV/s.

After repeating the in-situ X-ray diffraction (XRD) measurements for more than ten cycles, the reproducibility of the behavior is found to be very good, but its magnitude becomes smaller dur-

ing long time measurements. Nanoporous gold is known to coarsen slowly during electrochemical cycling, with a concomitant reduction in specific surface area and, hence, strain amplitude [85, 92]. In order to speed up the experiment and to minimize coarsening, a reduced number of potential values per cycle (the vertex potentials plus one intermediate value) were used for in-situ diffraction. In order to ensure comparability, dilatometry samples (~1×1×1 mm^3 in size) were cut from the larger samples of the diffraction measurements, either before or after completing an in situ diffraction potential cycle. A set of diffraction and dilatometry experiments with identical potential time history was then run in parallel. The results are summarized below:

4.1.1.2 Nanoporous gold sample measured in 1 M $HClO_4$

A freshly dealloyed npg sample is measured in 1 M $HClO_4$ with the potential range from −0.2 to 1.35 V in this subsection.

1st cycle: A dilatometry sample was cut out before the XRD measurement. The peak-to-peak strain amplitudes are $\Delta l/l = 0.041(2)\%$ for dilatometry and $\Delta a/a = 0.019(1)\%$ for diffraction as shown in Figure 4.3(a) and Figure 4.3(b), respectively. For the in-situ dilatometry measurement, the chrono-amperometry method (see subsection 2.1.4.4) is used and the potential is varied as the right ordinate axis in Figure 4.3(a). The ratio of these two amplitude values is $\Theta = 2.1(1)$.

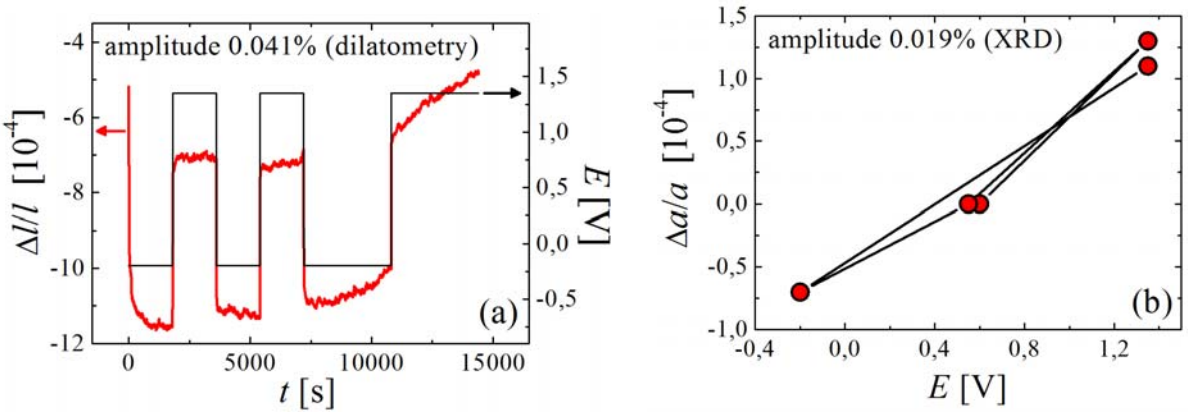

Figure 4.3 Strains Δl/l and Δa/a of a npg sample measured in 1 M $HClO_4$ during 1st cycle by dilatometer and X-ray diffraction, respectively, vs. (a) the potential variation in the time (t-) domain; (b) the electrode potential, E.

2nd cycle: The diffraction measurement was then repeated, followed by cutting out a second dilatometry sample. The results of the 2nd cycle are shown in Figure 4.4, in which the dilatometry used a continuum potential scanning (cyclic-voltammetry method). Here, it is found that $\Delta l/l = 0.036(3)\%$ and $\Delta a/a = 0.016(1)\%$. The slight decrease of the amplitudes can be attributed to coarsening. However, the amplitude *ratio* is practically identical to that of the first cycle, $\Theta = 2.3(1)$.

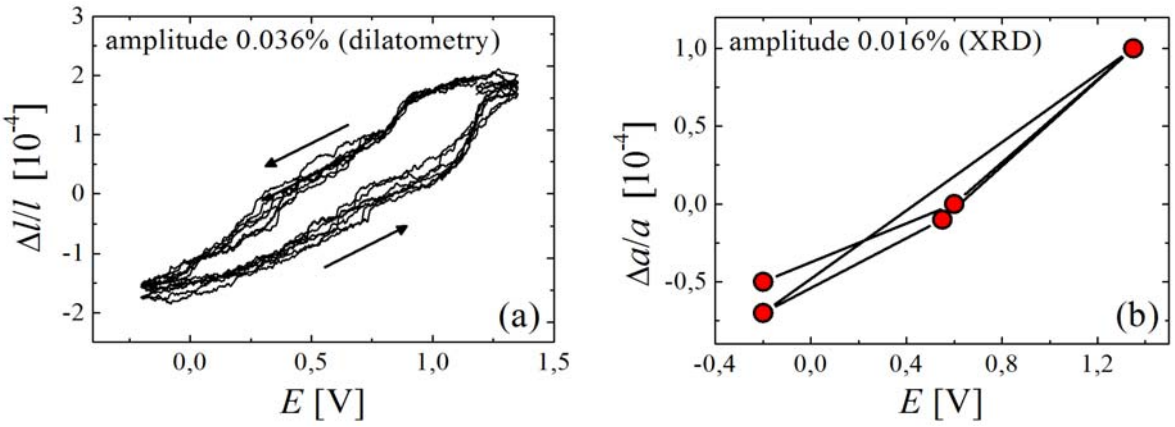

Figure 4.4 Strains $\Delta l/l$ and $\Delta a/a$ of a npg sample measured in 1 M $HClO_4$ during 2nd cycle by dilatometer and X-ray diffraction, respectively, vs. the electrode potential, E.

4.1.1.3 Nanoporous gold sample measured in 0.7 M NaF

A fresh dealloyed npg sample was first cleaned by ultrapure water and then rinsed with 0.7 M NaF solution for ten times. Fast potential cycling was carried out during rinsing with the new solution, with the objective to properly wet all pores. Then the sample was measured in 0.7 M NaF solution with a potential range from −0.3 to 1 V.

1st cycle: A dilatometry sample was cut out before the XRD measurement. The dilatometry and XRD measured peak-to-peak strain amplitudes are $\Delta l/l = 0.043(2)\%$, $\Delta a/a = 0.021(1)\%$ as shown in Figure 4.5 (a) and Figure 4.5 (b), respectively. Here, the *ratio* of the two strain amplitudes is $\Theta = 2.0(2)$ in 0.7 M NaF solution.

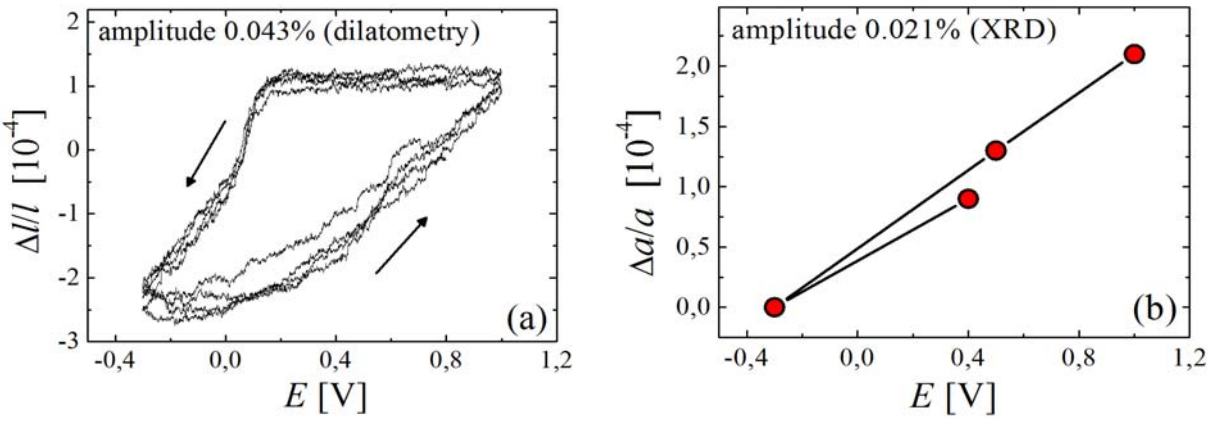

Figure 4.5 Strains $\Delta l/l$ and $\Delta a/a$ of a npg sample measured in 0.7 M NaF during 1st cycle by dilatometer and X-ray diffraction, respectively, vs. the electrode potential, E.

2nd cycle: The previous procedure of cutting a dilatometry sample after the XRD measurement was repeated here. The peak-to-peak strain amplitudes are $\Delta l/l = 0.030(1)\%$ for dilatometry and

$\Delta a/a = 0.014(1)\%$ for diffraction as shown in Figure 4.6 (a) and Figure 4.6 (b), respectively. Here again, the findings for the *ratio* of the two strain amplitudes agree closely with the previous ones, $\Theta = 2.1(2)$.

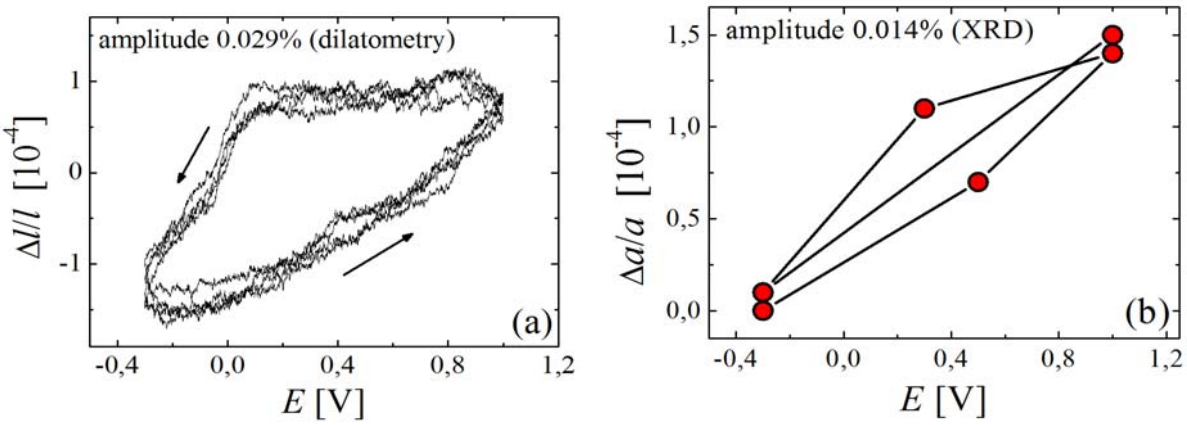

Figure 4.6 Strains $\Delta l/l$ and $\Delta a/a$ of a npg sample measured in 0.7 M NaF during 2nd cycle by dilatometer and X-ray diffraction, respectively, vs. the electrode potential, E.

4.1.2 Discussion

4.1.2.1 Comparison with results and models reported in literature

The macroscopic dimension change, $\Delta l/l$, and lattice parameter variation, $\Delta a/a$, of nanoporous gold (npg) have been measured by dilatometry and in-situ wide-angle x-ray diffraction, respectively. The resulting two strain values showed a significant difference with a ratio $\Theta \approx 2$. This effect is not compatible with the action of the Laplace pressure in the fluid, but it has a natural explanation in terms of surface stress at the solid-fluid interface, which is linked to bulk stress and strain via the generalized capillary equation for solids as introduced in section 2.2.2. The experiment results here also verified the theory given in Ref. [19], where the authors showed that the surface stress is the main driven force for the deformation of porous material. Recent studies with nanoporous metal samples of smaller ligament size than the present ones report strain amplitudes well in excess of 1% [17] in response to surface stress variation. This is more than the strain observed in capillary condensation experiments such as Refs. [13,20,21], again emphasizing that the surface stress variation may provide a major contribution to sorption strain. Indeed, the surface stress is well known to vary with the adsorbate coverage, even for surfaces in vacuum that are not subject to potential change in an electrolyte [69]. However, the strains of porous silica induced by capillary condensation or by the adsorption and desorption of a liquid have been discussed through the action of Laplace pressure alone [13,20-22]. The models used by those authors may not incorporate all the relevant microscopic interaction terms in Refs. [13,20-22]. Such models may be improved by incorporating surface stress and its origin, i.e. changes in the bond forces between the surface atoms of the solid phase.

4.1.2.2 Effects on the measured strain amplitude

In Ref. [5], the strains of a nanoporous platinum sample were measured by in-situ dilatometry and XRD in an electrolyte under an applied potential. The resulting macroscopic dimensional change was identical with the lattice parameter change of nanoporous Pt. Their nanoporous Pt samples are prepared by consolidating Pt black powder with a grain size of 6 nm, which can be modeled as a granular porous solid as introduced in section 2.2.2. With this geometry, it is natural to expect the same strains from equation 2.16. Hence, the result in Ref. [5], i.e. same strain value from different measuring methods ($\Theta = 1$) agrees well with the theoretical argument in Ref. [19].

Even though the measured strain ratio $\Theta \neq 1$ of npg in this work, the result still confirms the theory in Ref. [19]. The reason is that the macroscopic strain depends strongly on the geometry of the porous material as introduced in section 2.2.2. The npg sample used in this work just looks like a "felt" porous material consisting of an interconnected array of long thin fibers. The fibers have a circular cross-section with identical diameter and are interconnected in nodes which transmit force and displacement. From equation 2.19, we can find that with this geometry, the strain ratio Θ is only dependent on the Poisson ratio ν of the sample. For gold, $\nu = 0.44$, the ratio Θ should be as high as 7.0. And this value emerges as 5.5 from molecular dynamics simulations [19]. However, in this work the measured strain amplitude ratio Θ is ~ 2, which is considerably smaller than the theoretical value as introduced in section 2.2.2. In principle, this may relate to the finite aspect ratio of the ligaments in npg, and to the contribution of the nodes to the strain. The ligament size is different between the bulk sample and the sample surface, with about 5 nm difference in diameter. And the surface thickness is less than 0.3 μm as the SEM microstructure images show in Figure 3.2. The same phenomenon has also been observed in Ref. [94], the authors found that the surface region with a thickness of a few tens of nanometers, is characterized by features of smaller size. Under this thin surface, the bulk structure has a constant ligament size and shape. And they reported that the specific area per unit weight (and the specific capacity) is inversely proportional to the typical ligament diameter. As presented by Weissmueller, et al. [19], the specific area for a long fiber geometry assumption is $2/r$, where r is the radius of the fiber. In our case, both of the specific area and the specific capacity in the surface layer will be larger than in the bulk sample, which means the charge-induced lattice parameter change in the surface will also be larger than the bulk. However, the penetration depth of Mo Kα into npg under the scattering angle under investigation here can be up to 10 μm, which is much larger than the surface layer thickness. The ratio between the thickness of npg sample surface and the penetration depth of Mo Kα into npg is ~ 3%. In other words, using XRD we measured the average lattice parameter change of a npg of 10 μm thickness and 3% of the strain is higher than the average value. But with dilatometry, one can test the average strain from the contribution of all the ligaments inside the sample. So the effect of the microstructure difference between the surface and the bulk sample will reduce the experimentally measured strain amplitude ratio Θ, but still in reasonable error range.

4.1.2.3 Length change behavior

Different strain amplitudes have been measured by using different techniques, namely in-situ dillatometry and in-situ x-ray diffraction. But the length change behavior is comparable by comparing Figure 4.2(a) with Figure 4.4(a) and Figure 4.2(b) with Figure 4.5 (a). Both of the lattice parameter change and the macroscopic length change versus potential have similar trend, i.e. re-

flecting the different hysteresis between the adsorption and desorption peaks in the two different aqueous electrolytes, 1 M HClO4 and 0.7 M NaF.

4.1.2.4 Dealloying potential

It has been reported that the characteristic ligament size drops with increasing dealloying potential (E_D), and a very large density of defects (lattice dislocations, stacking faults, and twins) is apparent in the 0.85 V (vs. Ag/AgCl) dealloyed material [85]. In our cases, we need to do long time measurements (maybe one week or even longer), and it is easy to damage the nanoporous sample by cutting small pieces from the larger one if the sample was dealloyed at 0.85 V. In order to obtain a stable npg sample, which has fewer cracks but relatively smaller ligament size, we chose 0.75 V as the dealloying potential.

4.1.2.5 Technique option

As introduced above the time consumption of the XRD technique is obviously unfavorable. Even though, the low dependency on the condition of the sample of XRD measurement is a big advantage. A constant lattice parameter change is measurable of the samples dealloyed at high potential – in other words there are many cracks in the ligaments – with which it is difficult to measure the macroscopic dimension change by dilatometry.

4.1.3 Conclusion

In this section, in-situ dilatometry and in-situ wide-angle x-ray diffraction measurements are presented both in 1 M $HClO_4$ and 0.7 M NaF aqueous electrolytes, which shows a big difference between two strain amplitudes, and the ratio of macroscopic sample dimension change to lattice strain emerges as ~ 2 in both solutions. The apparent discrepancy points towards a distinct difference between the action of the surface stress at the solid surface as opposed to the Laplace pressure of the fluid in the pore space, which also validates the theory given in Ref. [19]. The finding is important since sorption strain and capillary condensation in porous solids are typically discussed in relation to the pressure in the fluid alone [13,20-22], which is inappropriate. The appropriate way is to take into account the surface stress effect, which is the main driving force inducing deformation of porous material, rather than the Laplace pressure.

4.2 Nanoporous carbon aerogel actuators

By using nanoporous metals, one can achieve large strain amplitude and mechanical energy density in a stiff actuator material [17]. The underlying mechanism is the changes in the surface stress of the metal when in contact with an electrolyte and subject to potential variation [95]. A similar concept may be applied to carbon aerogel [96]. Carbon aerogel (CA) is a light-weight, low cost porous material with extremely large surface area that can be loaded in compression. It is therefore of interest to explore its possible application as an actuator. Besides its use in actuation, the measurement of a fundamental parameter of electrode surfaces, namely the potential of zero charge (*pzc*) is also important. It has been proposed to use the maximum of surface tension – which is embodied in the Lippmann equation [34] – as an alternative indicator of the *pzc* by measuring the dimensional changes of the porous carbon electrode as a function of the applied potential [35,36]. In the case of liquid electrodes (for instance, mercury), the *pzc* indeed coincides with the maximum of the surface tension – from which it can be measured. However, for solid metals, it has been theoretically demonstrated that the pzc and the potential of maximum surface stress do not have to be identical. This controversy requires reinvestigating the electrochemical properties of CAs.

In this section, the mechanical and electrochemical properties of CA will be characterized. The *pzc* and their reversible dimensional changes are measured by impedance spectroscopy and by in-situ dilatometry measurements, respectively. An electrically tunable CA actuator will be presented.

4.2.1 Experimental results

4.2.1.1 Impedance Spectrum

As introduced in section 2.1.6, impedance spectroscopy (Nyquist plot of the negative imaginary part of the impedance, $-\mathrm{Im}\, Z$, versus the real part, $\mathrm{Re}\, Z$) is a very useful technique for the measurement of capacitance giving the frequency dependence $C = C(\omega)$ [97]. Here, impedance spectroscopy is used to identify suitable frequency ranges for exploring the capacitance minimum. The Nyquist plots are similar to those of an ideally polarizable electrode – an ohmic solution resistance and a double layer capacitance in series – where the Nyquist plot consists of a vertical line and the intercept with the real axis provides an estimate of the electrolyte resistance [59] (see section 2.1.6 for details). However, this is only true for the liquid mercury electrode. The impedance of most solid electrodes deviates from the purely capacitive behavior. The non-ideality or frequency dispersion has been described widely by the constant phase element (CPE) which is an empirical distributed element [98], and also observed in this work.

Figure 4.7 presents the Nyquist plots of the impedance in the ranges of ac frequency from 3 mHz to 200 Hz and of potential from −0.4 to 0.4 V at each fixed E in 0.05 M (Figure 4.7 (a)) and 0.7 M (Figure 4.7 (b)) aqueous NaF solution. The results demonstrate that both the real and imaginary parts of the impedance Z depend noticeably on E. The ideal behavior is at lower frequencies the negative imaginary part of the impedance, −Im Z, is a vertical line – which means the resistance of the electrolyte, Re Z, is constant, and the whole system is under the pure capacitive charging process. Then, the total impedance change of the system is only relevant to the capacitance change. From Figure 4.7, one can see that the most optimal behaviors are at potentials E=0.083 V and E=0.093 V in 0.05 M and 0.7 M NaF solution, respectively. Therefore, these two potentials are chosen and frequencies between 3 mHz and 200 Hz are used in the following measurements.

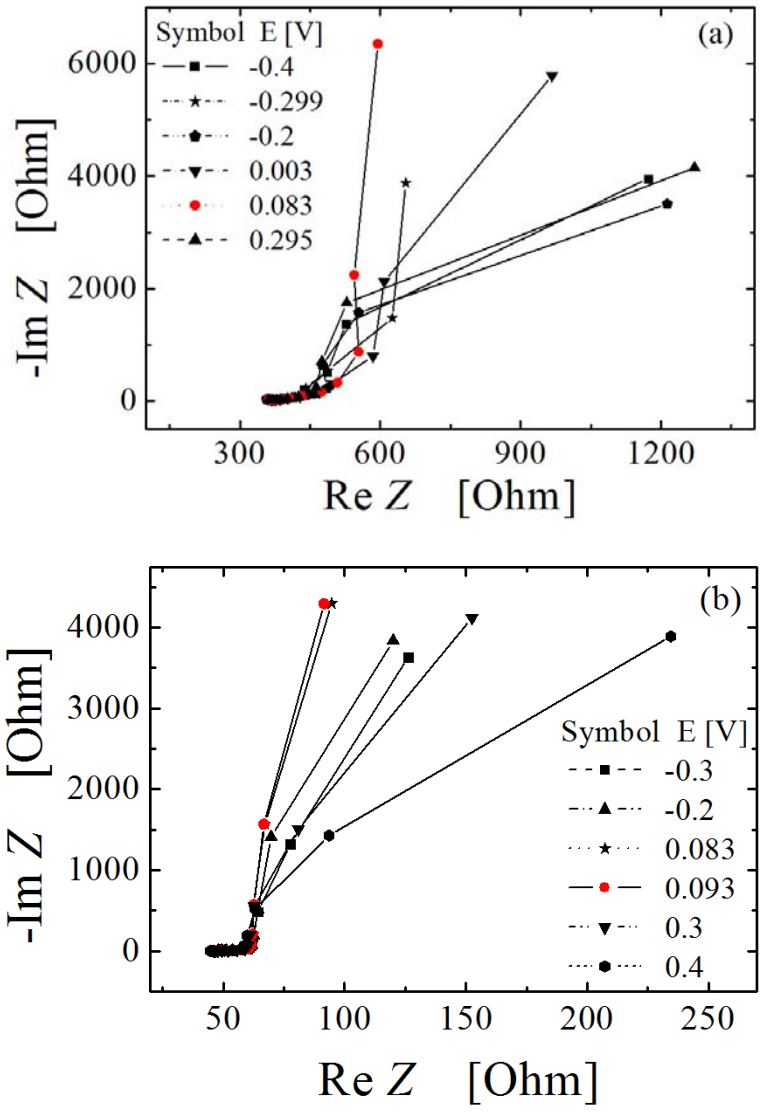

Figure 4.7 Impedance spectra (Nyquist plots of the negative imaginary part of the impedance, -Im Z, versus the real part, Re Z) obtained from CA electrodes at different potentials in (a) 0.05 M and (b) 0.7 M NaF solution. Note that both of the Re Z and -Im Z depend noticeably on E.

Figure 4.8 shows Nyquist plots obtained in 0.05 and 0.7 M NaF solutions, respectively. The data sets suggest characteristic frequencies (60 and 170 mHz, respectively) above which the imaginary part of Z becomes nearly independent of the frequency. These values were taken as the upper frequency limit for the differential capacitance measurements described below.

The frequency dispersion observed in our data is commonly found in electrochemical impedance spectroscopy, and reflects the time constant distribution of adsorption processes. The impedance spectroscopy which gets broader with increasing surface roughness. Nevertheless, the data demonstrate that the CA/NaF electrolyte interface is almost ideally polarizable.

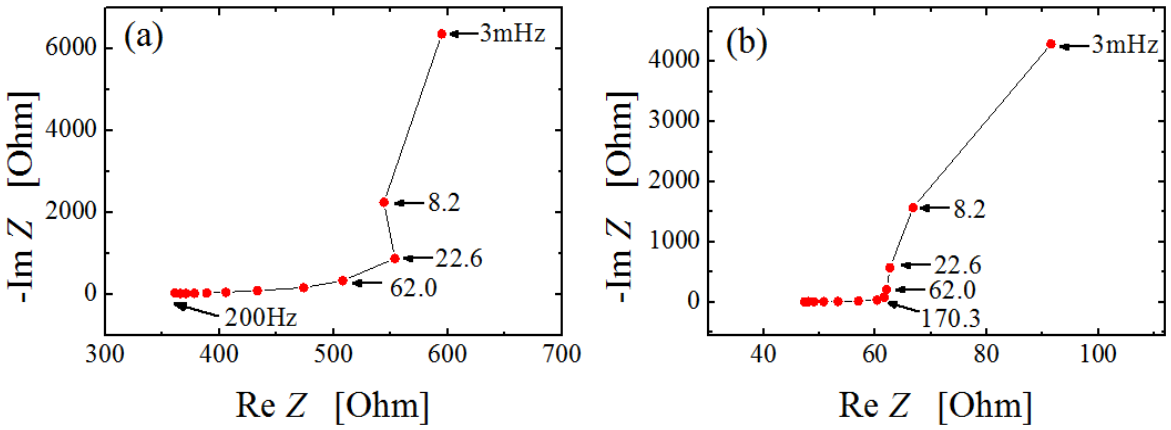

Figure 4.8 Impedance spectra of CA electrodes at (a) 0.083 V in 0.05 M NaF, and (b) at 0.093 V in 0.7 M NaF. If not otherwise noted, frequency values in labels are given in units of mHz.

4.2.1.2 Potential of zero charge

Figure 4.9 shows differential capacitance curves measured in (a) 0.05 M and (b) 0.7 M NaF solutions at different frequencies of 3 mHZ (black), 8.23 mHZ (red), 22.6 mHZ (green), 62.0 mHz (blue) and 170.3 mHz (orange). The bias potential varied in a range of ~0.4 V, centered near 0.1 V. Despite the small difference between the capacitance values measured at different frequency, the position of the minimum on the curves (*pzc*) is the same for all cases, as presented in Ref. [99]. Also shown in the figure are exemplary polynomial fits, which were used to extract the potential of capacitance minimum. These values are 89±5 mV and 92±5 mV, respectively. The values agree excellently with the one, 90 mV, measured for carbon aerogel in 0.5 M NaF by probe beam deflection and AC impedance techniques [100]. The potential at the minimum, E_{min} do not depend on the electrolyte concentration, thus indicating the absence of specific adsorption for this anion at E_{min} [101].

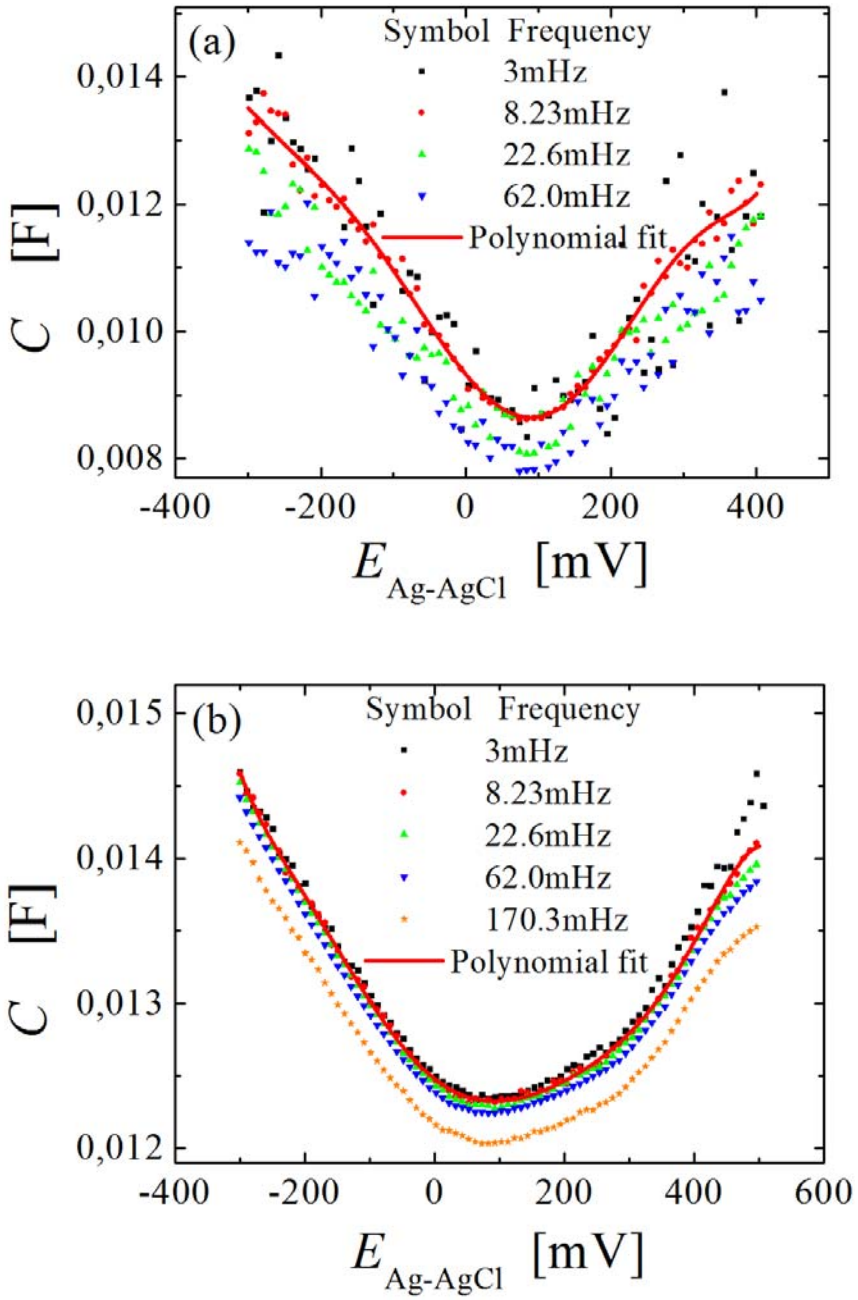

Figure 4.9 Differential capacity, *C*, of a CA electrode versus the potential, *E*. Electrolytes were (a) 0.05 M and (b) 0.7 M NaF solution. Frequencies for the different graphs are indicated in the legend. Solid lines refer to the third degree polynomial fits used for locating the minimum in *C*.

It has been reported that surface electrochemical properties of CAs are similar to those of massive (i.e., nominally pore-free) glassy carbon [102]. Therefore, the capacitance of bulk glassy carbon is measured in 0.05 M NaF at the frequency of 100 mHz, 578 mHz and 6 Hz for comparison. As can be seen in Figure 4.10 , the potential of capacitance minimum is obtained as 70±5 mV, in reasonable agreement with the results presented in this work for CAs.

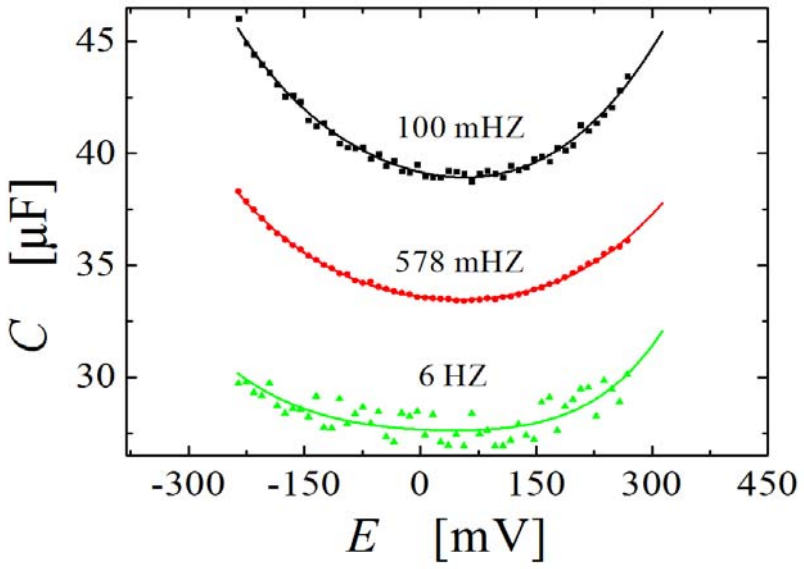

Figure 4.10 Differential capacity, *C*, of a glassy carbon electrode versus the applied potential, *E* at different frequencies. The electrolyte is a 0.05 M NaF solution. Solid lines refer to polynomial fits used for locating the minimum in *C*.

4.2.1.3 Charge-induced reversible strain in NaF solution

Figure 4.11 shows results of in-situ dilatometry during cyclic scans of the potential, *E*, with 0.05 M NaF. A potential range of ±0.2 V centered near the capacitance minimum is used at a scan rate of 0.8 mV/s. All graphs show the superposition of seven successive scans. The cyclic voltammogram (CV) of current *I* versus potential *E* in Figure 4.11 (a) is featureless, consistent with dominantly double-layer charging. In Figure 4.11 (b) the graph of charge, *Q*, versus *E* is closed, indicating that the charge is conserved. Figure 4.11 (c) shows the strain, $\Delta l/l$, as a function of *E*. The behavior is essentially linear, though with a noticeable hysteresis. Figure 4.11 (d) presents the strain-charge correlation, which is also nearly linear. The hysteresis is significantly smaller than that of the strain-potential plot shown in Figure 4.11 (c). The data thus support the notion that the strain is primarily a function of the charge. Figure 4.12 shows analogous data for the more concentrated electrolyte, 0.7 M NaF. The findings agree closely with those represented in Figure 4.11 , except for the somewhat larger strain amplitude.

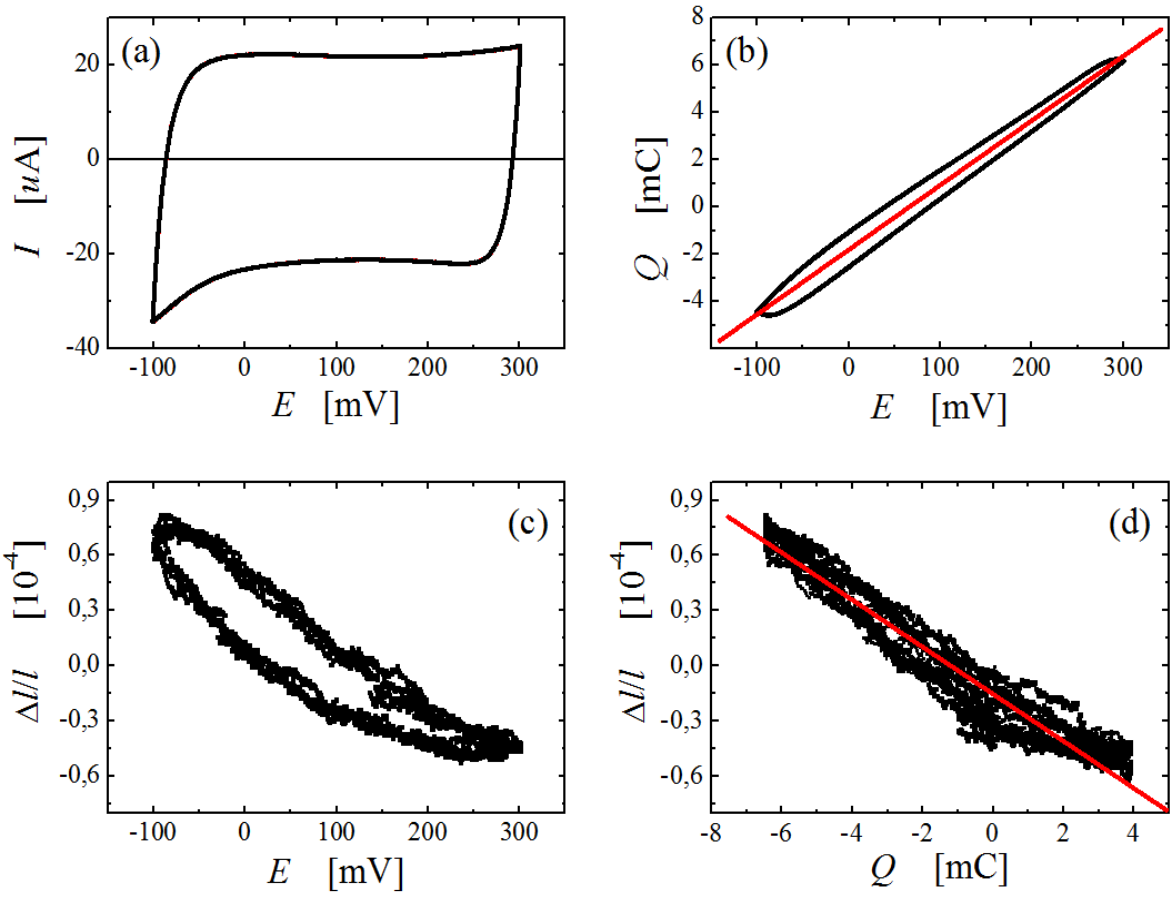

Figure 4.11 Results of in-situ dilatometry during cyclic scans of the potential, E, in 0.05 M NaF solution and at a scan rate of 0.8 mV/s. The potential interval is centered near the potential of capacitance minimum. (a), current I versus E. (b), total charge Q versus E. (c), strain $\Delta l/l$ versus E. (d), $\Delta l/l$ versus Q .

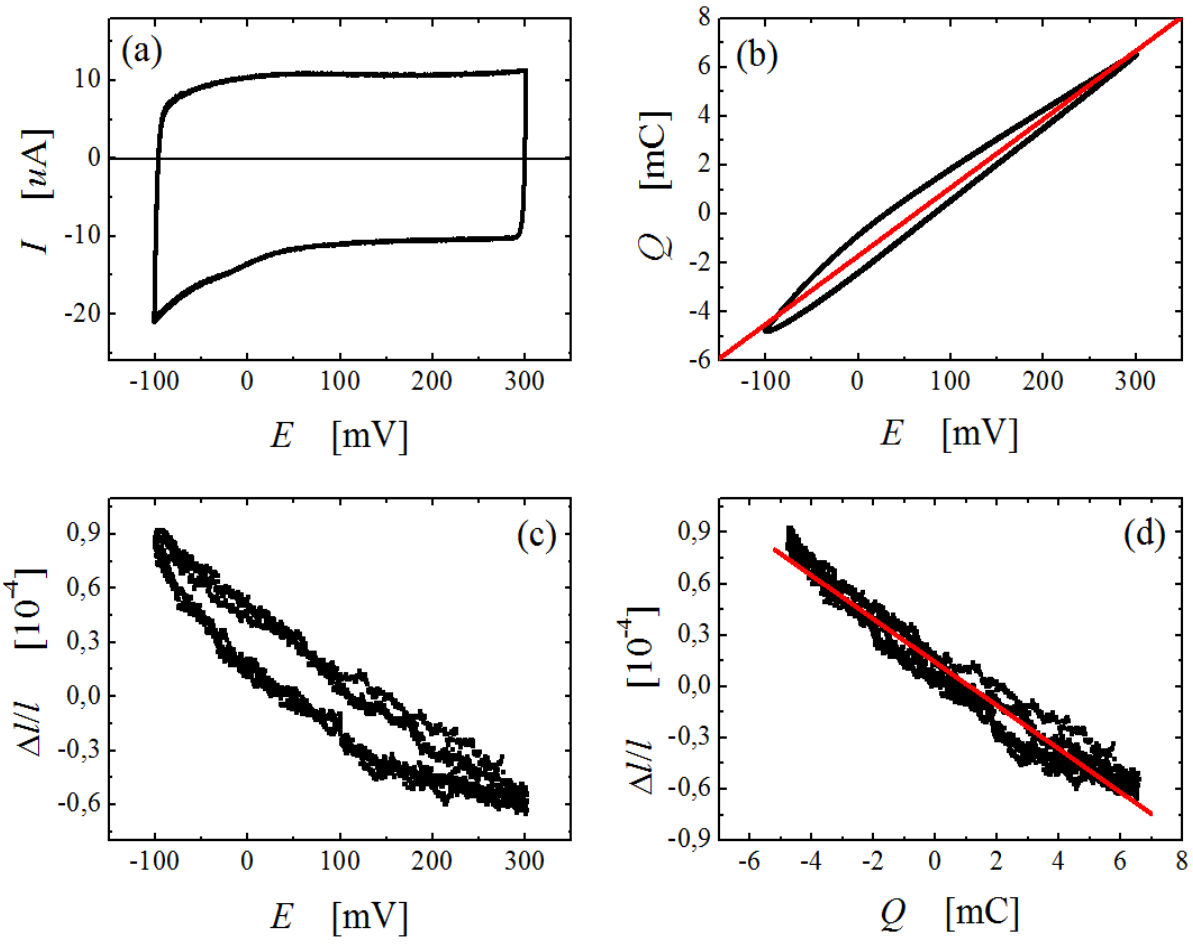

Figure 4.12 Results of in-situ dilatometry during cyclic scans of the potential as in Figure 4.11, but using the more concentrated 0.7 M NaF solution as electrolyte and a scan rate of 0.4 mV/s.

Figure 4.13 presents the continuous cyclic scans for a fresh sample in 0.7 M NaF solution, but using a larger potential range from −0.7 V to 0.9 V at a scan rate of 1 mV/s. From the red curve, one can see that the length change Δl is slowly increasing versus time t. After one day scanning, the amplitude of Δl is nearly constant. This phenomenon corresponds to a previous work discussing about the wetting behavior that 'fresh' samples upon their first contact with electrolyte tend to float, indicating that a major pore fraction is not immediately wetted. In agreement with that observation, the capacity as well as the strain amplitude in in-situ dilatometry are initially small and increase during the first cycles. After repeated cycling both values stabilize, and samples no longer float. This was taken as evidence that the electrolyte tends to wet the pores spontaneously, but with a slow kinetics [96]. Finally, the strain amplitude reached 1%, considerably larger than that in the scans with smaller potential window as described previously.

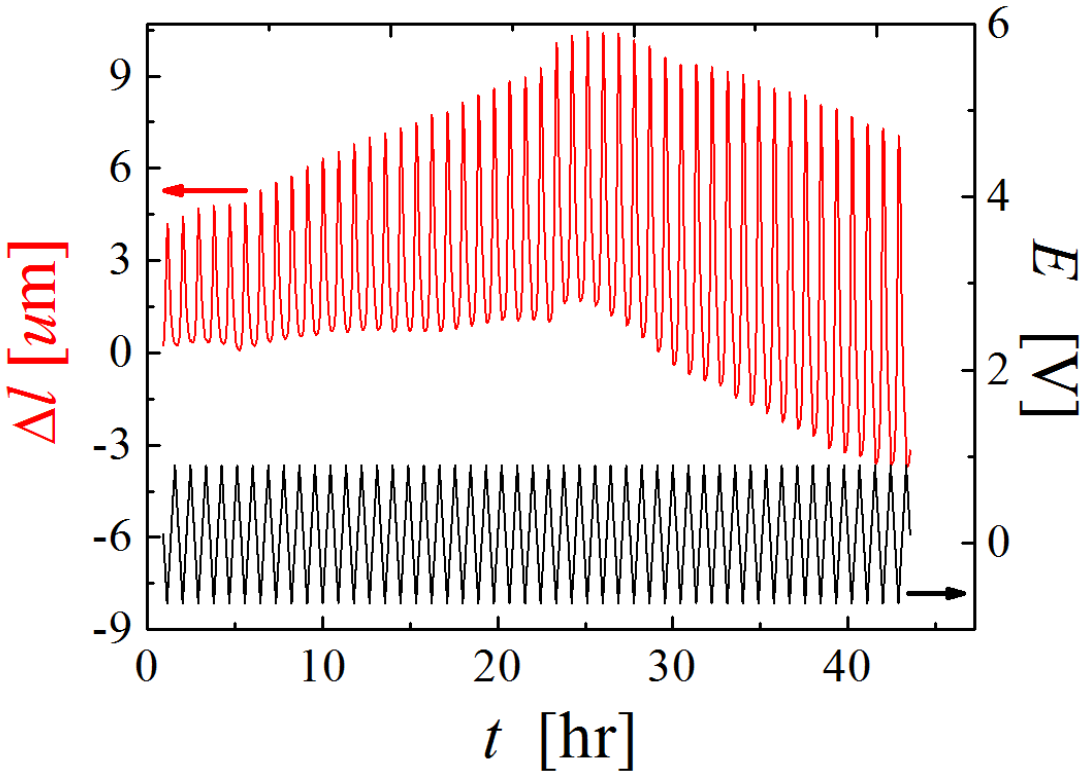

Figure 4.13 In-situ dilatometry measured length change Δl of the CAs in response to the potential E variation in the time (t-) domain, with the potential range from −0.7 to 0.9 V in 0.7 M NaF solution and a scan rate of 1 mV/s.

Figure 4.14 (a) shows the strain $\Delta l/l$ versus time t while the potential is cycled between −1.0 V and +1.0 V in 0.7 M NaF. The length changes periodically and with a decreasing slope. This irreversible change might be related to some plastic deformation of carbon aerogel and/or due to the electrochemical activation process (e.g., removing some contaminations at the surface of the sample) during the electrochemical scanning. Remarkably, the strain amplitude emerges as 2.2%. This is considerably larger than what has been reported with nanoporous metals so far [5,17], and also much larger than the strain amplitude of the typical actuator – piezoelectric actuation materials – which is restricted to 0.1-0.2% [103].

For actuation application, the reaction rate is an important parameter. The halftimes of the jumps in current and strain are 145 s and 165 s. Because of the limited sampling rate (10 s^{-1}) of the dilatometer, the time constant obtained from the charging curves is considered more accurate. Figure 4.14 (b) shows the frequency dependence of the amplitude (in the form of percentage of the maximum strain amplitude) during potential jumps. The strain amplitude at a frequency of 7 mHz is almost identical to that during slower switching, which is consistent with the response time given above. The characteristic frequencies are also measured with 0.05 M NaF, which emerge as 2 mHz, 15 mHz with 1 M H_2SO_4 aqueous solution and with 1-butyl-3-methylimidazolium tetrafluoroborate (C8H15BF4N2). These characteristic frequency values support that the reaction is faster within the solutions of higher electric conductivity.

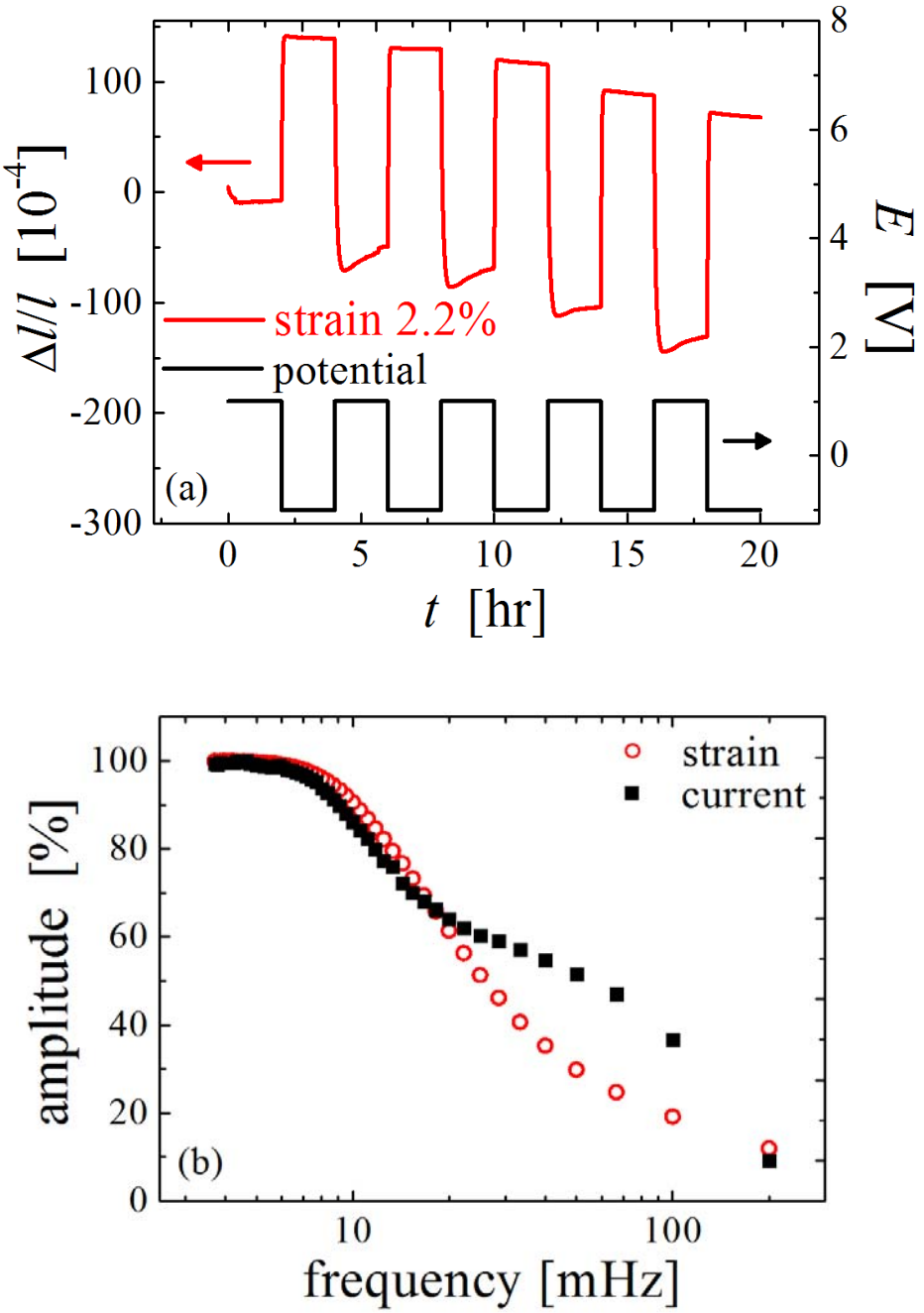

Figure 4.14 In-situ dilatometry measurement of the CAs with the potential range from −1.0 to 1.0 V in 0.7 M NaF solution. (a), strain $\Delta l/l$ in response to the potential E variation in the time (t-) domain. (b), Frequency dependence of the amplitude (% means that the percentage of the maximum strain amplitude) during potential jumps (rectangular wave). Large squares (black): Amplitude of the charging curve. Small circles (red): Amplitude of the length change as measured in the dilatometer.

Figure 4.15 presents the strain amplitudes of carbon aerogel samples with different BET surface areas (namely 440, 1490, 2800 and 3030 m^2/g) in the potential range from −0.7 V to 0.9 V (dark

triangle) and −1.0 to 1.0 V (red square), respectively. It shows a linear dependence of strain on the BET surface area, the slopes are 7.1×10^{-4} and 1.5×10^{-4} g/m^2, respectively.

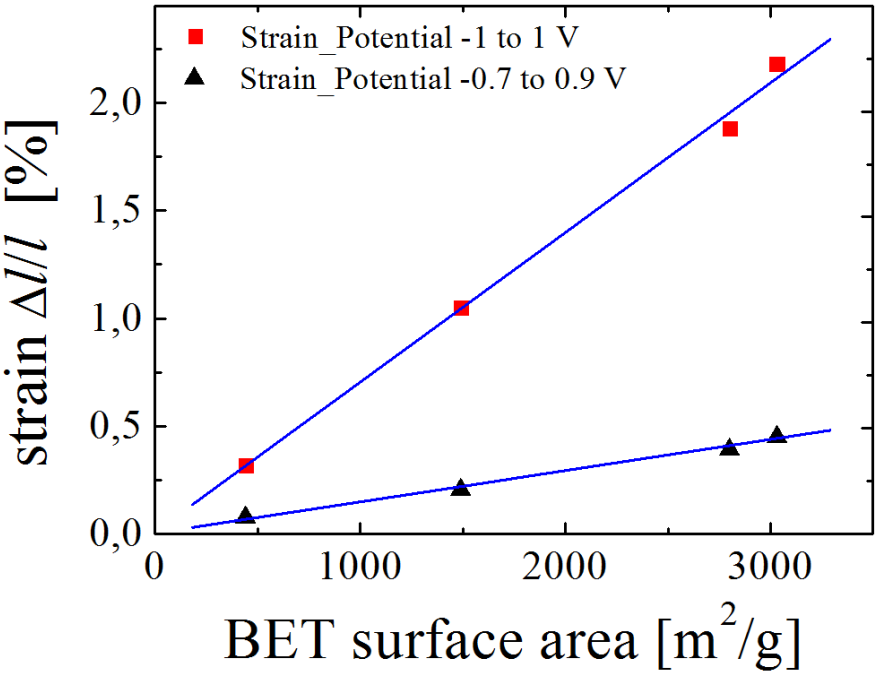

Figure 4.15 In-situ scans with different samples in 0.7 M NaF at the scan rate of 1 mV/s and in a potential range from -0.7 V to 0.9 V (dark triangle) and -1.0 to 1.0 V (red square), respectively.

4.2.1.4 Mass-specific capacity

The net capacity, C, of CA material is determined by recording cyclic voltammograms within the double-layer region at different scan rates v (Figure 4.16 (a)) and using the relationship

$$|I| = C\,|\mathrm{d}E/\mathrm{d}t| = Cv \qquad 4.2$$

where $|I|$ refers to the mean magnitude of the currents measured during the positive and negative scans near the potential of capacitance minimum. Note the linear correlation between $|I|$ and v (Figure 4.16 (b)). Using this method, C values of 28 and 33 mF are obtained for the 0.05 and 0.7 M solutions, respectively. As a counter check, C from the slopes of the Q versus E plots shown in Figure 4.11 (b) and Figure 4.12 (b) are also computed. This method yields C = 27 and 28 mF for the 0.05 and 0.7 M solutions, respectively. Thus, it can be concluded that the capacity is in the order of 30 mF and that it varies by 15% or less between the two solutions. As the basis for further discussion it is useful to refer the capacity to the sample mass, which gives c_m ~77 F/g for the mass-specific capacitance.

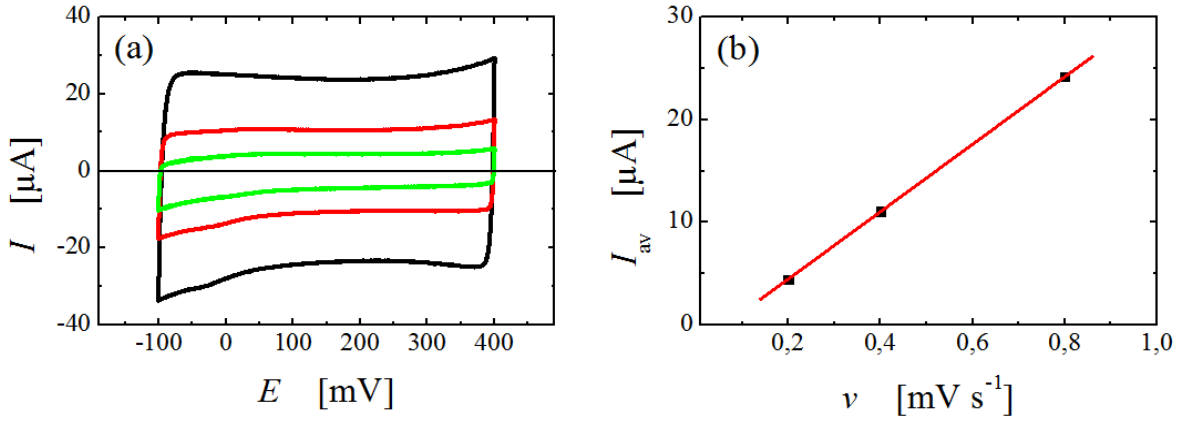

Figure 4.16 cyclic voltammograms of current, I, versus potential, E, in 0.7 M NaF near the potential of capacitance minimum. Scan rates are 0.8 mV/s (black), 0.4 mV/s (red), 0.2 mV/s (green). (b) Average, I_{av}, of current in positive and negative going scans of the voltammograms in part a), plotted versus the scan rate, ν.

4.2.1.5 Work density

As an important parameter for actuation, it needs the value of work density, w, of an actuator. Assuming the actuator is a linear elastic solid, the mass-specific strain energy density, w_M, is given as $w_M = ½ Y_{eff} \varepsilon^2_{max}/\rho$, where Y_{eff} is the effective macroscopic Young's modulus, ε_{max} is the maximum strain amplitude and ρ is mass density [17]. The effective macroscopic Young's modulus Y_{eff} was measured by compression test, which was carried out on a testing machine [104] for miniature samples under controlled cross-head speed. The displacement of the cross-head was recorded, and empty runs produced a baseline used for correction the effects caused by the machine compliance. The engineering stress was determined as $\sigma = F/S_0$, where F is the force and S_0 is the initial area of sample cross section. And the engineering strain $\varepsilon = \delta l/l_0 \times 100\%$, where δl is the displacement of the sample upon compression and l_0 is the sample initial length. Y_{eff} is measured as 280 MPa for the CA sample, and the stress-strain curve is shown in Figure 4.17 . ε_{max} and ρ are 2.2% and 0.14 g/cm^3, respectively. Thus it can be obtained that the energy density is 485 J/kg.

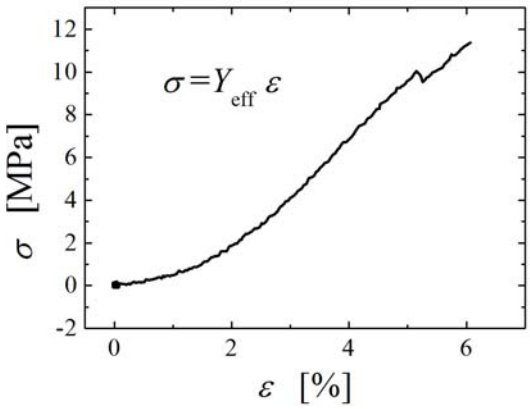

Figure 4.17 Stress-strain curve of CA sample measured by compression test.

4.2.1.6 Charge-induced reversible strain in different solutions

Figure 4.18 shows the charge-induced reversible length change of carbon aerogel in different aqueous electrolytes, which are 0.7 M NaF, 1 M KOH, 1 M KCl and 1 M H_2SO_4, respectively. The length changes nearly linearly versus potential in NaF and KOH solution as shown in Figure 4.18 (a), (b) and parabolically in KCl and H_2SO_4 as shown in Figure 4.18 (c), (d).

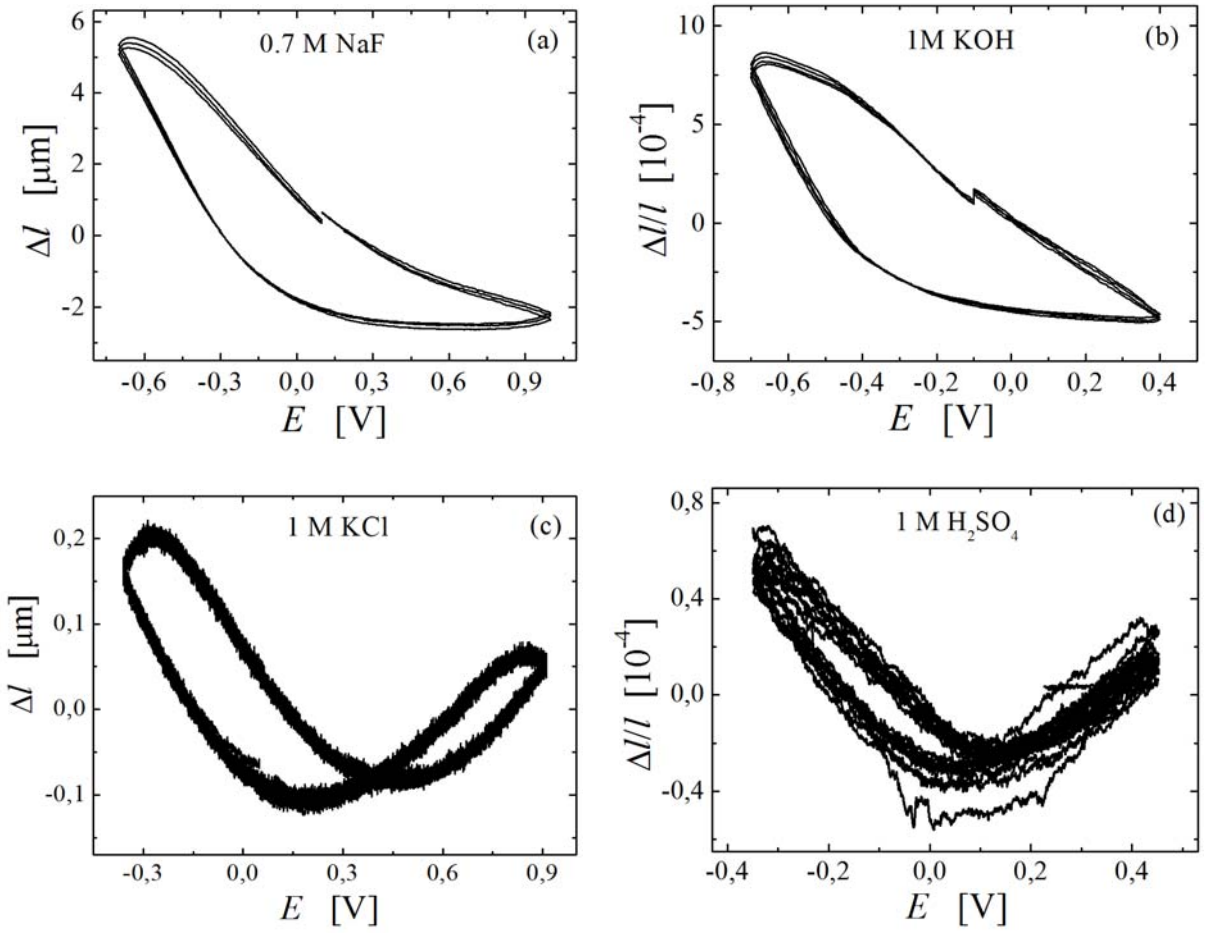

Figure 4.18 Dimentional changes of CAs measured by in-situ cyclic scans in different aqueous solutions. (a) 0.7 M NaF; (b) 1 M KOH; (c) 1 M KCl; (d) 1 M H_2SO_4.

4.2.2 Discussion

4.2.2.1 Microstructure

The BET mass-specific surface area of CA samples, α_m = 2800 m^2/g, is extremely large, it is meaningful to estimate the fraction, Φ, of surface atoms. The number of surface atoms per gram, n_s, can be estimated by assuming that the surface of our CA has graphitic character. Multiplying

α_m with the areal density of C atoms in the graphite basal plane, $3.8 \times 10^{15}\,cm^{-2}$, yields $n_s \sim 1.1 \times 10^{23}\,g^{-1}$. On the other hand, the total number, n, of carbon atoms per mass is only $5 \times 10^{22}\,g^{-1}$. From this argument, the fraction of surface atoms, $\Phi = n_s/n$, emerges as ~ 2. This result looks like unphysical at first sight, since the atom fraction can not exceed unity. However, in our reasoning a free-standing basal plane of graphite would have $\Phi = 2$, since each atom belongs here to two surfaces. The obvious example for such a structure is graphene, which is a perfectly stable form of carbon. Apparently, the CA structure is very open, so that most carbon atoms are adjacent to more than one surface.

It is also instructive to estimate a volume-specific surface area, α_S, of the solid phase. Using the α_m value along with the mass density of graphite – again in the spirit of a rough estimate – it is obtained $\alpha_S \sim 5.9/nm$. As a cross-check for the above considerations on the geometry, let us assume that the solid skeleton structure of the aerogel was formed by elongated ligaments with roughly circular cross-section of diameter D, so that $\alpha_S = 4/D$. The required value of D would then be 0.68 nm, again comparable to the carbon-carbon interatomic spacing.

Thus, it can be concluded that CAs samples used in this work are carbon nanostructures with an extremely large specific surface area, in which essentially every carbon atom is a surface atom. Given the relatively high solid volume fraction of the materials, 0.07, this result requires the existence of extremely small pores.

4.2.2.2 Capacitance

Combining the experimental value for the mass-specific capacitance, c_m (see subsection 4.2.1.4), with that of the BET mass-specific surface area, α_m, the area-specific values of the capacitances, c_a, can be obtained at around 2.8 $\mu F/cm^2$. The double layer capacitance measured by impedance spectroscopy and linear sweep voltammetry on the basal plane of graphite has been reported as 3 $\mu F/cm^2$ and 2.7 $\mu F/cm^2$ for the 0.9 M and 0.01 M NaF aqueous solution, respectively [105,106]. However, the same reference finds that the value for the edge plane is as high as 50 – 70 $\mu F/cm^2$. The findings for the capacitance of CAs in this work agree well with the reported values of the graphite basal plane, supporting the discussion in terms of a graphite-like structure.

For the area-specific capacitance of the glassy carbon reference sample the measured value is 25 $\mu F/cm^2$ in 0.7 M NaF. This is significantly larger than the data for both graphite and aerogel. The difference can be attributed to roughness of the glassy carbon surface, which prevents a valid determination of the surface area. In fact, reported values of the double layer capacitance for other carbon materials in liquid electrolytes vary significantly, depending on the surface orientation and roughness, electrolyte pH, and functional groups on the surface [107].

As compared to metals (which exhibit capacitance values of several tens of $\mu F/cm^2$), the capacitance of our CA samples appears anomalously small. Two different explanations have been brought forward: First, if the pore size is comparable to or smaller than the (Debye-Hückel-) screening length in the electrolyte, the restricted geometry will impair the screening and, consequently, reduce the capacitance [108]. Secondly, the capacitance may be controlled by the solid side, where the small density of states at the Fermi level in graphite-like carbon implies small capacitance [109]. Of the two explanations, the data shown in this work seem to support the second, as the capacitance of the CA agrees well with reported data for bulk graphite samples. This is also further supported by the finding that the capacity for CAs is nearly independent of the

electrolyte concentration: The data for *C* deduced from Figure 4.16 vary by 15% or less as the electrolyte concentration is increased fourteen fold (from 0.05 to 0.7 M). This observation is not readily reconciled with theories for the capacitance of the diffuse layer in the electrolyte, even if one considers the confined geometry. The observation is, however, consistent with the screening limitations in the solid phase as discussed above.

4.2.2.3 Relation of length change to *pzc*

As mentioned in the introduction, it has been suggested that the *pzc* of nanoporous carbon (and generally the *pzc* of solids with a sufficiently large specific surface area) can be determined from the electrocapillary strain maximum [35,36]. Experiments shown in this work provide a test for this suggestion, since they combine strain measurements by dilatometry with impedance spectroscopy as an independent means to obtain the *pzc* from the capacitance minimum. The results here reveal a linear strain-potential correlation at the potential of minimum capacitance. Since the latter is fundamentally linked to the *pzc*, and since strain has been shown to be unrelated to the *pzc* on fundamental grounds [38], the results in this work are taken as conclusive evidence that the *pzc* and the potential of the strain minimum (the maximum of surface stress) do not coincide in porous carbon under the present conditions. Thus, it can be concluded that the *pzc* should not be determined from the observation of an electrocapillary strain maximum as suggested in Refs. [35,36].

4.2.2.4 Linear or parabolic?

In Figure 4.18, the strain versus potential curve has either linear or parabolic shape in different electrolytes even in a similar potential window. The observation of expansion during negative charging is in agreement with graphite intercalation data, where it was found that the C-C in-plane bond length increases if electrons are added into the graphite π bands and vice versa [110]. A possible explanation for the bending when the scan goes to more anodic potential in Figure 4.18 (c) and (d), is the charge transfer from the adsorbed Cl^- or SO_4^{2-} anions to the carbon substrate, which leads to the increase of negative charge, thus the electrode expansion. It is well known that Cl^- or SO_4^{2-} ions are strongly specifically adsorbed anions, while F^- and OH^- are not [111].

Within a rigid-band scenario, one would anticipate that the expected strain-potential (charge) behavior of graphite is very sensitive to the microscopic nature of the density of states (DOS): if one were to assume that the Fermi energy, E_F, of charge-neutral graphite is at the minimum in the DOS graph, then one would expect a minimum of the in-plane C-C bond length at zero charge. Negative charging injects electrons into the antibonding conduction band states, whereas positive charging removes electrons from the bonding valence band states. Both processes would lead to expansion. At first sight, this argument appears to support equivalence between the electrocapillary minimum and the potential of zero charge. However, the argument rests on an assumption of a microscopic nature of the DOS, which may or may not apply to the solid graphite nanostructure under investigation. By contrast, the electrocapillary minimum at fluid surfaces that emerges from the Lippmann equation is a thermodynamic result that applies universally to all fluid surfaces, independent of the microscopic details of the system. Coming back to carbon

nanostructures, it has been pointed out that the graphite DOS actually has the Fermi level displaced relative to the DOS minimum so that the minimum bond length is expected at slightly positive charge [112]. Qualitatively, our findings point to a similar situation.

4.2.2.5 Surface stress-charge coefficient

Length changes of carbon structures–more specifically, nanotubes–upon introducing space-charge layers have already been reported by others and turn out to be applicable for actuators [26,113]. The underlying mechanism is the interatomic bond forces changing of the atoms at surface due to charge injection. In order to compensate this surface stress, f, in response to surface charging, the bulk stress changes which leads to the measured strain. This local response is quantified by the surface stress charge coefficient, $\varsigma = (\mathrm{d}f/\mathrm{d}q)_e$, where q is the superficial charge density and e denotes a tangential strain. For a given value of the materials parameter ς, the balance equations of continuum mechanics afford predictions on the interrelation between net strain amplitude and the geometry and scale of the microstructure (see section 2.2.2). While such relations are valuable in the context of charge induced strain of porous solids, the underlying concept cannot be transferred to the present material: Since it was found that every atom in CA sample is a surface atom, the distinction between bulk and surface behavior that underlies the definition of surface tension and surface stress becomes inappropriate. Nonetheless, the phenomenology of the present experiments is closely related to that of the more conventional nanoporous solids, and we may use the same data analysis to obtain an apparent surface stress-charge coefficient that then can be compared to that of the previous data. To this end we use [114]

$$\varsigma_{\text{apparent}} = -\frac{9}{2}\frac{K\,m}{\rho}\frac{\delta \ln l}{\delta Q}$$

to relate ς to the experimental data. Here, m and K denote the sample mass and the bulk modulus (40 GPa [115]) of graphite, respectively. We have determined $\delta \ln l/\delta Q$ from straight-line fits to the in situ dilatometry data and obtained the apparent surface stress-charge coefficients, $\varsigma = 0.42 \pm 0.01$ V and 0.41 ± 0.01 V in 0.05 M and 0.7 M NaF solution, respectively. Reported ς values for metals are between −0.4 to −2.0 V [114]. However, metal surface covered with an oxide monolayer oxide can also exhibit positive ς values [14,90].

4.2.2.6 Potential of zero free charge or potential of zero total charge?

In the above context, it is important to discuss the distinction between two variants of the *pzc* [62,116]:

1. The potential of zero free charge (*pzfc*), defined as the potential at which the truly free, electronic excess charge density on the electrode vanishes.

2. The potential of zero total charge (*pztc*), defined as the potential at which the sum of the free, electronic excess charge density and the charge density transferred in adsorption processes equals zero.

The capacitance minimum occurs at the *pztc*. This potential coincides with the *pzfc* only in the absence of specific adsorption. In this work, the NaF aqueous electrolyte has been used for the

pzc measurement, because F^- anions show very low specific adsorption to the carbon aerogel surface. However, one can not exclude that there is a small amount of specifically adsorbed fluorine ions. In addition, the material may also contain some H- or OH-terminated step edges, though their number is expected to be small due to the high temperature synthesis of the material. The close agreement of the potential of capacitance minimum measured here for CAs with the *pzc* values reported for nominally clean graphite surfaces suggests that the adsorbates coverage in our samples is small, and that the potential of capacitance minimum are indeed representative for the *pzfc*.

4.2.2.7 Advantages of carbon aerogel actuators

The results in section 4.2.1.3 verified the actuation effect of carbon aerogel with a huge dimensional change of 2.2%, which is consistent with the 2% maximum variation in basal plane dimension that is observed for graphite intercalation compounds [26]. And the volume strain, which is obtained through multiplying the length change of the bulk sample by factor of 3, emerges as 6.6%. In contrast, the typical carbon nanotube arrays, which have been suggested for actuation application, cannot achieve such large strain in aqueous electrolyte.

It is well known that, in the electrochemical actuator systems, increasing the magnitude of the applied potential can increase the strain amplitude, which is also verified in this work. However, higher potential will induce electrolysis of water and generate bubbles on the sample surface. This would decrease the lifetime of the actuator. Therefore, the method of increasing the potential to obtain larger strain is limited. Actual strains of 0.1 - 1% have been reported based on film type single-wall carbon nanotube actuators. The multi-wall carbon nanotubes actuator shows strains up to 0.15% within a 4 V potential interval [117], where the potential is twice the potential window used in this work but resulting in a much smaller strain amplitude than our CA samples. In this work, except choosing the different potential range to get the corresponding strain, it is not only possible to keep the potential in a relatively smaller interval, but also to choose samples with different surface area to achieve a particular strain, which depends on the relations between strain and BET surface area as shown in Figure 4.15.

In order to evaluate the investigated CAs, some characteristic figures of merit for different types of actuator materials are represented in Figure 4.19. While the largest strain amplitudes are reached by dielectric elastomers [118] and by skeletal muscles [119], the highest stiffness is observed for piezoceramics [103] and np metals [17], carbon aerogels show the largest mass-specific strain energy density. Furthermore, by comparing to all alternative materials shown in the chart, carbon aerogels are distinguished by their low operating voltage, which is at same scale as np metals. Therefore, the combination of low voltage with tunable large strain amplitude and high mass-specific strain energy density and the fact that they are inexpensive than noble metals characterizes carbon aerogels as materials for effective conversion of electric energy into mechanical work.

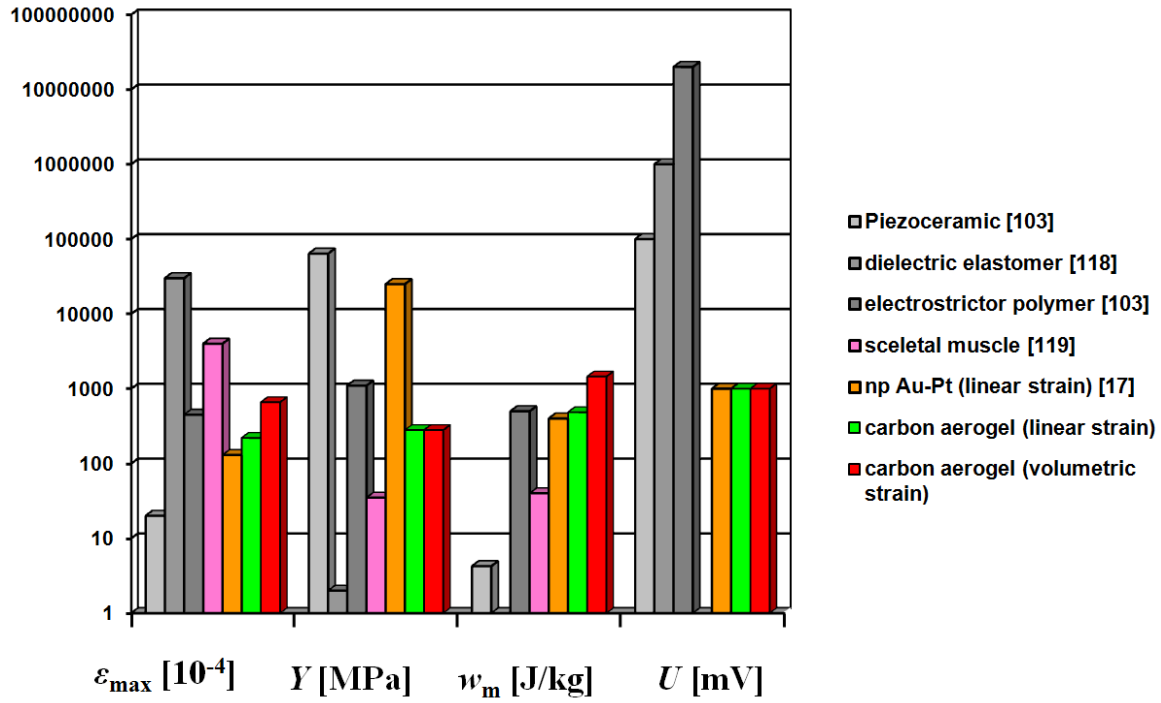

Figure 4.19 Column chart plot of characteristics of various actuator materials. ε_{max}, maximum strain; Y, effective modulus; ω_m, mass-specific strain energy density; U, operating voltage for 100 µm actuator size.

4.2.3 Conclusions

In order to determine the potential of zero charge (*pzc*) of carbon aerogel immersed in aqueous NaF solutions, impedance measurements have been presented. The pronounced and reproducible capacitance minima which were found suggested that the *pzc* can be reliably obtained from the impedance data. The experimental *pzc* values obtained in this way are around 90 mV, in reasonable agreement with the result for bulk glassy carbon. The charge-induced length changes of the same samples have been measured by in-situ dilatometry in a potential interval centered at the *pzc*. The comparison of the two data sets leads to the conclusion that for carbon aerogel the *pzc* does not coincide with the potential of minimum sample length. In other words, while there must be an (electrocapillary) maximum in the surface tension at the *pzc*, the dilatometry data do not probe that phenomenon. Instead, the potential-dependent stress and strain of carbon aerogels probe charge-dependent changes in the bonding at the interface. This phenomenon is commonly described by variation of the surface stress, but the very small structure size of the aerogel prevents a meaningful separation into bulk and surface properties that is required for that concept. The absence of a strain minimum at the *pzc* confirms that dilatometry data are poorly suited for identifying the *pzc* of solid electrodes, including carbon.

Besides being of interest in relation to the above fundamental aspect of electrochemistry, the large strain amplitude and mass-specific strain energy make carbon aerogels also candidates for use as light-weight, low-cost actuator materials. In this relation it is remarkable that scans in a

larger potential window yielded a strain amplitude of 2.2%. This compares favorably to amplitudes reported for nanoporous Pt and Au, which have larger specific weight and higher cost. Additionally, CA exhibits a large mass-specific strain energy density, which even exceeds that of piezoceramics and nanoporous metal actuators.

5 Electrochemical training and modulation of photonic metamaterial

In last chapter, a method to get novel functional behavior is introduced that immersing a metallic-based nanomaterial in an electrolyte and introducing a space-charge region by an applied potential. The charge-induced macroscopic length change can be measured by changing the potential value. In this way, an electrically tunable carbon aerogel actuator is achieved. Another instance for the concept of tunable nanomaterials is electrically tunable photonic metamaterials [120,121]. Metamaterials use arrays of lithographically structured spilt-ring resonators to achieve an unconventional optical response – in the extreme, the negative refractive index.

In the present work, the space-charge and also the adsorbate coverage at the surface of each resonator is controlled via an applied potential. A surprisingly large electrochemical modulation will be presented through an in-situ optical measurement which combines electrochemistry and transmittance measurements. And the quality of thin gold split ring resonators will be improved by electrochemical training. In order to figure out the mechanism of the electrical modulation phenomena, the influence of foreign ions, here lead and copper adsorbed on the resonators by underpotential deposition was analyzed to give a qualitative explanation. For the basic theory and experiment setup please see section 2.3 and 3.3.4, respectively.

5.1 Experimental results

5.1.1 Training of photonic metamaterial

All the photonic metamaterial samples used in this work consist of split-ring-resonators (SRR) with the edge length about 90 nm as the inset SEM image shown in Figure 5.1 (a). Only the thickness of the SRR samples will be varied in the following experiment, the other dimension will be kept as constant. For the SRR samples with thin thickness (less than 12 nm), the damping of the resonance is very large or even no resonance can be measured with extremely thin resonators. Hence, before the electrically modulation measurement, the samples need to be trained to present a good resonance. The details will be present in this section.

The representative electrochemical signatures for the metamaterial of this work in the form of cyclic voltammograms (CVs) are shown in Figure 5.1 (a). The most distinctive feature is a peak at positive potential that occurs only during the first cycle. This peak is absent if no Cr adhesion layer is used (not depicted). Thus, this peak can be linked to partial dissolution of Cr. In the sub-

sequent cycles, the most important features are the OH-adsorption peaks during positive-going scans and the corresponding desorption peaks during negative-going scans in the potential range $E > 0$. The large current values at $E < 0$ indicate Faraday reactions (see subsection 2.1.2) related to oxygen trace contaminants in the cell, which is open to air. The small current value outside these features indicates dominantly capacitive double-layer processes. Optical transmittance spectra are shown in Figure 5.1 (b). After completion of sample fabrication, the 7 nm thin gold resonators show nearly no plasmonic resonance – in air as well as in the electrolyte as the black curve shows in Figure 5.1 (b) (before cycling). This is not surprising in view of the very large gold electron scattering/damping due to the considerable surface roughness and presence of grain boundaries expected for such very thin evaporated amorphous gold films. However, after 10 electrochemical cycles with a potential window from –0.9 V to +1.3 V – which we will call the "training" phase in what follows – a much more pronounced and sharper plasmonic resonance appears as the red curve shows in Figure 5.1 (b) (after cycling). The training effect also reproducibly persists if the nanostructure is removed from the electrolyte, making it useful as a simple electrochemical post-processing step for metamaterial fabrication. This approach complements recent work in a different size and thickness regime based on thermal annealing [122].

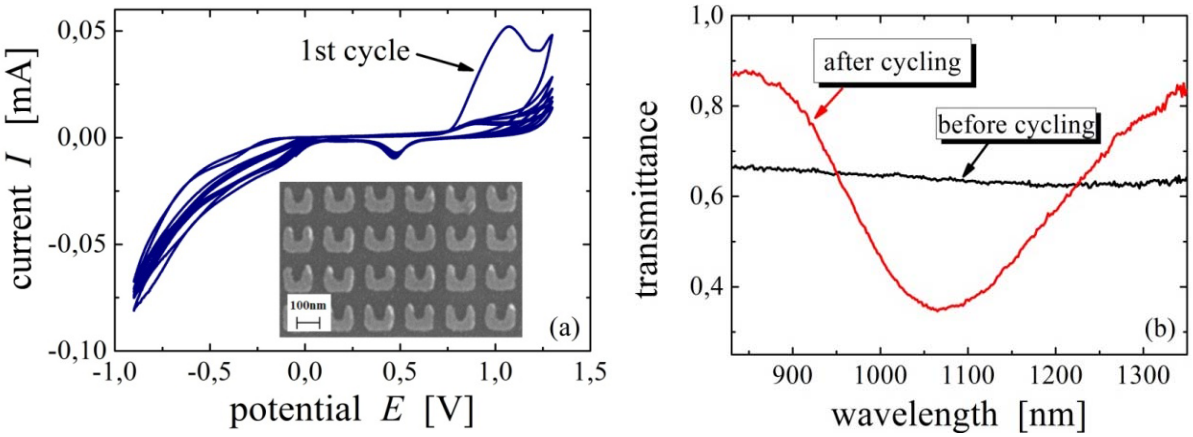

Figure 5.1 (a) Typical cyclic voltammograms of arrays of 7 nm thin gold split-ring resonators (scanning electron micrograph shown as inset) in aqueous NaF electrolyte with electrode potential window from –0.9 to +1.3 V. The first cycle is indicated, further cycles coincide within the linewidth of the curves. (b) Corresponding normal-incidence transmittance spectra for vertical incident linear polarization of light at open circuit potential before (black) and after 10 complete cycles (red). Note the very substantial sharpening of the resonance.

As shown in Ref. [39], for thicker gold resonators (20 nm in their case), the plasmonic resonances exhibit low damping even without initial electrochemical cycling. The training effects in Figure 5.1 (b) are more pronounced for thinner "resonators" near or even below the percolation threshold. The thin SRRs are used in this work, because with these samples one can get larger modulation effect since the surface-to-volume ratio is larger with thinner sample. For example, for a nominal gold-resonator's thickness of 8 nm, the disconnected islands of gold "before" cycling develop into a continuous film "after" the cycling. This phenomenon is presented by the images taken from scanning electron microscopy (SEM) before (left of Figure 5.2 (a)) and after (right of Figure 5.2 (a)) the complete electrochemical cycling. Note that the resonators after cycling appear much smoother in the SEM images. The comparison of the corresponding transmittance spectra in electrolyte at open circuit potential before and after the complete cycling is ex-

hibited in Figure 5.2 (b). The samples with different thicknesses in the range from 12 nm to 7 nm have been measured in the same way, and in each of these cases, a substantial sharpening of the plasmonic resonances is observed.

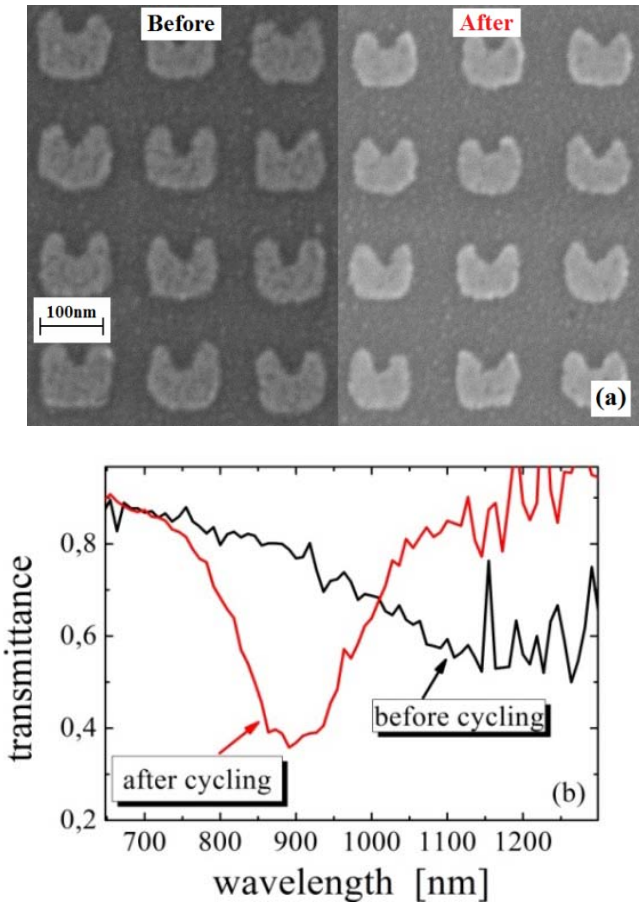

Figure 5.2 Gold split-ring resonator arrays with an average gold-resonator thickness of 8 nm before and after electrochemical cycling. (a) The left image exhibits scanning electron micrographs before cycling. The right image depicts corresponding data after cycling. (b) The corresponding measured normal-incidence transmittance spectra before (black curve) and after (red curve) cycling. Note the distinct changes after cycling.

The above mentioned training effect causes similar phenomena as with electrochemical annealing on gold single crystal electrodes [123,124], where the authors found that the oxide covered rough Au(111) layer becomes smooth after the electrochemical cycling. However, one should pay attention to the choice of training electrolyte. For instance, 0.5 M NaCl aqueous solution has been tried for training the photonic metamaterial in this work. After cycling 10 times in the potential window from –0.9 V to 1 V, the gold resonators' structure has been damaged as shown in Figure 5.3. The reason might be related to the strong specific adsorption property of Cl^- anions, because it has also been observed that the dissolution of surface gold atoms occurred during electrochemical cycling in chloride-containing solutions [123]. The specific adsorbates greatly enhanced the mobility of the surface gold atoms, since the bonding between the gold atoms to the adsorbates reduces the strength of the bonding to the neighbor gold atoms. Therefore, NaCl was avoided and

the less strongly adsorbing NaF used instead for electrochemical training and modulation in this work.

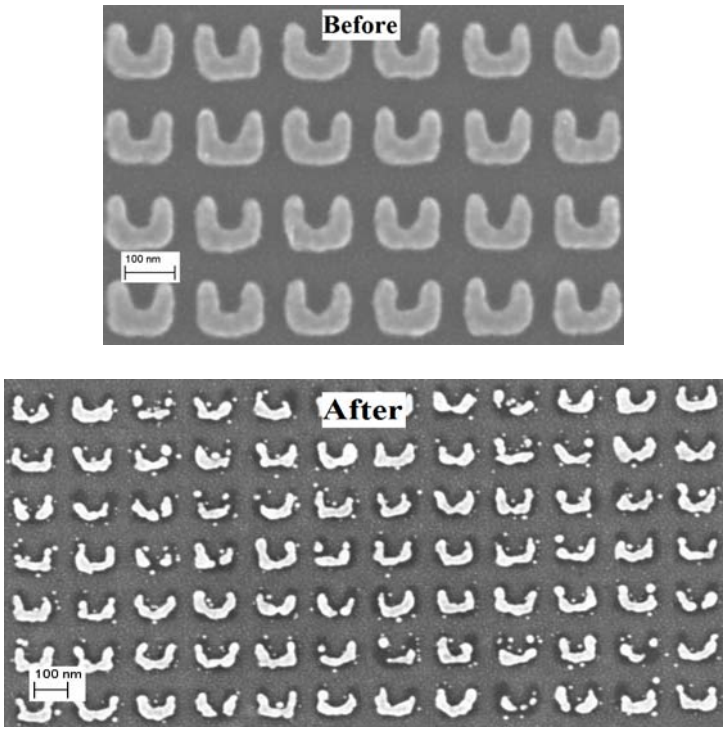

Figure 5.3 Scanning electron micrographs of gold split-ring resonator arrays with an average gold resonator thickness of 10 nm before and after 10 electrochemical cycles from –0.9 V to 1 V in 0.5 M NaCl aqueous electrolyte. Note that the resonator structure has been damaged after cycling.

5.1.2 Modulation of photonic metamaterial

Once the plasmonic resonance is established by electrochemical training, it also persists within the electrolyte, allowing for further studies. Figure 5.4 exemplifies the typical results of resonators having a thickness of 10 nm and with a horizontally polarized incident light. A reversible modulation of the plasmonic resonance position is observed. Figure 5.4 (a) shows the spectra shift to blue (smaller wavelength) when E is varied from 1.3 V to −0.9 V, and a red shift (larger wavelength) when E goes to the positive direction as shown in Figure 5.4 (b).

As has been introduced in section 2.3.3, with the horizontally polarized light (see Figure 2.9 (c)), the electric field could couple to the capacitance of the SRR and induce a circulating current in the coil leading to a magnetic-dipole moment normal to the SRR plane and opposing the external magnetic field, hence $\mu<0$. As shown in the transmission versus wavelength curve Figure 5.4 (a) and (b), those two measured pronounced minima at around 700-800 nm and 1100-1250 nm correspond to the electric and magnetic resonances, respectively [39,125]. The peaks of the electric and magnetic resonances shift by as much as 65 nm and 117 nm within one cycle, respectively. The resonance wavelength, λ_R, and transmittance, T_R, versus potential, E, of both the electric and

magnetic resonances are shown in Figure 5.4 (c) to (f), respectively. The trends can be roughly described as λ_R changes linearly and T_R changes parabolically versus E. Note that both λ_R and T_R change slopes at – (i) around 0.8 V, where the OH-adsorption starts when E goes to positive direction and (ii) around 0.5 V, where desorption starts when E goes to negative direction.

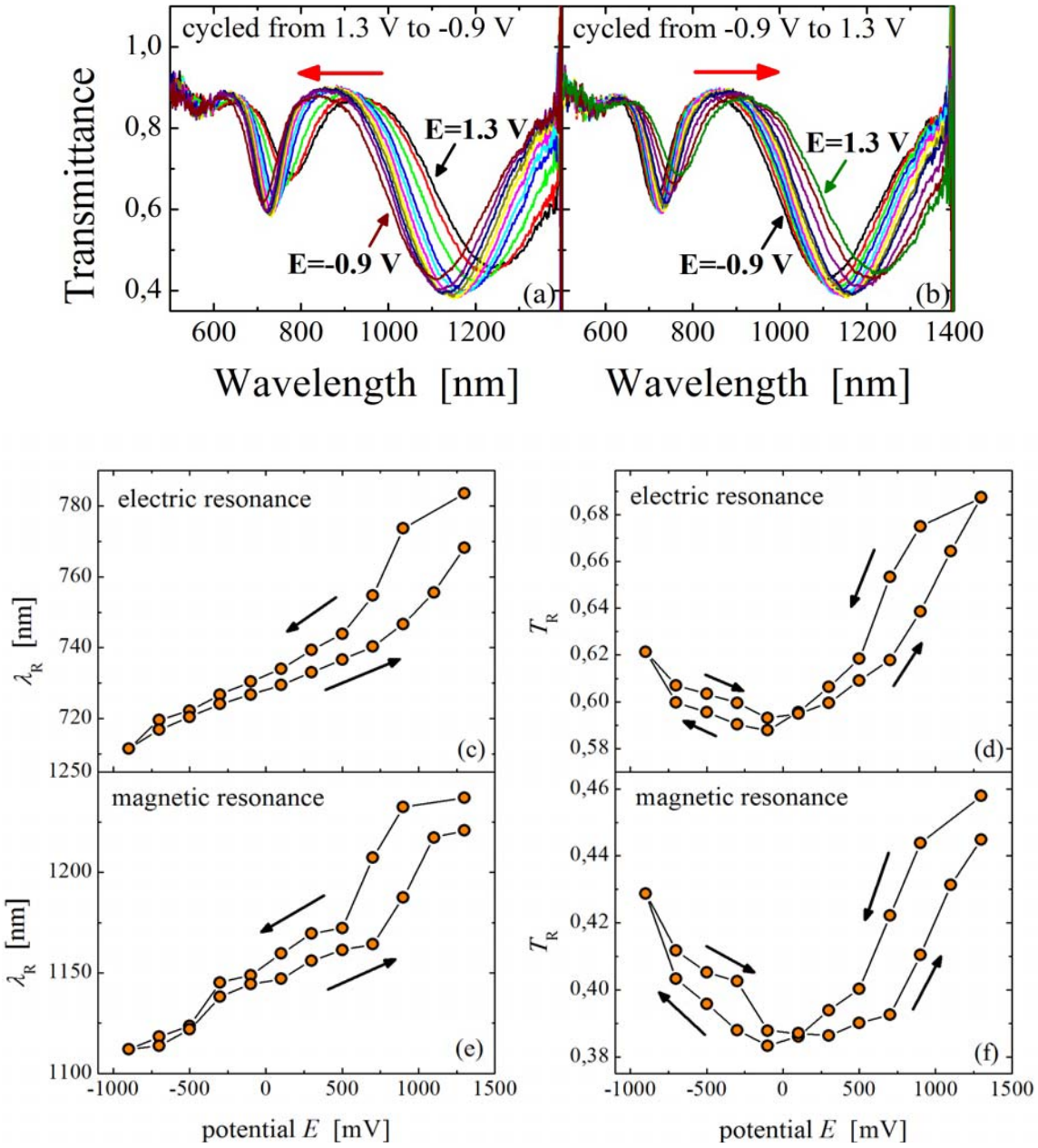

Figure 5.4 In-situ optical measurement results of arrays of 10 nm thin gold split-ring resonators with horizontal polarization incident light, and in 0.7 M aqueous NaF electrolyte with electrode potential window from –0.9 to +1.3 V. (a), (b) Normal-incidence transmittance spectra. (c), (d) and (e), (f), The corresponding resonance wavelength, λ_R, and transmittance, T_R, versus potential, E, of the electric resonances and the magnetic resonances, respectively.

The magnetic resonance disappears for vertical incident polarization as shown in Figure 5.5 (a) leaving behind only the electric resonance with a 77 nm shift of the transmittance spectrum peak. In this case, the electric field of the light leads to a charge accumulation at the surfaces of the vertical SRR arms, resulting in a depolarization electric field. Depending on the permittivity of the metal, also depending on the frequency of light, this depolarization field can enhance or suppress the external electric field. And therefore, a electric resonance can be measured. The resonance wavelength λ_R and transmittance T_R change linearly and parabolically with E as shown in Figure 5.5 (b) and (c), respectively, which agree closely with those represented in Figure 5.4 (c) to (f).

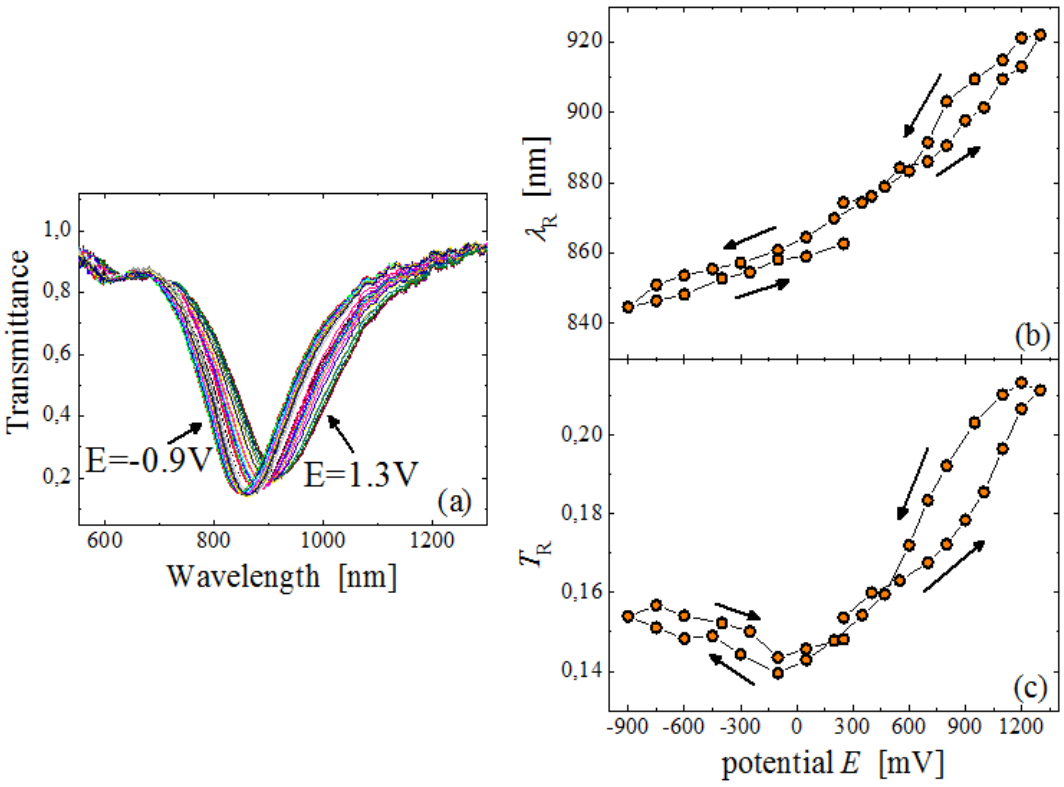

Figure 5.5 In-situ optical measurement results of arrays of 10 nm thin gold split-ring resonators with vertical polarization incident light, and in 0.7 M aqueous NaF electrolyte with an electrode potential window from –0.9 to +1.3 V. (a) Normal-incidence transmittance spectra. (b), (c) The corresponding resonance wavelength, λ_R, and transmittance, T_R, versus potential, E.

5.1.3 Reproducibility

Since the electrochemical training as described above is clearly irreversible, it is important to ask whether the modulation of the photonic metamaterial is reversible and reproducible within several electrochemical cycles. Hence, in the following experiment, a sample with 6 nm Au resonators is scanned in the potential window from −0.9 V to +1.3 V for 10 cycles as during the previous training process. Then the sample is measured with vertical polarized incidence for three electro-

chemical cycles. The resulting data for resonance wavelength λ_R and transmittance T_R are shown in Figure 5.6. It is obvious that after three cycles the average λ_R shifts to blue and also the T_R does not quite recover its original position.

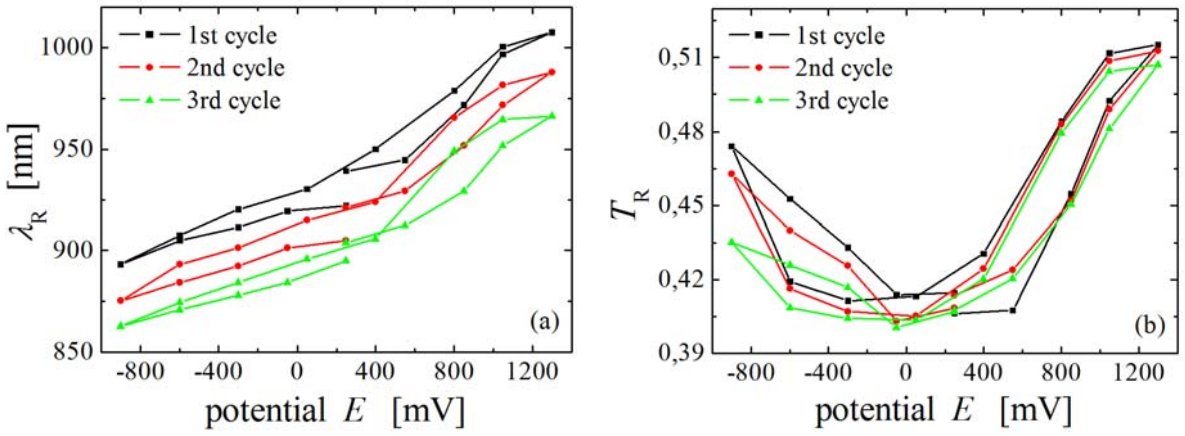

Figure 5.6 In-situ optical measurement results of arrays of gold split-ring resonators with thickness of 6 nm and vertical polarization incident light after a 10 cycles training process. Measured in 0.7 M aqueous NaF electrolyte with an electrode potential window from –0.9 to +1.3 V for 3 cycles (black square: 1st cycle; red dot: 2nd cycle; green triangle: 3rd cycle). (a) Resonance wavelength, λ_R, and (b) Resonance transmittance, T_R, versus potential, E.

Then a new sample with the same structure is cycled for a long time (ca. 6 hours for 100 cycles) in the same potential window from −0.9 V to +1.3 V for training, and then measured for three cycles. It is found that both of λ_R and T_R are very reproducible as shown in Figure 5.7. However, the shift of the spectrum peak decreases a lot – from ca. 100 nm (Figure 5.6 (a)) to ca. 30 nm (Figure 5.7 (a)).

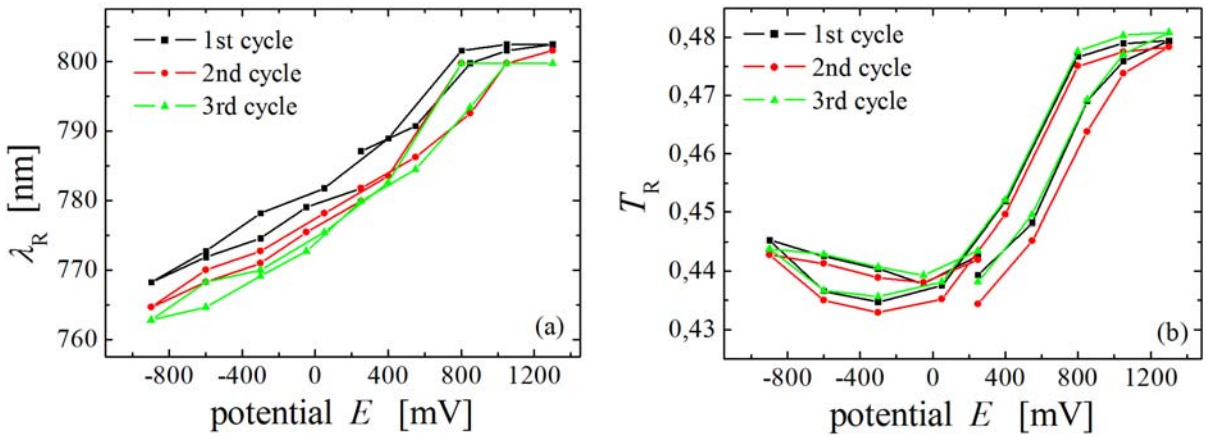

Figure 5.7 In-situ optical measurement results of the same sample and under same measurement condition as shown in Figure 5.6, but for a longer training time (ca. 6 hours for 100 cycles). (a) Resonance wavelength, λ_R, and (b) Resonance transmittance, T_R, versus potential, E. (black square: 1st cycle; red dot: 2nd cycle; green triangle: 3rd cycle). Note the good reproducibility but smaller effect.

Now the question is raised what fraction of the 77 nm wavelength shift in Figure 5.5 is reversible and what fraction is irreversible. To address this important question, the electrode potential was scanned several times for two smaller potential windows while observing the transmittance spectra for similar samples. The resulting resonance positions are summarized in Figure 5.8 and Figure 5.9.

Following the above 10-cycles training procedure in the potential window from −0.9 V to +1.3 V, the measurement with the small potential window ranging from –0.5 V to +0.9 V was started and the results are shown in Figure 5.8. The three depicted complete cycles reveal little if any irreversible effect.

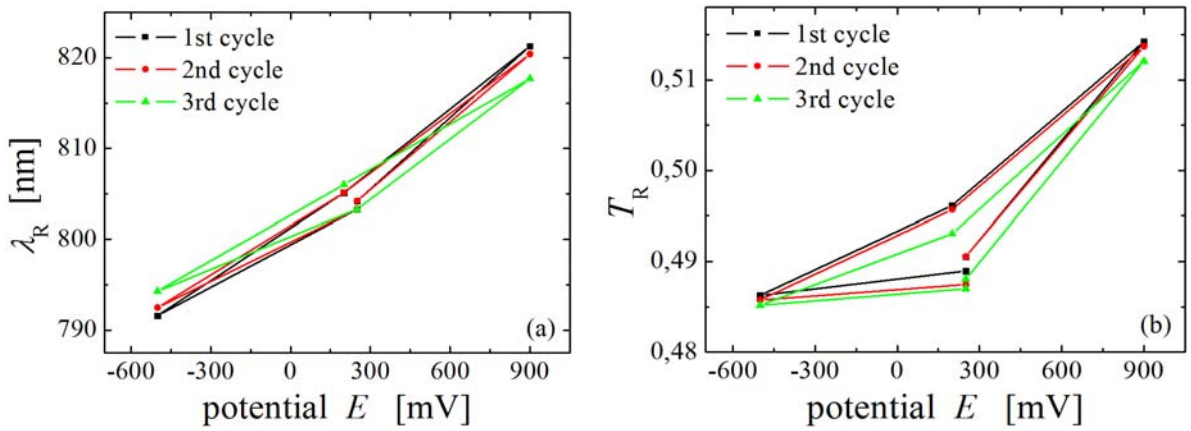

Figure 5.8 In-situ optical measurement results measured with a small potential window ranging from –0.5 V to +0.9 V after 10-cycles training procedure of the similar sample and under similar measurement conditions as shown in Figure 5.6. (a) Resonance wavelength, λ_R, and (b) Resonance transmittance, T_R, versus potential, E. (black square: 1st cycle; red dot: 2nd cycle; green triangle: 3rd cycle). Note the good reproducibility.

Next, the measurement potential window is increased from –0.9 V to +0.9 V in Figure 5.9. Obviously, the modulation becomes somewhat hysteretic and exhibits a drift towards smaller wavelength, i.e., the resonance does not quite come back to the same position after one cycle (Figure 5.9 (a) and (b)). However, this irreversible part essentially saturates after another 100 cycles from –0.9 V to + 0.9 V as shown in Figure 5.9 (c) and (d). Here, reversible transmittance shifts as large as 51 nm are obtained. Even though the potential window used here is smaller (0.4 V smaller) compared to the graph in Figure 5.5, one can still concludes that at least 70% of the wavelength shift in Figure 5.5 is reversible. It is assigned that the irreversible contributions from structural changes similar to those during the initial training. And therefore, the training method can be used for improving the resonance quality as the following procedure: (1) cycle the sample in 0.7 M NaF from –0.9 V to +1.3 V at a scan rate of 20 mV/s for 10 times; (2) then decrease the potential window, which is from –0.9 V to +0.9 V and cycle for 100 times at the same rate. After this procedure, one can obtain reversible and reproducible plasmonic resonances.

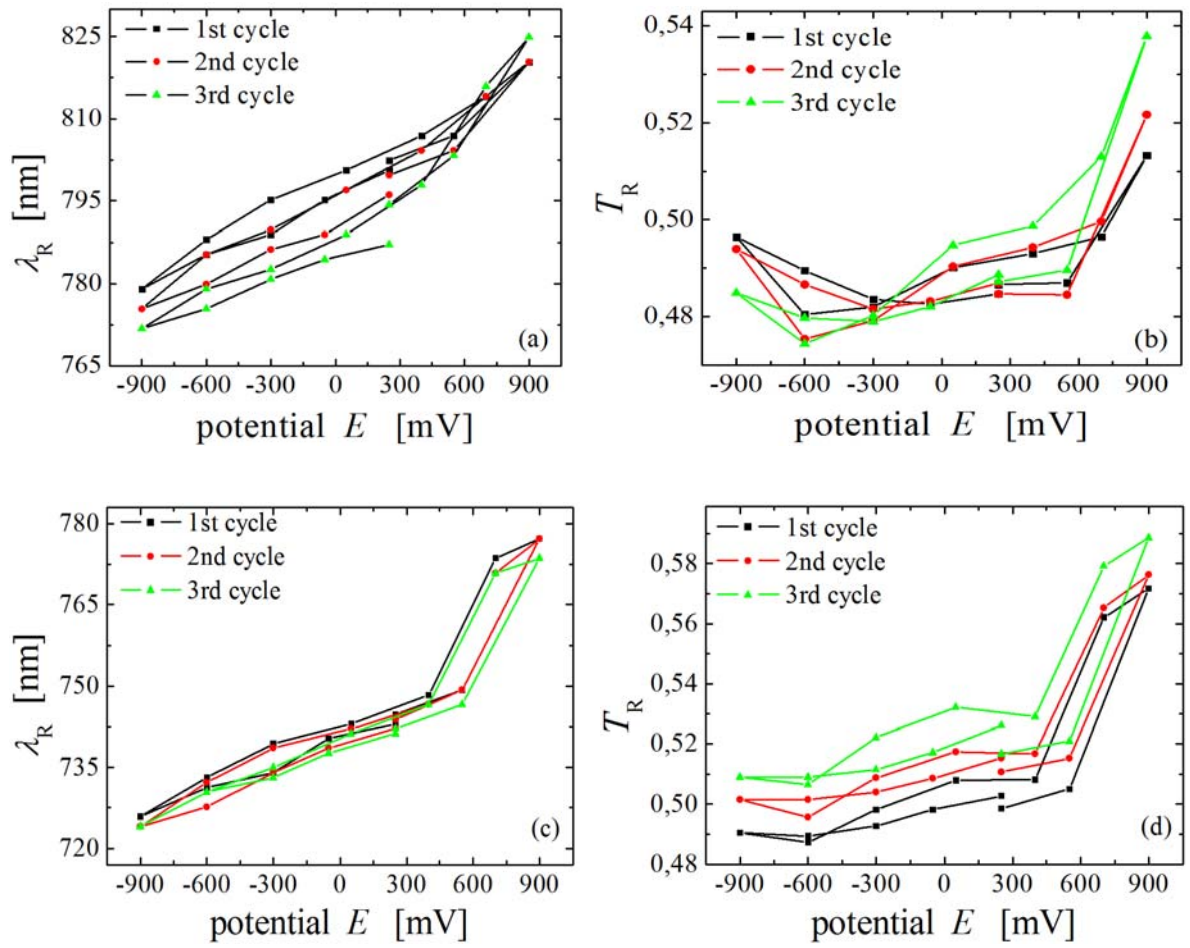

Figure 5.9 In-situ optical measurement results measured with the potential window ranging from –0.9 V to +0.9 V of the similar sample and under similar measurement condition as shown in Figure 5.6. (a), (b) Resonance wavelength, λ_R, and resonance transmittance, T_R, versus potential, E after a 10 cycles training procedure. (c), (d) The same parameter but after another 100 cycles from –0.9 V to +0.9 V. (black square: 1st cycle; red dot: 2nd cycle; green triangle: 3rd cycle). Note the good reproducibility and large effect.

5.1.4 Optical and electrochemical responses

In order to figure out the relation between the optical and electrochemical signals, the chrono-amperometry (please see subsection 2.1.4.4) is used here, i.e. potential jumps between –0.9 V and +0.9 V to measure the current change vs. time. The incident beam was set at constant wavelength (710 nm) to measure the transmittance change vs. time in-situ. The results are summarized in Figure 5.10. When the potential jumps from +0.9 V to –0.9 V, the current becomes stable after a short time (less than 5 s). This is much faster than the optical signal. However, when the potential jumps back to +0.9 V, the reaction rates are similar for both the current and the transmittance.

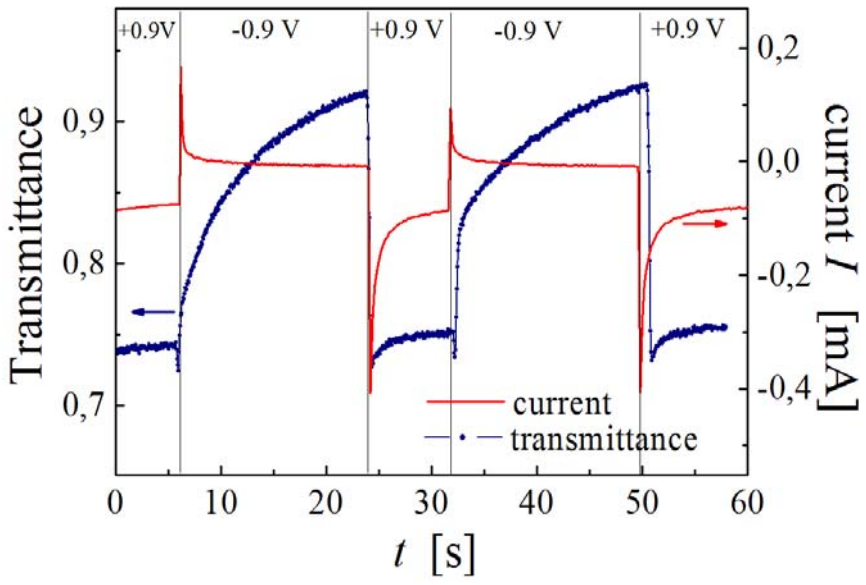

Figure 5.10 Transmittance and current change versus time when the potential stepped between –0.9 V and +0.9 V. Note the current reaction is much faster when potential jumps from positive to negative values.

5.1.5 Relation between resonance modulation and sample thickness

To further probe the mechanism behind this electrically tunable resonances, additional experiments have been performed in which the gold SRR thickness was varied systematically. Clearly, we expect smaller reversible resonance transmittance shifts from surface-charge effects for thicker Au resonators due to the less favorable surface-to-volume ratio. Results of corresponding experiments measured in the potential range from –0.9 V and +0.9 V are shown in Figure 5.11. In all cases, the samples have been "trained" before the measurement. As expected, for a given modulation potential within the reversible regime, the observed resonance wavelength shift $\Delta\lambda_R$ decreases with increasing gold thickness, d, of the SRR, approximately proportional to $1/d$. It is known that the surface-to-volume ratio is proportional to $1/d$, hence, a tentative conclusion can be given that the resonance wavelength shift $\Delta\lambda_R$ is proportional to surface-to-volume ratio.

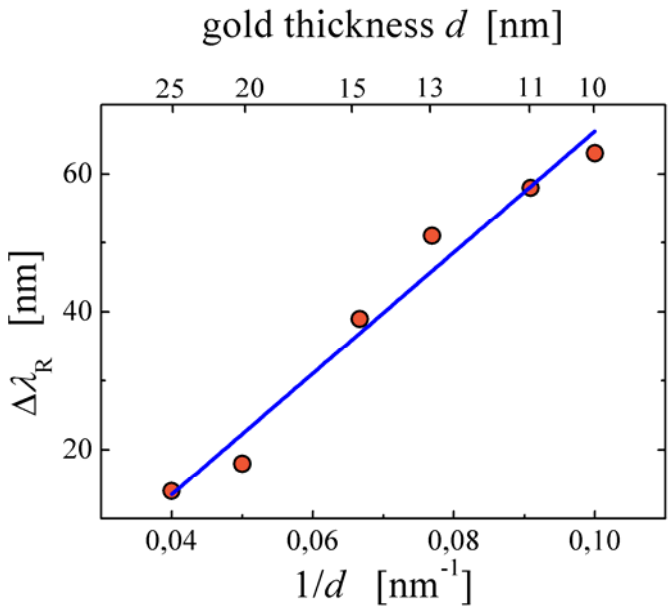

Figure 5.11 The resonance transmittance modulation (largest resonance transmittance shift) of a split-ring-resonator versus the inverse, 1/ *d*, of the gold thickness. In all cases, after the 10-cycles training procedure, the electrode-potential is varied in the range from –0.9 V to 0.9 V following 100 electrochemical cycles. Obviously, the reversible modulation is more pronounced for thin gold structures due to their larger surface-to-volume ratio. The blue line is a linear fit of the data points.

5.1.6 Underpotential deposition (UPD)

Metal adatoms in a submonolayer are believed to have electronic properties that can deviate significantly from those of the bulk material. In addition, the adsorbate layer may also alter the electronic properties of the substrate material itself, at least near the surface.

The adsorption and deposition of metal atoms on foreign metal substrates represents a very attractive system for studies because the strong adatom/substrate bonding can control the growth behavior and the resulting structures, especially as a function of surface coverage. Particularly attractive is the study of such systems by electrochemical means, especially within the context of underpotential deposition (UPD) [126-128]. UPD refers to the electrodeposition of a metal monolayer on a foreign metal substrate at potentials positive with respect to that for bulk deposition on the same metal surface. Such phenomena allow for the precise and reproducible control of the surface coverage and for the study of coverage dependent properties including the structure of the metallic adlayer and its electronic properties.

In order to figure out the dependence of photonic resonance modulation on surface electronic properties (e.g. surface resistance), lead and copper UPD on gold SRR structures (10 nm) are investigated. Before any measurement on the sample, the bared ITO substrate is measured in the same electrolyte for UPD test under the same conditions. The CVs on the ITO film just showed a featureless small double layer current in the whole potential window which will be used in the following experiments, which means the UPD process is not active on the ITO substrate.

5.1.6.1 Pb UPD on Au

In order to get precise deposition/desorption signatures of Pb UPD on a Au surface, a Au foil was measured in 1 mM $Pb(NO_3)_2$ + 0.1 M NaOH aqueous solution and the resulting CV is shown in Figure 5.12 (a). The CV presents pairs of peaks at negative potential ($E < 0$), where the UPD process happened. The Pb deposition starts at –0.2 V, followed by the first deposition peak at –0.4 V, then a much smaller feature at –0.55 V and a well defined peak at –0.75 V, where a monolayer Pb has deposited on the Au surface. It has been shown that the initial stages of Pb deposition take place on terrace edges [129,130]. Hence, the peaks at higher underpotentials in Figure 5.12 (a) correspond to the partial Pb deposition when the scan goes to the negative direction at $E < 0$. After one monolayer Pb deposition, the potential is scanned to the positive direction, and three corresponding desorption peaks can be identified even though the third one is quite small. All the Pb atoms have been removed from the Au surface after the last desorption peak at –0.4 V.

As soon as the detailed electrochemical features have been obtained, the in-situ optical measurement can be carried out. The potential range used for Pb UPD is from 0 V to –0.76 V. Note that the most negative potential is particular important in UPD experiment on thin Au resonators samples. Because the Au resonators' structure will be damaged if bulk Pb deposition happened since it is an irreversible process. And what's more, the UPD process is dependent on the surface quality of the electrode as shown in a review paper [131]. The surface status is always different from sample to sample. Therefore, the CV measured on the Au foil only gives a rough reference about the deposition/desorption peaks on the Au SRR samples. The corresponding transmittance spectra, resonance transmittance T_R and resonance frequency ω_R (in this section, resonance frequency is plotted for analysis convenience based on the equation $\lambda_R \times \omega_R = c$, where c is the speed of light) were plotted with respect to the potential E as shown in Figure 5.12 (b) to (d). A large resonance peak shift can be observed, and both T_R and ω_R change linearly with potential. In Figure 5.12 (c) and (d), the curves change slopes at $E = -0.4$ V, where the first deposition and last desorption peaks are. And ω_R stays at constant value at the most negative potentials, i.e. $E \leq -0.72$ V, which means one monolayer Pb has been deposited on the Au surface. Then the potential scans to the positive direction, the curves change slope at around $E = -0.6$ V, where the first desorption peak is.

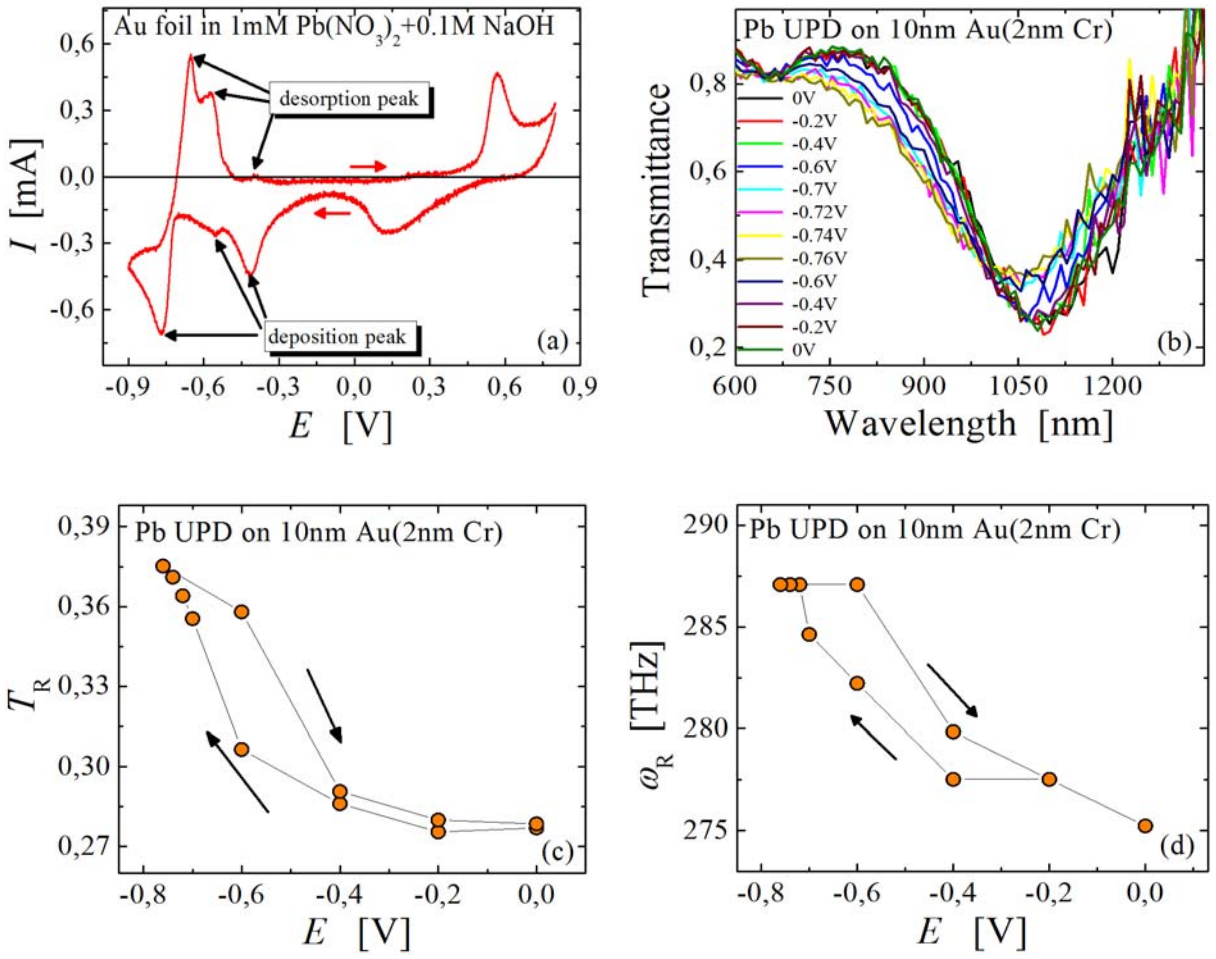

Figure 5.12 Lead underpotential deposition (UPD) on gold in 1 mM $Pb(NO_3)_2$ + 0.1 M NaOH aqueous electrolyte. (a) Cyclic voltammogram measured on a gold foil. (b) to (d) In-situ optical measurement results of arrays of 10-nm thin gold split-ring resonators during UPD process. (b) Normal-incidence transmittance spectra. (c), (d) The corresponding resonance wavelength, λ_R, and frequency, ω_R, versus potential, E.

5.1.6.2 Cu UPD on Au

An evaporated 30 nm thin Au film on a glass substrate was measured in 5 mM $CuSO_4$ + 0.1 M H_2SO_4 aqueous solution as a pretest before the in-situ optical measurement on SRR arrays taking place. The CV of Cu UPD on Au film in Figure 5.13 (a) shows one pair of well-defined and sharp peaks at $E = \sim 0.32$ V, and a broad shoulder at lower underpotentials. The transmittance spectra, resonance transmittance T_R and resonance frequency ω_R measured on Au SRR samples are shown in Figure 5.13 (b) to (d), where a very small resonance peak shift can been observed. Even though, the curves can still indicate the electrochemical features, especially the resonance transmittance curve as shown in Figure 5.13 (c), it changes its slope significantly at $E = \sim 0.3$ V where the adsorption/desorption peaks are observed.

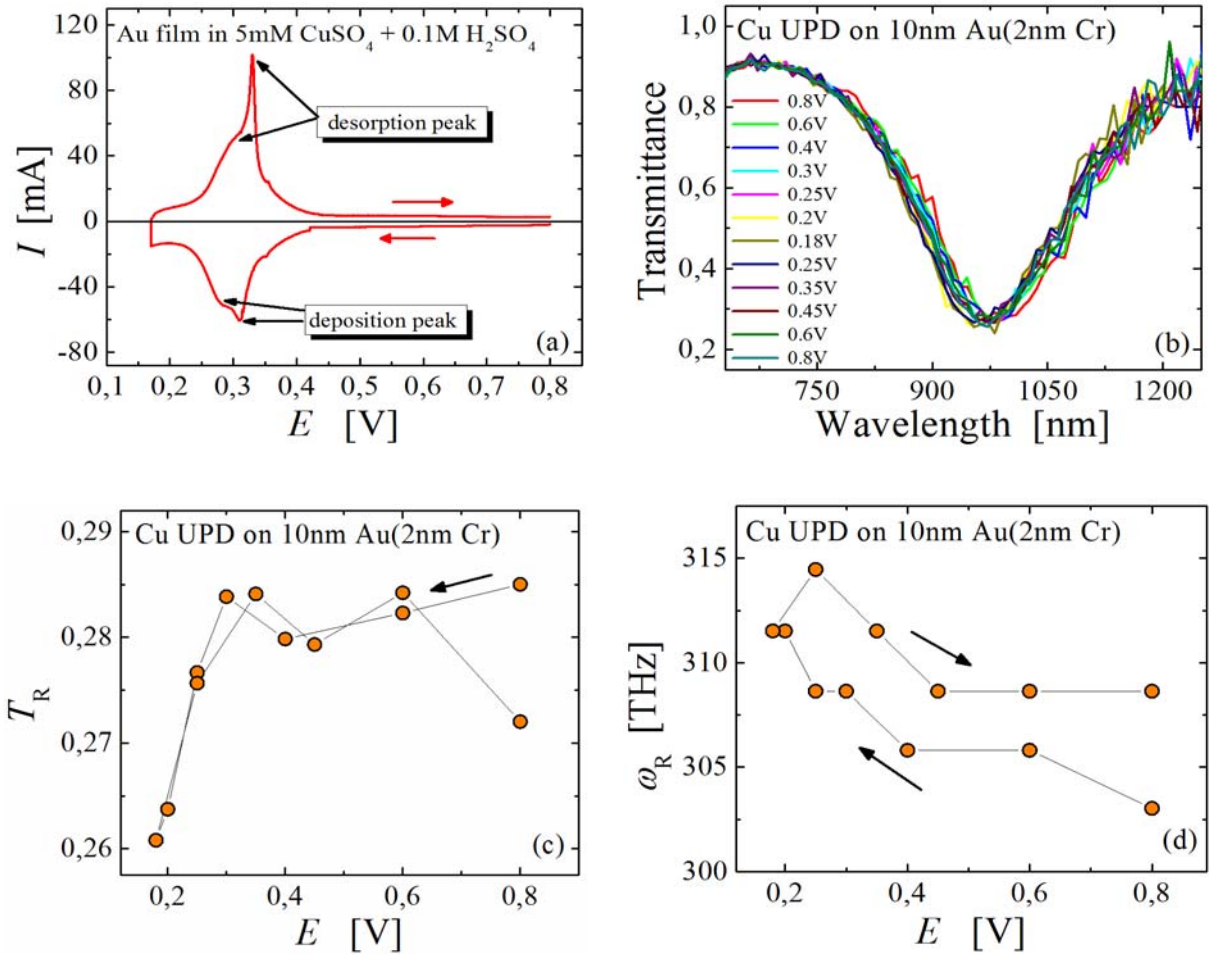

Figure 5.13 Copper underpotential deposition (UPD) on gold in 5 mM $CuSO_4$ + 0.1 M H_2SO_4 aqueous electrolyte. (a) Cyclic voltammogram measured on 30 nm thin Au film on glass substrate. (b) to (d) In-situ optical measurement results of arrays of 10-nm thin gold split-ring resonators during UPD process. (b) Normal-incidence transmittance spectra. (c), (d) The corresponding resonance wavelength, λ_R, and frequency, ω_R, versus potential, E.

As introduced in section 5.1.1, the most important features of the CVs in Figure 5.1 (a) are the OH-adsorption peaks during positive-going scans and the corresponding desorption peaks during negative-going scans in the potential range $E > 0$, which can also be treated as an OH UPD process. The corresponding results are summarized in Table 5.1 (cf. page 76).

5.2 Discussion

5.2.1 ITO substrate effect

The transmittances of the bare ITO substrate were measured both at different potentials and at different positions. The results show that there is no difference between the transmittance intensity. And the reproducible results can be obtained even after a longer time (e.g. 24 hours) of electrochemical cycling. Thus, an effect of the ITO substrate on the measurement of gold SRR samples can be excluded.

5.2.2 Explanation of electrochemical training phenomena

The training effect clearly shows that the resonance gradually becomes sharper and shifts toward the higher frequency during the initial potential cycles. This effect can be phenomenologically explained by a decrease in the resistance and capacitance of the gold nanostructures due to surface smoothening. It has been reported that transient roughening, accompanied by an increase in surface diffusivity, accompanies the oxidation/reduction treatment of noble metal electrodes [132,133]. In our experiments, the "smoothening" only happened when we included an oxidation/reduction potential window ($E > 0.9$ V), and from the Lippmann equation it is known that in this potential window the gold-electrolyte surface tension is reduced [34]. The reduction in the surface tension of the gold-electrolyte interface favors wetting of the substrate by gold and, therefore, a smoother surface. Thus, it can be concluded that the change in the optical properties is accompanied by a clear restructuring of the gold atoms within the SRRs that is most pronounced for very thin resonators.

5.2.3 Effect of Au thickness on resonance modulation

A recent density-functional-theory study [134] of charged Au surfaces suggests that the potential variation affects the electron density exclusively within the topmost atomic layer at the surface. Furthermore, the position of the image plane changes in good agreement with the notion of an electron liquid in which the charge density is a constant and the extra charge is accommodated by an outward shift of the surface of the electron liquid. This motivates us to view the modulation of the metal's surface charge, naively, as an effective change of the SRR metal-film thickness. To verify this reasoning, the following calculation has been performed.

It has been reported that the average location of the excess charge z increases (the center of the excess charge distribution moves outwards) with increasing excess electron density q (see Figure 5.14 (a)) with the relation $z = c\,q$, where $c = 1.06\times10^{-10}\ \mathrm{m^3C^{-1}}$ [134]. The charge density q in the CVs as shown in Figure 5.1(a) is around 3.7 C $\mathrm{m^{-2}}$, from which we can calculate that z emerges as 0.4 nm. In Figure 5.14 (b), the average resonance wavelength λ_{RAVG} versus d is plotted and the experiment data points were fitted linearly. Thus, the relation between λ_{RAVG} and d can be ob-

tained as: $\lambda_{RAVG} = 981 - 12\,d$, thus $\Delta d = \Delta\lambda_{RAVG}/12$. Take the sample shown in Figure 5.9 as an example that $\Delta\lambda_{RAVG}$ is 51 nm, which means the thickness increase Δd is around 4 nm. Even though the increase of excess charge location on the lateral sides of the resonators is taken into account, the total location increase Δz is still significantly smaller than the calculated thickness change Δd, which emerges as 4 nm. Hence, the effective thickness change might play a certain role but it is quite unlikely to dominate in our experiments.

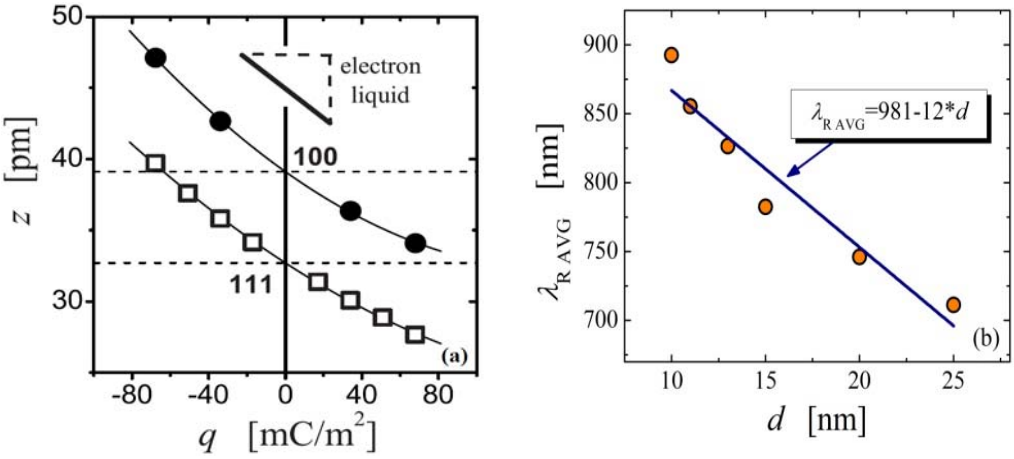

Figure 5.14 (a) Average location of the excess charge, z, versus net excess charge density, q, for (111) and (100) surfaces [134]. Solid lines represent parabolic fits to the data. (b) The average resonance wavelength λ_{RAVG} of a split-ring-resonator versus gold thickness d. In all cases, after the 10-cycles training procedure, the electrode-potential is varied in the range from –0.9 V to 0.9 V following 100 electrochemical cycles. The blue line is a linear fit of the data points.

5.2.4 Mechanism of electrochemical modulation of optical resonance

In the present work, the space-charge or adsorbate coverage at the surface of each resonator is controlled via an applied potential, and this leads to a reversibly tunable optical resonance. While the underlying mechanism is not understood, it is natural to suspect a coupling between the optical response and the electric resistivity. In fact, large potential-induced resistance changes are observed in thin metal films, nanoporous metals and oxides [10,11,135]. Since thin metal films (i.e., films with thickness $d < 30$ nm) have a large surface-to-volume ratio, they have been regarded as 'all surface' [136], and their electronic transport is strongly affected by interfacial phenomena [137]. The notion of "surface resistance" refers to the phenomenon that the resistivity (or conductivity) of these materials can be significantly influenced by the electron scattering at the surface, for instance due to electron-phonon collisions [138]. Surface scattering is affected by impurities, defects and charge carrier concentration at the interface of the exposed sample surface. Thus, surface resistance change has been used for a long time to study adsorption of gases, foreign metal atoms and ionic or molecular species on different thin metal films. It has also been involved for verifying models of the resistance change versus metal film thickness and surface adsorbates coverage (see Ref. [137] and references therein). Therefore, it is of interest to investigate the surface resistance effect in the context of our resonance modulation experiment.

Section 5.1.1 showed that after the training process, the resonance peak significantly shifts to a higher frequency and also the damping becomes smaller (i.e. the spectrum is narrower) compared to fresh samples with rough surfaces. This phenomenon might be connected to a resistance change: The charge carrier scattering – and, hence, the resistance – at the solid-electrolyte interface depends on the surface roughness, with lower resistance at smoother surfaces [137]. In other words, the reduction of the SRR resistance during training coincides with a resonance with higher frequency and less damping. The link between resistivity and frequency is supported by the plot in Figure 5.15, which shows that the average resonance frequencies, ω_{RAVG}, of SRRs are directly proportional to their thicknesses. Since the resistance increases as the film thickness is reduced, the observations imply a reduction of ω_{RAVG} with decrease in d. However, please note that the variation of ω_{RAVG} with film thickness (and, in the spirit of our discussion, with film resistance) is slow: Figure 5.15 shows a relative change in ω_{RAVG} by merely ~25% while d varies by the factor 2.5.

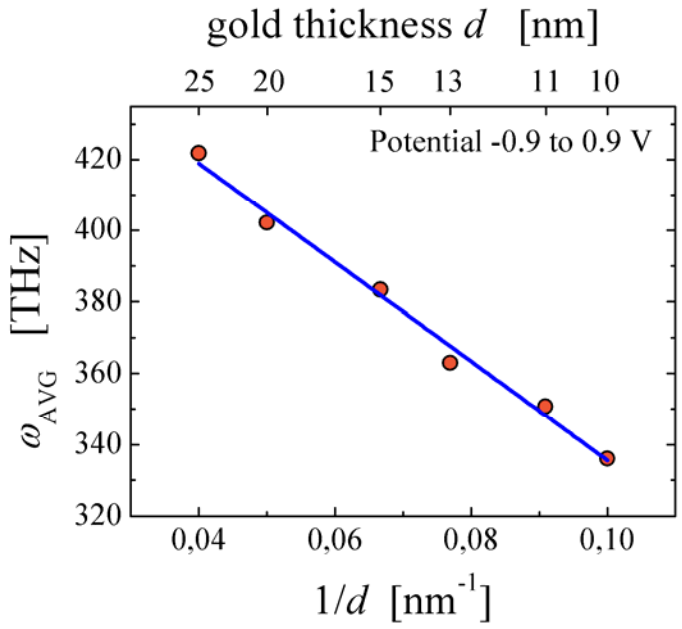

Figure 5.15 An alternative representation of the data of Fig 5.14(b) is to plot the average resonance frequency, ω_{RAVG} of split-ring-resonator versus the inverse, $1/d$, of the gold thickness. In all cases, after the 10-cycles training procedure, the electrode-potential is varied in the range from –0.9 V to 0.9 V following 100 electrochemical cycles. The blue line is a linear fit of the data points.

Now, it is important to verify the proposition that the resistance change is the main reason behind the phenomena which we observed in the optical measurement. If this is the case, what is the mechanism that links the resistance to the optical properties? The resistance change of the resonators in the photonic metamaterial is not known. However, resistance changes have been reported for thin gold films subject to different electrochemical processes. Examples are the OH-, Pb and Cu adsorption and desorption [139,140]. The results of these studies are summarized in the first column of Table 5.1. They document resistance changes of around 1 - 10%, depending on the nature of the adsorbate, for films with thickness around 30 nm. The resonators of the present study were significantly thinner, around 10 nm. It is then natural to assume that the resonators suffer even larger resistance changes than what was found in the studies using thin films.

Table 5.1 Resistance, resonance transmittance and frequency change during underpotential deposition of different anions. R is the resistance of a thin gold film. The relative resonance transmittance and frequency changes of Au resonators are $\Delta\omega_R/\omega_{avg}$ and $\Delta T_R/T_{avg}$, respectively. The sign of the derivatives $\delta T_R/\delta\Theta$, $\delta\omega_R/\delta\Theta$ and $\delta(\Delta R/R)/\delta\Theta$ are listed to show the trends of how T_R, ω_R and also the resistance $\Delta R/R$ change with the adsorbates coverage Θ, and the sign of $\delta\omega_R/\delta E$ shows the trend of how ω_R changes with the applied potential E.

	$\Delta R/R$ %	$\Delta T_R/T_{avg}$ %	$\Delta\omega_R/\omega_{avg}$ %	$\delta(\Delta R/R)/\delta\Theta$	$\delta T_R/\delta\Theta$	$\delta\omega_R/\delta\Theta$	$\delta\omega_R/\delta E$
OH/Au	12.5[139]	28	7	+	+	-	-
Pb/Au	6[140]	30	4	+	+	+	-
Cu/Au	1.2[140]	7	<2	-	-	+	-

In order to summarize the most important observations of the optical properties change during the underpotential deposition experiments, we compare the trends shown in Figure 5.9, Figure 5.12 and Figure 5.13 to the resistance changes given in the Refs. [139, 140]. The following three observations are listed:

1st: The graphs of T_R vs. E show different behavior for different adsorption/desorption processes. However, the trends in T_R vs. E agree with those of the potential-induced resistance change.

2nd: All graphs of ω_R vs. E display similar trend, independent of the electrode process.

3rd: The effect of Cu UPD on both, ω_R and T_R, is much smaller than the effect of Pb UPD and OH UPD.

Below, we shall consider the trends of how T_R, ω_R and also the resistance R change with the adsorbates coverage Θ (e.g., coverage with OH-, Pb, Cu). To this end, Table 5.1 shows the sign of the derivatives $\delta T_R/\delta\Theta$, $\delta\omega_R/\delta\Theta$ and $\delta(\Delta R/R)/\delta\Theta$. The sign of $\delta\omega_R/\delta E$ shows the trend of how ω_R changes with the applied potential E.

The **1st** of the three phenomena listed above can be tentatively explained in the following way:

Based on the Lorentz oscillator model, the transmittance, T, is a function of the frequency, ω of the driving electric field (frequency of the incident light), and this transmittance has a minimum at the resonance frequency ω_R. In the model the amplitude of transmittance spectrum at the resonance frequency, $1-T_R$, is obtained as inversely proportional to the resistance. The classical Lorentz-oscillator lineshape for the transmittance spectrum, T, is [141]

$$T(\omega) \propto \frac{\gamma}{(\omega_R^2 - \omega^2)^2 + \gamma^2} \qquad 5.1$$

where γ is the oscillator damping. Upon reducing γ, the line gets narrower and the transmittance amplitude increases. Precisely, the amplitude of transmittance spectrum at resonance ($\omega = \omega_R$) scales according to

$$1-T_R \propto \frac{1}{\gamma} \tag{5.2}$$

And also it is well known that the damping is proportional to the resistance. This means the amplitude of transmittance spectrum at resonance, $1-T_R$, is inversely proportional to the resistance change. This reasoning agrees with the observation that the trends for T_R vs. Θ and for ΔR vs. Θ are in agreement for all electrode processes investigated here.

From the T_R vs. E curves, it can be found that the resonance transmittance, T, exhibits nearly no change during the capacitive charging process (in the double layer potential range). This suggests that the charge density variation is not the key factor governing the transmittance. Instead, T is more dependent on the adsorption/desorption process. This is consistent with a larger effect of electrosorptin on the resistance as compared to the effect of capacitive charging. However, below I shall argue that the resonance frequency is sensitive to the charge density.

The **2nd** and **3rd** phenomena, and in particular the shift of the resonance frequency can be explained as follows:

The trends of resonance frequency change with adsorbates coverage have different signs for different adsorption/desorption processes. However, the last column of Table 5.1 shows that ω_R displays similar trend with electrode potential E, independent of the electrode process. In contrast to the transmittance change, from the ω_R vs. E curves, one can find that the resonance frequency, ω_R, changes nearly linearly versus E during the whole potential range we used. The observations suggest that the resonance frequency change is not determined by the resistance change alone. Conceivably, the electron density in the metal may be relevant. This could be explained by the theory based on Drude model given in the works of electron-induced surface plasmon resonance shift [142,143]. In Refs. [142,143], the authors also found a blue-shift resonance upon the electron injection or Pb UPD with gold rods or metal particles. The metamaterial samples used in this work are composed of gold split-ring-resonator (SRR), which can be treated as an artificial atom. And the metamaterial is an effective homogeneous material with many SRR atoms. Hence, the optical behavior of our metamaterial can be qualitatively described by the theory for gold particles, which is given as following.

The dielectric behavior of gold can be well approximated with the notion of a free electron gas, which is described in the Drude function with the form of [142]

$$\varepsilon(\omega) = \varepsilon_\infty - \frac{\omega_{pl}^2}{\omega^2 + i\gamma\omega} \tag{5.3}$$

where the bulk plasma frequency is given by

$$\omega_{pl} = \sqrt{\frac{n_e e^2}{m\varepsilon_0}} \tag{5.4}$$

where e is the electron charge, m is the effective mass, ε_0 is the permittivity of vacuum, ε_∞ is the high-frequency contribution from interband transitions, γ is damping and n_e is the electron density. Then for the measured surface plasmon peak central frequency ω, we have [142]

$$\omega^2 = \omega_0^2 \ (1 + \frac{\Delta n_e}{n_e}) \qquad 5.5$$

with

$$\omega_0^2 = \omega_{pl}^2 \ \frac{1}{\varepsilon_\infty + (\frac{1}{L} - 1)\varepsilon_m} \qquad 5.6$$

where ω_0 is the plasmon position for the charge-neutral surface, L is the shape-dependent depolarization factor and ε_m is the dielectric constant of the medium outside the surface. Thus, the resonance frequency shift is

$$\Delta\omega = \omega - \omega_0 = \omega_0 (\sqrt{1 + \frac{\Delta n_e}{n_e}} - 1) \qquad 5.7$$

From equations 5.5 and 5.7, one can find that both the resonance frequency ω and the resonance frequency shift $\Delta\omega$ are directly relevant to the electron density change Δn_e. An increase of Δn_e will lead to the increase of ω and $\Delta\omega$. Qualitatively, the predictions of the free electron plasma frequency agree with the shift of resonance frequency observed in the present work.

One can find that the charge density q scales with the potential E according to

$$C = \frac{q}{E}; \quad \Delta n_e \propto -q \qquad 5.8$$

where C is the capacitance of our sample. Since the electron density change, Δn_e, scales with the negative charge density, $-q$, one can conclude that Δn_e scales with the negative potential range, ΔE^-. The negative potential range used here is $\Delta E^-_{Cu/Au} = 0 < \Delta E^-_{Pb/Au} < \Delta E^-_{OH/Au}$ (positive potential range is used for Cu UPD), which means that the electron density change has following relation that $\Delta n_{eCu/Au} < \Delta n_{ePb/Au} < \Delta n_{eOH/Au}$. Indeed, the effect of Cu UPD on ω_R is much smaller than the effect of Pb UPD and OH UPD. Even though the resonance frequency is inversely proportional to its resistance as shown in Figure 5.15, the small relative change of the frequency might be covered by the electron-induced effect.

According to what has been discussed in this section, the resistance change can be identified as a decisive impact on the resonance transmittance, while the electron density change appears to mainly influence the resonance frequency.

5.2.5 Optical measurement as a monitor for electrochemical processes

It is well know that from cyclic voltammograms (CVs), the electrochemical features on the electrode/electrolyte interface can be clearly indicated, e.g., where the adsorption/desorption happened. And based on these features, the suitable potential range can be easily chosen. However, the electrochemical cycling depends a lot on the experiment conditions, like the purity of the environment (air, electrolyte…), the morphology of the electrode surface (smooth or rough, the

orientation…), and so on. For instance, during the UPD experiment in this work, the deposition/desorption peaks of a Au foil or evaporated film only have a minor difference to that of SRR samples.

On the other hand, as shown in this chapter, the optical measurement results also can be used to indicate the electrochemical processes undergoing on the electrode surface even though the cell used here is open to air. For example, with the resonance transmittance or wavelength (frequency) versus potential curves, the slopes change when adsorption/desorption happened. And furthermore, as shown in Figure 5.10, when the potential jumps from positive to negative values, the current becomes stable after a short time (less than 5 s) while the optical signal does not. This may be related to some reaction on the gold surface, which is detected by the optical signal but the current does not see it. For example, there will be some oxygen contamination in the electrolyte due to the electrochemical cell being open to air. Oxygen might react with water at negative potential where there are some extra negative electrons. Hence, the optical measurement can also be used as a monitor for supervising the electrochemical processes, which is a sensitive and environmental friendly method.

5.3 Conclusion

In conclusion, the work on electrically modulation of photonic metamaterial has lead to two new insights. First, a method is found for postprocessing metallic photonic metamaterial samples to get pronounced resonance with low damping through electrochemical cycling. This approach is complementary to the thermal annealing of photonic metamaterials in that the electrochemical cycling is advantageous if applied to very thin gold resonators. Second, an electrically tunable photonic metamaterial is achieved. The novel concept presented is that the space-charge at the surface of each resonator is modulated by the applied potential in an electrochemical environment. This leads to a reversibly tunable optical resonance, with which one can switch on/off the resonance ideally by an electric signal. The reversible modulation of resonances gives the possibility for application as photonic metamaterial devices. And furthermore through Pb and Cu underpotential deposition experiments, the resistance change has been identified as a decisive impact on the resonance transmittance, while the electron density change appears to mainly influence the resonance frequency.

6 Summary and outlook

The main achievements of the present thesis are the successful exploitation of metallic-based tunable nanomaterials and the presentation of their novel functions for actuation and photonics applications. The underlying mechanism is introducing a controlled space-charge region localized at the surface of the metallic nanoscale structured materials. An applied voltage can change their local properties such as the interatomic bond forces and also the surface electronic structure. These changes of local properties are sufficient to tune the macroscopic properties of these materials. This work also proposes concepts for the underlying fundamental processes behind the functionality. The details will be summarized in the following paragraphs.

This work experimentally validated the theory on distinction between different capillary forces and suggested the mechanism for capillarity-driven deformation of porous materials for the first time. The experiments were performed with nanoporous gold samples through: (1) dilatometry to probe the change in macroscopic sample dimension and (2) in-situ wide-angle x-ray diffraction to probe the variation in the lattice parameter of the gold crystal lattice, under potential control in the electrolyte. The resulting two strains showed a significant difference with a ratio of ~ 2, which confirms that the strain in response to the action of the surface stress at the solid surface and the strain in response to changes in the pressure in the fluid are fundamentally different. If there is only one capillary force action, i.e. the pressure in the fluid, the strain should be constant whatever measures are used. The finding here suggests that the theory given in previous reported works [13,20-22] is inappropriate, where the sorption strain and the capillary condensation in porous solids were discussed only in relation to the pressure in the fluid. Such models may be improved by incorporating surface stress and its origin, i.e. changes in the bond forces between the surface atoms of the solid phase.

Using nanoporous metals, one can achieve large strain amplitude and high mechanical energy density in a stiff actuator material. The basic idea is to change the surface stress of the metal when in contact with an electrolyte by potential variation. A similar concept may be applied to carbon aerogels. Carbon aerogel (CA) is a light-weight, low cost porous material with extremely large surface area that can be loaded in compression. In this work, the first electrically tunable CA actuator is achieved. The new material has a huge and reversible volume strain up to 6.6%. Its mass-specific strain energy density even exceeds that of piezoceramics and of nanoporous metal actuators.

Besides their use in actuation, nanoporous solids impregnated by electrolyte are also of interest with regard to the measurement of the potential of zero charge (*pzc*). Thus, in the present investigation the *pzc* was measured by a standard technique – impedance spectroscopy – for CA and glassy carbon (GC) samples. The measured *pzc* values are 90 mV and 70 mV for CA and GC, respectively – which agree well with the reported value. Comparing the linear variation of dimension change versus potential to the measured *pzc* value of CA, a conclusion can be given that the *pzc* does not coincide with the potential of maximum stress. This confirms the aforementioned distinction between the capillary forces. The observation here indicates that the method used in previous work to determine the *pzc* of a solid material by the potential where the strain is at its

minimum is inappropriate [35,36]. Therefore, the *pzc* of solid materials can only be measured by a standard technique, for instance, impedance spectroscopy.

Another instance for the concept of tunable nanomaterials are electrically tunable photonic metamaterials, which were firstly exploited in this work. The metamaterials used here consist of arrays of lithographically nanostructured gold split-ring resonators. The novel concept presented here is that the space-charge at the surface of each resonator is modulated by the applied potential in an electrochemical environment. This leads to a reversibly tunable optical resonance, with which one can switch on/off the resonance ideally by an electric signal. The reversible modulation of resonances gives the possibility for application as photonic metamaterial devices. While the underlying mechanism is not conclusively understood, it is natural to suspect a coupling between the space charge and the electric resistivity. As a consequence, the resonance frequency of the metamaterials as well as the damping could be reversibly shifted. In fact, large potential-induced resistance changes have been observed in thin metal films, nanoporous metals and oxides [10,11,135]. Here, experiments using Pb and Cu underpotential deposition were performed, and the trends in the results support the notion of a decisive impact of the resistance on resonance damping, while the electron density change appears to mainly influence the resonance frequency.

In addition to this modulation effect, a method is found to improve the quality of the resonators. During the initial electrochemical cycles within a potential range from −0.9 V to +1.3 V, the damping of the plasmonic resonances has significantly decreased. The damping reduction persists when executing further cycles or removing the metal nanostructures from the electrolyte. This 'training effect' can be phenomenologically explained by a decrease in the resistance and capacitance of the gold nanostructures due to surface smoothening. The surface becomes smoother after electrochemical cycling in a large potential window, which is due to an enhanced mobility of gold atoms associated with a transient increase in surface diffusivity during the lifting of the oxygen adsorbate layer at the positive end of the potential scale. This training method can be used as a post-procedure to fabricate resonators with good quality.

Through this whole work, all of the achievements are based on the idea that by introducing a space-charge layer located at the surface of nanomaterials by an applied voltage in an electrolyte one can tune their macroscopic properties and then obtains the desired functions. At first sight, this method seems to be quite easy to apply. However, the truth is that there is a lot of work to do for the fundamental understanding of the physics behind these phenomena, and also the difficulty of combining the various techniques together. Therefore, improvements are still applicable on those topics which have been discussed in this work.

For example, we have experimentally proved that the surface-induced stress can induce very large dimensional changes of a porous material. To efficiently take advantage of this surface stress effect to obtain much larger strain with a stiffer and inexpensive porous material could be an interesting topic. One can try to synthesize nanoporous copper, nickel or other inexpensivemetals or composite material for this electrochemical actuator application.

This applies as well for the carbon aerogel actuators presented in section 4.2, they are also promising for application with their large strain and high mass-specific energy density. While their slow reaction and relatively small Young's modulus are impediments for widespread use. Hence, how to enhance the strain rate to improve the actuation attractiveness should be figured out in future works, e.g. by using an ionic liquid in a rigorous inert gas environment. And how to make this material stronger could also be interesting. For example, by synthesis of a composite carbon aerogel material reinforced by some strong fiber, like carbon nanotube, metal or ceramic

particles. On top of that, from a fundamental research point of view, the reason for the strain-potential curve of carbon aerogel to have different behavior within different electrolytes is still worth being explored.

For the photonic metamaterials, their unnatural optical property gives these materials a bright prospect. The electrical tailoring and modulation as presented in this work takes the first step for possible application of metamaterials. Therefore, how to precisely control the resonance frequency and to fabricate durable, easy to manipulate new photonic metamaterial devices are also worth further studying in the future. And this electrochemical modulation method might also be applicable to silver, since silver has been interesting for metamaterial fabrication because it's less expensive than gold. However, a special electrochemical technique needs to be employed with silver, as it is very easily oxidized during electrochemical processes.

In conclusion, the ranges of variances, novel properties and applications of nanomaterials are extraordinarily huge, as indicated as early as in 1959 by physicist Richard Feynman's talk entitled "*There's Plenty of Room at the Bottom*". He commented that there were no fundamental physical reasons that materials could not be fabricated by maneuvering individual atoms. Nanomaterials have actually been produced and used by humans for hundreds of years, some of the techniques used were considered trade secrets at that time, and are not wholly understood even now [2]. Hence, there is a big fortune waiting for people to dig in. The novel synthesis, characterization and applications of functional nanomaterials is still an exciting and promising field of research.

7 References

[1] K.T. Ramesh. *Nanomaterials: Mechanics and mechanisms*. Springer, New York (2009).

[2] K. Hickman. *Nanomaterials: It's a small, small world*. DOI: j.d.pacey.1085664858.

http://www.csa.com/discoveryguides/nano/overview.php (2002).

[3] R. Valiev. *Materials science: nanomaterial advantage*. Nature, **419** (2002) 887.

[4] H. Lüth. *Surfaces and interfaces of solid materials*. Springer, Heidelberg (1995).

[5] J. Weissmüller, R. N. Viswanath, D. Kramer, R. Würschum, H. Gleiter. *Charge-induced reversible strain in a metal.* Science, **300** (2003) 312.

[6] H. Gleiter, J. Weissmüller, O.Wollersheim, R. Würschum. *Nanocrystalline materials: a way to solids with tunable electronic structures and properties?* Acta Mater., **49** (2000) 737.

[7] M. Sagmeister, U. Brossmann, S. Landgraf, R. Würschum. *Electrically tunable resistance of a metal*. Phys. Rev. Lett., **96** (2006) 156601.

[8] A. K. Mishra, C. Bansal, H. Hahn. S*urface charge induced variation in the electrical conductivity of nanoporous gold*. J. Appl. Phys., **103** (2008) 094308.

[9] H. Drings, R. N. Viswanath, D. Kramer, C. Lemier, J. Weissmüller, R. Würschum. *Tuneable magnetic susceptibility of nanocrystalline palladium*. Appl. Phys. Lett., **88** (2006) 253103.

[10] S. Dasgupta, R. Kruk, D. Ebke, A. Hütten, C. Bansal, and H. Hahn. *Electric field induced reversible tuning of resistance of thin gold films*. J. Appl. Phys., **104** (2008) 103707.

[11] P. Wahl, T. Traußnig, S. Landgraf, H.-J. Jin, J. Weissmüller, R. Würschum. *Adsorption-Driven Tuning of the Electrical Resistance of Nanoporous Gold*. J. Appl. Phys., **108** (2010) 073706.

[12] S. H. Mushrif, A. D. Rey. *An integrated model for adsorption-induced strain in microporous solids*. Chem. Eng. Sci., **64** (2009) 4744.

[13] J. Prass, D. Müter, P. Fratzl, O. Paris. *Capillarity-driven deformation of ordered nanoporous silica*. Appl. Phys. Lett., **95** (2009) 083121.

[14] H.-J. Jin, S. Parida, D. Kramer, J. Weissmüller. *Sign-inverted surface stress-charge response in nanoporous gold*. Surf. Sci., **602** (2008) 3588.

[15] http://science.jrank.org/pages/1182/Capillary-Action.html.

[16] D. Kramer, R.N. Viswanath, J. Weissmüller. *Surface-stress induced macroscopic bending of nanoporous gold cantilevers*. Nano Lett., **4** (2004) 793.

[17] H.-J. Jin, X.-L. Wang, S. Parida, K. Wang, M. Seo, J. Weissmüller. *Nanoporous Au-Pt alloys as large strain electrochemical actuators*. Nano Lett., **10** (2010) 187.

[18] J. Biener, A. Wittstock, L. A. Zepeda-Ruiz, M. M. Biener, V. Zielasek, D. Kramer, R. N. Viswanath, J. Weissmüller, M. Bäumer, A. V. Hamza. *Surface-chemistry-driven actuation in nanoporous gold*. Nature Mater., **8** (2009) 47.

[19] J. Weissmüler, H.-L. Duan, D. Farkas. *Deformation of Solids with Nanoscale Pores by the Action of Capillary Forces*. Acta Mater., **58** (2010) 1.

[20] G.Reichenauer, G.W. Scherer. *Nitrogen adsorption in compliant materials*. J. Non-Cryst. Solids, **277** (2000) 162.

[21] S. Dourdain, D. T. Britton, H. Reichert, A. Gibaud. *Determination of the elastic modulus of mesoporous silica thin films by x-ray reflectivity via the capillary condensation of water*. Appl. Phys. Lett., **93** (2008) 183108.

[22] G. Günther, M. Schön. *Sorption strains and their consequences for capillary condensation in nanoconfinement*. Mol. Simul., **35** (2009) 138.

[23] L.L. Schramm. *The Language of Colloid & Interface Science: A Dictionary of Terms*. ACS Professional Reference Book. Wiley VCH, Washington, DC (1993)

[24] http://en.wikipedia.org/wiki/Capillary_condensation#cite_note-schramm-0

[25] R.J. Hunter. *Foundations of Colloid Science*, 2nd Edition. Oxford University Press, Oxford (2001)

[26] R. H. Baughman, C. Cui, A. A. Zakhidov, Z. Iqbal, J. N. Barisci, G. M. Spinks, G. G. Wallace, A. Mazzoldi, D. D. Rossi, A. G. Rinzler, O. Jaschinski, S. Roth, M. Kertesz. *Carbon nanotube actuators*. Science, **284** (1999) 1340.

[27] J.C. Farmer, S.M. Bahowick, J.E. Harrar, D.V. FIX, R.E. Martinelli, A.K. Vu, K.L. Carroll. *Electrosorption of chromium ions on carbon aerogel electrodes as a means of remediating ground water*. Energy and Fuels, **11** (1997) 337.

[28] J.C. Farmer, D.V. Fix, G.V. Mack, R.W. Pekala, J.F. Poco. *Capacitive deionization of NH_4ClO_4 solutions with carbon aerogel electrodes*. J. Appl. Electrochem., **26** (1996) 1007.

[29] J.C. Farmer, D.V. Fix, G.V. Mack, R.W. Pekala, J.F. Poco. *Capacitive deionization of NaCl and $NaNO_3$ solutions with carbon aerogel electrodes*. J. Electrochem. Soc., **143** (1996) 159.

[30] S.T. Mayer, R.W. Pekala, J.L. Kaschmitter. *The aerocapacitor: an electrochemical double-layer energy-storage device*. J. Electrochem. Soc., **140** (1993) 446.

[31] R. W. Pekala, J. C. Farmer, C. T. Alviso, T. D. Tran, S. T. Mayer, J. M. Miller, B. Dunn. *Carbon aerogels for electrochemical applications*. J. Non-Cryst. Solids, **225** (1998) 74.

[32] J. Chmiola, G. Yushin, Y. Gogotsi, C. Portet, P. Simon, P.L. Taberna. *Anomalous increase in carbon capacitance at pore sizes less than 1 nanometer*. Science, **313** (2006) 1760.

[33] Y. Oren, H Tobias, A Soffer. *The electrical doublelayer of carbon and graphite electrodes: Part I. Dependence on electrolyte type and concentration*. J. Electroanal. Chem., **162** (1984) 87.

[34] G. Lippmann. *Relations entre les phénomènes électriques et capíllaires*. Ann. de chim. et de phys., **5** (1875) 494.

[35] D. Golub, Y. Oren, A. Soffer. *Electro adsorption, the electrical double layer and their relation to dimensional changes of carbon electrodes*. Carbon, **25** (1987) 109.

[36] D. Golub, A. Soffer, Y. Oren. *The electrical double layer of carbon and graphite electrodes. Part V: Specific adsorption of simple Ions*. J. Electroanal. Chem., **260** (1989) 383.

[37] G. Valincius. *Elastic electrocapillary properties of polycrystalline gold*. Langmuir, **14** (1998) 6307.

[38] D. Kramer, J. Weissmüller. *A note on surface stress and surface tension and their interrelation via Shuttleworth's equation and the Lippmann equation*. Surf. Sci., **601** (2007) 3042.

[39] S. Linden, C. Enkrich, M. Wegener, J. Zhou, T. Koschny, and C.M. Soukoulis. *Magnetic response of metamaterials at 100 terahertz*. Science. **306** (2004) 1351.

[40] V. M. Shalaev. *Optical negative-index metamaterials*. Nature Photon., **1** (**2007**) 41.

[41] C. M. Soukoulis, S. Linden, M. Wegener. *Negative refractive index at optical wavelengths*. Science, **315** (2007) 47.

[42] V. G. Veselago. *The electrodynamics of substrates with simultaneously negative values of ε and μ*. Sov. Phys. Usp., **10** (1968) 509.

[43] J. B. Pendry. *Negative refraction makes a perfect lens*. Phys. Rev. Lett., **85** (2000) 3966.

[44] J. B. Pendry, D. Schurig, D. R. Smith. *Controlling electromagnetic fields*. Science, **312** (2006) 1780.

[45] I. Sersic, M. Frimmer, E. Verhagen, A. F. Koenderink. *Electric and magnetic dipole coupling in near-infrared split-ring metamaterial arrays*. Phys. Rev. Lett., **103** (2009) 213902.

[46] C. Enkrich, M. Wegener, S. Linden, S. Burger, L. Zschiedrich, F. Schmidt, J. F. Zhou, Th. Koschny, C. M. Soukoulis. *Magnetic metamaterials at telecommunication and visible frequencies*. Phys. Rev. Lett., **95** (2005) 203901.

[47] D. H. Werner, D. -H. Kwon, I. -C. Khoo. *Liquid crystal clad near-infrared metamaterials with tunable negative-zero-positive refractive indices*. Opt. Express, **15** (2007) 3342.

[48] X. Wang, D. -H. Kwon, D. H. Werner, I. -C. Khoo, A. V. Kildishev, V. M. Shalaev. *Tunable optical negative-index metamaterials employing anisotropic liquid crystals*. Appl. Phys. Lett., **91** (2007) 143122.

[49] F. Zhang, L. Kang, Q. Zhao, J. Zhou, X. Zhao, D. Lippens. *Magnetically tunable left handed metamaterials by liquid crystal orientation*. Opt. Express, **17** (2009) 4360.

[50] M. J. Dicken, K. Aydin, I. M. Pryce, L. A. Sweatlock, E. M. Boyd, S. Walavalkar, J. Ma, H. A. Atwater. *Frequency tunable near-infrared metamaterials based on VO_2 phase transition*. Opt. Express, **17** (2009) 18330.

[51] H. -T. Driscoll, B. -G. Kim, B. -J. Chae, Y. -W. Kim, N. M. Lee, S. Jokerst, D. R. Palit, D. R. Smith, M. Di Ventra, D. N. Basov. *Memory Metamaterials*. Science, **325** (2009) 1518.

[52] Z. L. Samson, K. F. Mac Donald, F. D. Angelis, B. Gholipour, K. Knight, C. C. Huang, E. D. Fabrizio, D. W. Hewak, N. I. Zheludev. *Metamaterial electro-optic switch of nanoscale thickness*. Appl. Phys. Lett., **96** (2009) 143105.

[53] R. Kötz, D. M. Kolb. *Electroreflectance of copper, silver, and gold single crystal electrodes*. Z. Physik. Chemie NF, **112** (1978) 69.

[54] J. C. Abanulo, R. D. Harris, P. N. Bartlett, J. S. Wilkinson. *Waveguide surface plasmon resonance sensor for electrochemically controlled surface reactions*. Appl. Opt., **40** (2001) 6242.

[55] T. Baum, D. Bethell, M. Brust, D. J. Schiffrin. *Electrochemical charge injection into immobilized nanosized gold particle ensembles: potential modulated transmission and reflectance spectroscopy*. Langmuir, **15** (1999) 866.

[56] A. H. Ali, C. A. Foss, Jr.. *Electrochemically induced shifts in the plasmon resonance bands of nanoscopic gold particles adsorbed on transparent electrodes*. J. Electrochem. Soc., **146** (1999) 628.

[57] M. Takashi, H. Ray, Y. Hajime, O.-o. Haruhi, N. Hitoshi, A. Isao, U. Shuichi. *Electrical control of plasmon resonance of gold nanoparticles using electrochemical oxidation*. J. Phys. Chem. C, **113** (2009**)** 8484

[58] C. Novo, A. M. Funstone, A. K. Gooding, P. Mulvaney. *Electrochemical charging of single gold nanorods*. J. Am. Chem. Soc., **131** (2009) 14664.

[59] A. J. Bard, L. R. Faulkner. *Electrochemical methods: Fundamentals and Applications*. Wiley, New York (2001).

[60] P. A. Christensen, A. Hamnett. *Techniques and Mechanisms in Electrochemistry*. Chapman & Hall, Glasgow (1994).

[61] B. E. Conway. *Electrochemical oxide film formation at noble metals as a surface-chemical process*. Prog. Surf. Sci., **49** (1995) 331.

[62] A.N. Frumkin, O.A. Petrii, B.B. Damaskin, in: J.O.'M. Bockris, B.E. Conway, E. Yeager (Eds.). *Comprehensive Treatise of Electrochemistry*. *Vol. 1: The Double Layer*. Plenum Press, New York (1980).

[63] S. Trasatti, in: H. Gerischer, C. W. Tobias (Eds.). *Advances in Electrochemistry and Electrochemical Engineering, Vol. 10*. Wiley, New York (1977).

[64] J. O'M Bockris, A. K. N. Reddy. *Modern Electrochemistry*. Plenum Press, New York (1970).

[65] D. Kramer. *Dependence of surface stress, surface energy and surface tension on potential and charge*. Phys. Chem. Chem. Phys., **10** (2008) 168.

[66] V.A. Marichev. *Partial charge transfer during anion adsorption: Methodological aspects*. Surf. Sci. Rep., **56** (2005) 277.

[67] V.A. Marichev. *Structure-mechanical approach to surface tension of solids*. Surf. Sci., **600** (2006) 4527.

[68] J.W. Gibbs. *The Scientific Papers of J. Willard Gibbs, vol. I: Thermodynamics*. Dover Publications Inc., New York (1961).

[69] H. Ibach. *The role of surface stress in reconstruction, epitaxial growth and stabilization of mesoscopic structures*. Surf. Sci. Rep., **29** (1997) 195.

[70] W. Haiss. *Surface stress of clean and adsorbate-covered solids*. Rep. Prog. Phys., **64** (2001) 591.

[71] H. Ibach, C. E. Bach, M. Giesen, A. Grossmann. *Potential-induced stress in the solid-liquid interface: Au(111) and Au(100) in an $HClO_4$ electrolyte*. Surf. Sci., **375** (1997) 107.

[72] J. Weissmüller, J. W. Cahn. *Mean stresses in microstructures due to interface stresses: a generalization of a capillary equation for solids*. Acta Mater., **45** (1997) 1899.

[73] S. A. Ramakrishna. *Physics of negative refractive index materials*. Rep. Prog. Phys., **68** (2005) 449.

[74] S. A. Maier. *Plasmonics: Fundamentals and Applications*. Springer, New York (2007).

[75] J. B. Pendry. *Negative refraction*. Contemp. Phys., **45** (2004) 191.

[76] J. T. Shen, P. M. Platzmann. *Near field imaging with negative dielectric constant lenses*. Appl. Phys. Lett., **80** (2002) 3286.

[77] D. R. Smith, W. J. Padilla, D. C. Vier, S. C. Nemat-Nasser, S. Schultz. *Composite medium with simultaneously negative permeability and permittivity*. Phys. Rev. Lett., **84** (2000) 4184.

[78] J. B. Pendry, A. J. Holden, D. J. Robbins, W. J. Stewart. *Magnetism from conductors and enhanced nonlinear phenomena*. IEEE Trans. Microwave Theory Tech. **47** (1999) 2075.

[79] R. A. Shelby, D. R. Smith, S. Schultz. *Experimental verification of a negative index of refraction*. Science, **292** (2001) 77.

[80] N. Katsarakis, T. Koschny, M. Kafesaki, E. N. Economou, C. M. Soukoulis. *Electric coupling to the magnetic resonance of split ring resonators*. Appl. Phys. Lett., **84** (2004) 2943.

[81] http://en.wikipedia.org/wiki/Transmittance

[82] http://scienceworld.wolfram.com/physics/Transmittance.html

[83] http://www.andor.com/pdfs/absorption-transmission-reflectance%20spectroscopy.pdf

[84] S. Parida. *Nanoporous noble metals by alloy corrosion: formation process, microstructure and surface-stress-charge behaviors*. PhD Dissertation. Physik und Mechatronik - der Universität des Saarlandes. (2007).

[85] S. Parida, D. Kramer, C. A. Volkert, H. Rösner, J. Erlebacher, J. Weissmüller. *Volume change during the formation of nanoporous gold by dealloying*. Phys. Rev. Lett., **97** (2006) 035504.

[86] T. F. Baumann, M. A. Worsley, T. Y. Han, J. H. Satcher, Jr.. *High surface area carbon aerogel monoliths with hierarchical porosity*. J. Non-Cryst. Solids, **354** (2008) 3513.

[87] M. Decker. *New light on optical activity: interaction of electromagnetic waves with chiral photonic metamaterials*. PhD Dissertation, Fakultät für Physik des Karlsruher Instituts für Technologie. (2010).

[88] J. Biener, A.M. Hodge, A.V. Hamza. *Microscopic failure behavior of nanoporous gold*. Appl. Phys. Lett., **87** (2005) 121908.

[89] K. L. Yang, S. Yiacoumi, C. Tsouris. *Electrosorption capacitance of nanostructured carbon aerogel obtained by cyclic voltammetry*. J. Electroanal. Chem., **540** (2003) 159.

[90] R.N. Viswanath, D. Kramer, J. Weissmüller. *Variation of the surface stress−charge coefficient of platinum with electrolyte concentration.* Langmuir, **21** (2005) 4604.

[91] A. Ledermann. *Design, fabrication, and characterisation of three-dimensional photonic quasicrystals*. PhD Dissertation, Fakultät für Physik des Karlsruher Instituts für Technologie. (2010).

[92] J. Weissmüller, R. C. Newman, H. -J. Jin, A. M. Hodge, J. W. Kysar. *Nanoporous metals by alloy corrosion: formation and mechanical properties*. MRS Bull., **34** (2009) 553.

[93] J. B. Nelson, D. P. Riley. *An experimental investigation of extrapolation methods in the derivation of accurate unit-cell dimensions of crystals*. Proc. Phys. Soc. (Lon), **57** (1945) 160.

[94] S. Cattarin, D. Kramer, A. Lui, M. Musiani. *Preparation and characterization of gold nanostructures of controlled dimension by electrochemical techniques*. J. Phys. Chem. C, **111** (2007) 12643.

[95] L.-H. Shao, H.-J. Jin, R. N. Viswanath, J. Weissmüller. *Different measures for the capillarity-driven deformation of a nanoporous metal*. Europhys. Lett., **89** (2010) 66001.

[96] L.-H. Shao, J. Biener, D. Kramer, R. N. Viswanath, T. F. Baumann, A. V. Hamza, J. Weissmüller. *Electrocapillary maximum and potential of zero charge of carbon aerogel*. Phys. Chem. Chem. Phys., **12** (2010) 7580.

[97] E. Frackowiak, F. Beguin. *Carbon materials for the electrochemical storage of energy in capacitors*. Carbon, **39** (2001) 937.

[98] V. Lockett, R. Sedev, J. Ralston, M. Horne, T. Rodopoulos. *Differential capacitance of the electrical double layer in imidazolium-based ionic liquids: influence of potential, cation size, and temperature*. J. Phys. Chem. C, **112** (2008) 7486.

[99] A. Lukomska, J. Sobkowski. *Potential of zero charge of monocrystalline copper electrodes in perchlorate solutions*. J. Electroanal. Chem., **567** (2004) 95.

[100] G. A. Planes, M. C. Miras, C. A. Barbero. *Double layer properties of carbon aerogel electrodes measured by probe beam deflection and AC impedance techniques*. Chem. Commun., (2005) 2146.

[101] R. I. Tucceri, D. Posadas. *The effect of surface charge on the surface conductance of silver in surface inactive electrolytes*. J. Electroanal. Chem., **283** (1990) 159.

[102] J. Wang, L. Angnes, H. Tobias, R. A. Roessner, K. C. Hong, R. S. Glass, F. M. Kong, R. W. Pekala. *Carbon aerogel composite electrodes*. Anal. Chem., **65** (1993) 2300.

[103] Q. Zhang, V. Bharti, X. Zhao. *Giant electrostriction and relaxor ferroelectric behavior in electron-irradiated poly (vinylidene fluoride-trifluoroethylene) copolymer*. Science, **280** (1998) 2101.

[104] O. B. Kulyasova, R. K. Islamgaliev, R. Z. Valiev. *On the specific features of tensile tests of small samples of nanostructured materials*. Phys. Met. Metallogr., **100** (2005) 83.

[105] J. P. Randin, E. Yeager. *Differential capacitance study of stress-annealed pyrolytic graphite electrodes*. J. Electrochem. SOC., **118** (1971) 711.

[106] J. P. Randin, E. Yeager. *Differential capacitance study on the basal plane of stress-annealed pyrolytic graphite*. J. Electroanal. Chem., **36** (1972) 257.

[107] K. Kinoshita. *Carbon: electrochemical and physicochemical properties*. Wiley, New York (1988).

[108] R. W. Pekala, J. C. Farmer, C. T. Alviso, T. D. Tran, S. T. Mayer, J. M. Miller, B. J. Dunn. *Carbon aerogels for electrochemical applications*. J. Non-Cryst. Solids, **225** (1998) 74.

[109] H. Gerischer. *An interpretation of the double layer capacity of graphite electrodes in relation to the density of states at the Fermi level*. J. Phys. Chem., **89** (1985) 4249.

[110] L. Pietronero, S. Strässler. *Bond-length change as a tool to determine charge transfer and electron-phonon coupling in graphite intercalation compounds*. Phys. Rev. Lett., **47** (1981) 593.

[111] W. Schmickler. *Interfacial electrochemistry*. Oxford university press, New York (1996).

[112] J. W. McClure. *Band structure of graphite and de Haas-van Alphen effect*. Phys. Rev. **108** (1957) 612.

[113] I. Kolaric, U. Vohrer, J. Fraysse. Patent WO/2004/030210: *Actuator comprising nanotubes, especially carbon nanotubes, layers of carbon nanotubes, and the production and use of the same*. (2004).

[114] R.N. Viswanath, D. Kramer, J. Weissmüller. Adsorbate effects on the surface stress–charge response of platinum electrodes. Electrochim. Acta, **53** (2008) 2757.

[115] E. Kim, C.F. Chen. *Calculation of bulk modulus for highly anisotropic materials*. Phys. Lett. A, **326** (2004) 442.

[116] A. N. Frumkin, O. A. Petrii. *Potentials of zero total and zero free charge of platinum group metals*. Electrochim. Acta, **20** (1975) 347.

[117] Y. H. Yun, V. Shanov, Y. Tu, M. J. Schulz, Se. Yarmolenko, S. Neralla, J. Sankar, S. Subramaniam. *A multiwall carbon nanotube tower electrochemical actuator*. Nano Lett., **6** (2006**)** 689.

[118] R. Pelrine, R. Kornbluh, Q. Pei, J. Joseph. *High-speed electrically actuated elastomers with strain greater than 100%.* Science, **287** (2000) 836.

[119] J. D. W. Madden, B. Schmid, M. Hechinger, S. R. Lafontaine, P. G. A. Madden, F. S. Hover, R. Kimball, I. W. Hunter. *Application of polypyrrole actuators: feasibility of variable camber foils*. IEEE J. Oceanic Eng., **29** (2004) 706.

[120] L.-H. Shao, M. Ruther, S. Linden, S. Essig, K. Busch, J. Weissmüller, M. Wegener. *Electrochemical training and modulation of gold nanostructure optical resonances*. Adv. Mater., **22** (2010) 5173.

[121] M. Ruther, L.-H. Shao, S. Linden, J. Weissmüller, M. Wegener. *Electrochemical restructuring of plasmonic metamaterials*. Appl. Phys. Lett., **98** (2011) 013112.

[122] K.-P. Chen, V. P. Drachev, J. D. Borneman, A. V. Kildishev, V. M. Shalaev. *Drude relaxation rate in grained gold nanoantennas*. Nano Lett., **10** (2010) 916.

[123] D. J. Trevor, C. E. D. Chidsey, D. N. Loiacono. *In situ scanning-tunneling-microscope observation of roughening, annealing, and dissolution of gold (111) in an electrochemical cell*. Phys. Rev. Lett., **62** (1989) 929.

[124] D. M. Kolb. *Reconstruction phenomena at metal-electrolyte interfaces*. Prog. Surf. Sci., **51** (1996) 109.

[125] C. Enkrich, M. Wegener, S. Linden, S. Burger, L. Zschiedrich, F. Schmidt, J. F. Zhou, Th. Koschny, C. M. Soukoulis. *Magnetic metamaterials at telecommunication and visible frequencies*. Phys. Rev. Lett., **95** (2005) 203901.

[126] D. M. Kolb. *In Advances in Electrochemistry and ElectrochemicalEngineering*. H. Gerisher, C. W. Tobias, Eds.. Wiley, New York. 11 (1978).

[127] R. Adzic. *In Advances in Electrochemistry and ElectrochemicalEngineering*. H. Gerisher, C. W. Tobias, Eds.. Wiley, New York. 13 (1984).

[128] A. Aramata. *In Modern Aspects of Electrochemistry*. J. O'M. Bockris, R. E. White, B. E. Conway, Eds.. Plenum Press, New York. 31 (1997).

[129] M. P. Green, K. J. Hanson, D. A. Scherson, X. Xing, M. Richter, P. N. Ross, R. Carr, I. Lindau. *In situ scanning tunneling microscopy studies of the underpotential deposition of lead on gold (111)*. J. Phys. Chem., **93** (1989) 2181.

[130] M. P. Green, K. J. Hanson, R. Carr, I. Lindau. *STM observations of the underpotential deposition and stripping of pb on au(111) under potential sweep conditions*. J. Electrochem. Soc., **137** (1990) 3493.

[131] E. Herrero, L. J. Buller, H. D. Abruña. *Underpotential deposition at single crystal surfaces of Au, Pt, Ag and other materials*. Chem. Rev., **101** (2001**)** 1897.

[132] M. H. Hölzle, V. Zwing, D. M. Kolb. *The influence of steps on the deposition of Cu onto Au(111)*. Electrochim. Acta, **40** (1995) 1237.

[133] M. A. Schneeweiss, D. M. Kolb. *Oxide formation on Au(111) an in situ STM study*. Solid State Ionics, **94** (1997) 171.

[134] Y. Umeno, C. Elsässer, B. Meyer, P. Gumbsch, J. Weissmüller. *Reversible relaxation at charged metal surfaces: an ab initio study*. Europhys. Lett., **84** (2008) 13002 /1-6.

[135] S. Dasgupta, S. Dehm, R. Kruk, H. Hahn. *Electrochemically-gated field-effect transistor with indium tin oxide nanoparticles as active layer*. Acta Phys. Pol. A, **115** (2009) 473.

[136] K.L. Chopra. *Thin Film Phenomena*. McGraw-Hill, New York. (1969).

[137] R. Tucceri. *A review about the surface resistance technique in electrochemistry*. Surf. Sci. Rep., **56** (2004) 85.

[138] J. S. Chawla, F. Zahid, H. Guo, D. Gall. *Effect of O2 adsorption on electron scattering at Cu(001)surfaces*. Appl. Phys. Lett., **97** (2010) 132106.

[139] J.-P. Ganon, C. Nguyen, J. Clavilier. *Étude de l'adsorption électrochimique de l'oxygène sur des lames minces d'or par la mesure de leur résistance électrique*. Surf. Sci., **79** (1979) 245.

[140] W.N. Hansen. *Electrode resistance and the emersed double layer*. Surf. Sci., **101** (1980) 109.

[141] J. D. Jackson. *Klassische Elektrodynamik*. Chapter 17. Walter de Gruyter, Berlin. (1981).

[142] P. Mulvaney, J. Perez-Juste, M. Giersig, L. M. Liz-Marzan, and C. Pecharroman. *Drastic surface plasmon mode shifts in gold nanorods due to electron charging*. Plasmonics, 1 (2006) 61.

[143] P. Mulvaney. *Surface plasmon spectroscopy of nanosized metal particles*. Langmuir, 12 (1996) 788.

8 Appendix

Mathematica notebook for analysis the lattice parameter change using a full pattern correlation technique with Mathematica version 6.0.

Data input

Import Relaxed and Unrelaxed hole data

Be carefull if importing from Excel! The CSV export from Excel uses the cell formatting for the output precision.

```
pathname =
  "E:\\my work\\Germany\\X-ray\\Sam_090515\\1MHClO4\\data\\";
```

```
rawnamesAll =
  { StringJoin[pathname,
    "17_npg-1MHClO4_-200mV_height 1mm.ASC"],
 StringJoin[pathname, "18_npg-1MHClO4_600mV_height 1mm.ASC"],
 StringJoin[pathname, "19_npg-1MHClO4_1350mV_height 1mm.ASC"]
 };
```

Select two files, first one is refrence, second one is sample.

```
rawnames = {rawnamesAll[[1]], rawnamesAll[[3]]}
```

```
{E:\my work\Germany\X-ray\Sam_090515\1MHClO4\data\17_npg-1MHClO4_-200mV_height 1mm.ASC,
 E:\my work\Germany\X-ray\Sam_090515\1MHClO4\data\19_npg-1MHClO4_1350mV_height 1mm.ASC}
```

```
NFiles = Length[rawnames]
```

```
2
```

Import from file with format "Table", dropping the last element.

```
dataRef1 = Drop[Import[rawnames[[1]], "Table"], -1];
dataSample1 = Drop[Import[rawnames[[2]], "Table"], -1];
```

```
Length[dataRef1]
Length[dataSample1]
NPoints1 = Min[Length[dataRef1], Length[dataSample1]]
```

```
1733
```

```
1733
```

```
1733
```

```
dataRef2 = Take[dataRef1, NPoints1];
dataSample2 = Take[dataSample1, NPoints1];
```

Plot both data stes:

```
ListPlot[{dataRef2, dataSample2},
 PlotRange → All, Frame → True, Joined → True,
 PlotStyle → {{PointSize[0.01], Red}, {PointSize[0.01], Blue}},
 FrameLabel → {Text[Style["2 theta", FontSize → 15]],
   Text[Style["counts", FontSize → 15]]}]
```

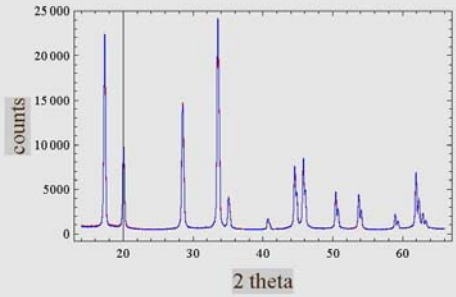

Plot a small region:

```
ListPlot[{dataRef2, dataSample2},
 PlotRange → {{44.2, 45.2}, {1000, 8500}},
 Frame → True, Joined → True,
 PlotStyle → {{PointSize[0.01], Red}, {PointSize[0.01], Blue}},
 FrameLabel → {Text[Style["2 theta", FontSize → 15]],
   Text[Style["counts", FontSize → 15]]}]
```

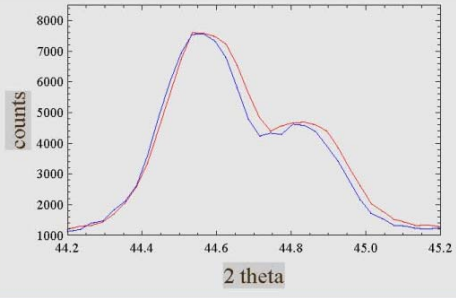

Data smoothing

It turned out that no useful correlationis possible on a sub - (point spacing) scale can be done without smoothing. Otherwise you see artifacts from the discrete nature of the data.

```
NAverage = 5;
dataRef = MovingAverage[dataRef2, NAverage];
dataSample = MovingAverage[dataSample2, NAverage];
```

```
ListPlot[{dataRef, dataRef2},
 PlotRange → {{16, 19}, {3000, All}},
 Frame → True, Joined → True,
 PlotStyle → {{PointSize[0.01], ColorData["Atoms", "N"]},
   {PointSize[0.01], ColorData["Atoms", "Cu"]}},
 FrameLabel → {Text[Style["2 theta", FontSize → 15]],
   Text[Style["counts", FontSize → 15]]}]
```

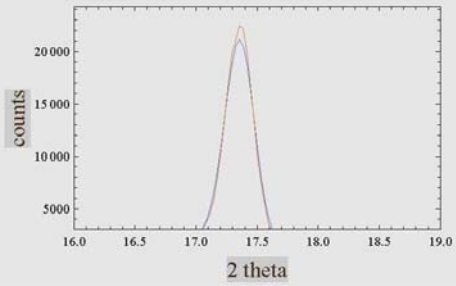


```
NPoints = Min[Length[dataRef], Length[dataSample]]
```

```
1729
```

Conversion of angles to wavenumbers

- **Conversion of angles to wavenumbers**

```
lambda = 0.71097 ;
```

lambda : wavelengthin Angstroem
e : strain
zeroshift : zero point change; this has the same effect as a sample height displacement

We go from angle twothetato wavenumberq through q = 4 Pi Sin[theta]/ lambda.

How do we go from intensityI (in angle-space)to interferencefunction S in q-space?
Our measuredintensityvalue in q space satisfies
Iq Deltaq = Itt Deltatt or
Iq = Itt dtt/dq which the same as Iq = Itt / Cos[theta] exceptfor a constant (since dq/dtt = 2 Pi Cos[theta]/ lambda)

referencedata:

```
S0Ref = dataRef /. {tt_, counts_} →
    {4 π Sin[tt Degree / 2] / lambda, counts / Cos[tt Degree / 2]};
```

this is the actual sample data, as measured:

```
S0Sample = dataSample /. {tt_, counts_} →
    {4 π Sin[tt Degree / 2] / lambda, counts / Cos[tt Degree / 2]};
```

```
ListPlot[{S0Ref, S0Sample},
 PlotRange → All, Frame → True, Joined → True,
 PlotStyle → {{PointSize[0.01], ColorData["Atoms", "N"]},
   {PointSize[0.01], ColorData["Atoms", "Cu"]}},
 FrameLabel → {Text[Style["q  [1/Å]", FontSize → 15]],
   Text[Style["counts", FontSize → 15]]}]
```

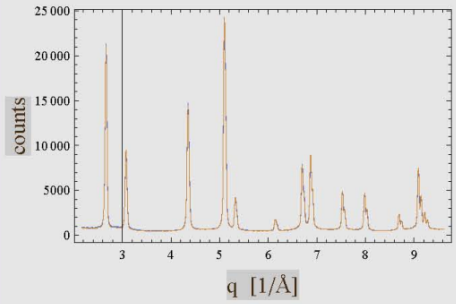

Interpolate Reference Data Set

```
IntOrd = 12;
```

```
LIRef = ListInterpolation[
   S0Ref /. {a_, b_} → {{a}, b}, InterpolationOrder → IntOrd];
```

Show data and interpolationtogether:

```
qRange = {2.2, 3};

Show[
 Plot[LIRef[x], {x, qRange[[1]], qRange[[2]]}, PlotStyle → Red],

 ListPlot[S0Ref, PlotRange → {qRange, All},
  Frame → True, Joined → True, PlotStyle → Blue,
  FrameLabel → {Text[Style["q", FontSize → 15]],
    Text[Style["counts", FontSize → 15]]}]]
```

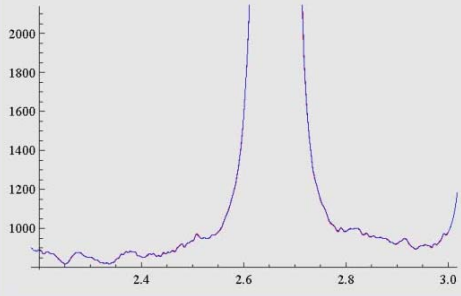

Analyze strain

Preliminary operation

start out by defining reduced arrays, to avoid the need for extrapolation
this means: we cut off data at the ends of the data set, where interpolation is unstable and extrapolation (which is not permissible) might otherwise be required

```
MinP = 50;
MaxP = 50;

S0RefRed = Drop[Drop[S0Ref, -MaxP], MinP];
S0SampleRed = Drop[Drop[S0Sample, -MaxP], MinP];
NRed = Length[S0SampleRed]
```

```
1629
```

Rescaling due to strain

Wavenumber scaling due to lattice strain:

If the lattice parameter scales as a -> a (1 + e) then q scales as q -> q (1 - e) , in other words, when the strain is positive then the peaks move to lesser q

Intensity scaling due to lattice strain:

At the same time, the integrated intensity within any given reflection (Bragg spherical shell in reciprocal space) is conserved.
Since the area of that shell becomes smaller by the factor (1 - 2 e), the local intensity goes up by (1 + 2 e).

Furthermore, the integrated intensity which goes into the constant detector aperture is changed, since that aperture now sees a larger fraction of the scattering pattern. Thus, the apparent intensity goes up by another factor (1 + e).

Overall, the scaling is S -> S (1 + 3 e)

A note of caution: using the above S-scaling means that the result for the strain gets coupled to intensity variations that may be artifacts.
We may want to ignore the scaling (switch off by by setting $\omega = 0$ below) in order to avoid this danger.

Below is one of the most important mathematical operations: we compute a data set for the reference, assuming its strain is e. This can be compared to the actual sample data set. Best agreement is expected if we scale the reference according to the same e that represents the actual strain of the sample.

At the q values qq (which we chose to be the same as in the sample (!) data set) we find the intensity S(qq (1+e)) × (1 + 3 e) where S refers to the reference data set.

```
ω = 1;
(* set ω=0 in order to switch off the intensity scaling.*)
SRefRed[e_] :=
 S0SampleRed /. {qq_, SS_} → {qq , LIRef[qq (1 + e)] (1 + 3 e ω)};
```

The graph shows a simple test.
We assume a positive strain and we find that the peaks of the strained reference (Blue) move to lesser angle and that their intensity increases relative to the unstrained reference (Red).

```
ListPlot[{S0RefRed, SRefRed[0.01]},
 PlotRange → {{2, 8}, {0, All}}, Frame → True,
 Joined → True, PlotStyle → {Red, Blue},
 FrameLabel → {Text[Style["q  [1/Å]", FontSize → 15]],
   Text[Style["counts", FontSize → 15]]}]
```

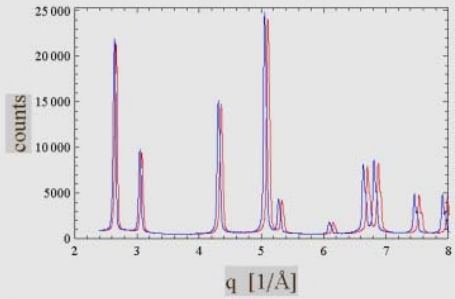

Below, Chisrq is the deviationbetween sample data and the transformedreference data.

Chisrq is the ' badness' of the fit. The smaller Chisqr, the better the fit.

Start out by computing the optimum Chisrq that can be expected. The expectederror for a datapoitn with N counts is Sqrt[n].

Thus, for a perfect model the data set will deviateby an expectationof about N value for mean square deviation.

We normalizeour ChiSqr valueto that number. Thus, if the value Chisqr is around 1 then the fit is good.

```
ChiSqrNorm = Mean[S0SampleRed[[All, 2]]]
```

```
1528.04
```

```
ChiSqr[e_] :=
  Norm[S0SampleRed[[All, 2]] - Round[ SRefRed[e][[All, 2]]]]^2 /
    NRed / ChiSqrNorm;
```

Make a table and plot the result.

```
ChiSqrTable =
  Table[{ee, ChiSqr[ee]}, {ee, -0.0005, 0.0005, 0.00001}] ;
ListPlot[ChiSqrTable, Frame → True,
 Joined → False, PlotStyle → Blue,
 FrameLabel → {Text[Style["strain", FontSize → 15]],
   Text[Style["χ²", FontSize → 15]]}]
```

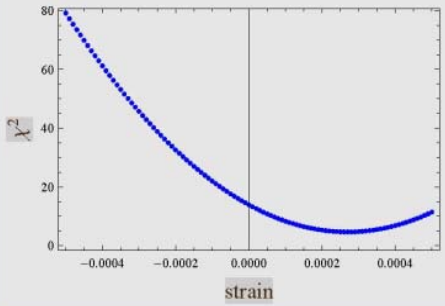

Find the strain as that value off ee where Chisqr is minimum (best fit):

```
strain = ChiSqrTable[[Ordering[ChiSqrTable[[All, 2]]][[1]], 1]]
```

```
0.00027
```

```
badness = ChiSqrTable[[Ordering[ChiSqrTable[[All, 2]]][[1]], 2]]
```

```
4.70125
```

Result

```
strain
```

```
0.00027
```